QUARTERLY PROGRESS REPORT NO. 17

ON

CONTRACT NASr-7

For the Period

October 1, 1964, through December 31, 1964

Project

HYPERVELOCITY IMPACT OF MICROPARTICLES

F. C. Todd, Principal Investigator

B. A. Sodek, Jr., Graduate Research Assistant

Presented by

Research Foundation
Oklahoma State University
Stillwater, Oklahoma

Marvin T. Edmison, Ph.D., Director

FACILITY FORM 602

N66 87290
(ACCESSION NUMBER)

144
(PAGES)

CR 78456
(NASA CR OR TMX OR AD NUMBER)

(THRU)

None
(CODE)

(CATEGORY)

TABLE OF CONTENTS

INTRODUCTION 1

MOST SIGNIFICANT ERRORS. 3

Smoothing of the Data from the Mesh Values 3

Long Slope in the Shock Front. 4

Error in Apparent Ratio of Depth to Surface Radius for the Calculated Crater Shape. 5

Oscillations between the Shock Front and the Free Surface. . 6

SUMMARY OF INFORMATION DISCLOSED BY SOLUTIONS. 9

BIBLIOGRAPHY 11

A HYDRODYNAMIC MODEL OF MICROMETEROID IMPACT

INTRODUCTION

This is the Seventeenth Quarterly Progress Report on Project NASr-7. The title of the project is "Shock, Flow and Radiation from the Hypervelocity Impact of Microparticles." The analytical and experimental phases of this project are concerned with the phenomena that occur with the hypervelocity impact of microparticles on a massive target, which may be solid, or layered. The overall objective is to obtain a sufficiently fundamental understanding of the physical mechanisms in the hypervelocity impact of a microparticle so the momentum and the energy transferred from the particle to the target may be ascertained and, possibly, the density of the incident microparticle may be estimated.

This Progress Report presents the thesis of a candidate for a doctoral degree in physics, Benard A. Sodek, Jr. The title of the thesis is a "Hydrodynamic Model of Micrometeroid Impact." This title is at least two years old, since a tentative title must be named early in the work on a thesis and it is preferred that the title remain roughly the same. A much longer, but more descriptive and more complete title would be "Hydrodynamic Flow from the Hypervelocity Impact of an Aluminum Sphere on a Semi-Infinite Aluminum Slab." This thesis considers the flow that occurs when an aluminum sphere is incident, at hypervelocity, on a semi-infinite aluminum slab. The selection of a sphere of aluminum to impact on a slab of the same material was dictated by the requirement that the program for computation on a digital computer, written in Fortran II, should not overflow the 32,000 word memory of an I.B.M. 7094 digital computer. Part of the required space represents a mesh for which are recorded

the initial position and condition of the material in the problem and for which the values of the solution are recorded as the calculation proceeds.

A more general problem would consider the impact of a sphere of any material on aluminum, or vice versa. The assumptions and the basic techniques for solving this problem require that the equations and techniques of this report be combined with the treatment of the shock penetration and reflection at an interface. The latter subject was treated in Quarterly Progress Report No. 13. Another necessary technique for this problem is the reflection of the shock front from the back, or top face of the impacting sphere. This subject was not considered in Progress Report No. 13 but has recently been studied by Lin Wang, one of our students. Progress Report No. 13 dealt with the penetration of a hemispherical shock in aluminum, through a plane interface into glass. That Progress Report shows the manner in which the interface between two materials, with different Hugoniot curves, must be treated. The preface to Progress Report No. 13 gives many of the considerations that are necessary to evaluate the raw data from the computer into the proper, practical solution of the problem. Much of that information is applicable to this thesis.

The attached thesis presents the direct output of the digital computer. The solution of the presented equations is exact to the degree that a digital computer solution of difference equations, instead of differential equations, may be exact. This thesis purposely presents the solution, as obtained, with only some slight smoothing of the data. For the reader to evaluate the data, it is desirable to designate the regions in which the most significant errors appear and to show why these errors

were permitted to occur. These errors are, in general, a consequence of limitations on the computer method and on the solution from the computer. For this discussion, the more significant errors are grouped under four headings and each is discussed separately. These headings are: (1) Smoothing of the data from the mesh values; (2) Long slope in the shock front; (3) Error in apparent ratio of depth to surface radius for the calculated crater shape; and (4) Oscillations behind the shock front. These sections are followed by a brief summary of the information that is disclosed by the computer solution.

MOST SIGNIFICANT ERRORS

Smoothing of the Data from the Mesh Values

The digital computer employs "difference" equations instead of the actual differential equations for hydrodynamic flow. With the difference equations, average values for the density, velocity, pressure and energy are calculated for each block in the computer mesh. The smooth curve that represents the free surface, as an example, is a curving line that is drawn through all of the blocks in the mesh that have empty meshes on one side and have aluminum filled meshes on the other side. This is illustrated by the smooth curve for the surface that is drawn in Figure 45 on page 109. The blocks with dots have empty space in the meshes above those with dots and aluminum in the meshes below those with dots. In addition to the surface, the isobars, the curves for constant density and the curves for constant energy are drawn in the same way. There are two additional guides for drawing the isobars: (a) The pressure at the tips of the isobars tend toward intersecting lines, although the two intersecting isobars may end in a single block; (b) The curves only show one quadrant and the quadrant

to the left must be a mirror image of the one that is shown. As a consequence, the isobars, iso-density and iso-energy curves must all be perpendicular to the vertical axis.

The size of the mesh is selected from several considerations. The initial mesh size is relatively small to show the details of the initial stages of the impact. The number of meshes in the initial grid is determined by the available space in the memory of the computer. As the impact proceeds, the number of meshes is gradually filled until a preselected boundary mesh is reached. At this time, the computer is programmed to double the radial length of each mesh, but not to change $\Delta\theta$. The solution then fills roughly half of the available number of meshes and the problem may be continued until the meshes are again filled. After the change of scale for the size of the meshes, the values of the variables in two meshes before condensation are averaged, by the required technique, and placed in a single mesh. In addition to the size of mesh, the angular region that is covered by the meshes may need to be increased in order to follow all of the changes that are produced, including those at the greatest distance from the axis of impact. The meshes that are added when the angle is increased in finite steps are the same size as the existing meshes.

Long Slope in the Shock Front

This subject is discussed in considerable detail in the preface to Progress Report No. 13. The following comments are primarily a recapitulation. The long slope is a consequence of employing the method that was proposed by John von Neumann and R. D. Richtmyer[1] in order to obtain a solution for the propagation of a shock front with a digital computer. This is the well established technique that introduces a pseudo-viscosity term to damp

out the computer-generated oscillations. These oscillations result from the large amount of kinetic energy that is inserted in the problem by a large increase in pressure in a single mesh. This subject is discussed in considerable detail in Progress Report No. 13. The actual, thin shock front occurs, according to von Neumann and Richtmyer, near the position of the steepest gradient in the shock front that is calculated by the computer and that is represented by the isobars at the shock front on the plotted curves in this thesis.

Error in Apparent Ratio of Depth to Surface Radius for the Calculated Crater Shape

It is particularly obvious at high initial velocities of the incident bullet, that the ratio of the depth to the surface radius for the craters is greater than unity. It is to be recalled that this ratio is very close to unity for all experimentally produced craters that have been observed. The very highest velocity in this study, 60.64 kilometers per second, or 198,500 feet per second, is higher than measurements have been made on craters. As a consequence, the appearance of the crater must be seriously considered to ascertain if it is real. It probably is not real and this follows from these considerations. During the impact and penetration of the bullet into the target, the material of the target appears to flow up around the outside edges of the entering bullet. Eventually, the highly-compressed material of the target reaches the surface and, according to the plotted results, appears to pile up around the edges of the crater. This pile-up is at complete variance to the spray that is actually observed to be emitted in the formation of the crater at lower velocity impacts. The apparent pile-up of the target material could result in a greater ratio of depth to surface radius

than unity, for the target material must push against this pile-up to escape. This apparent pile-up of material is indicated by the computer calculations, that omit from consideration, some fundamental laws of physics. This omission was known before the solution was started and was necessitated by a lack of space in the memory of the computer to insert them. The nature of the omissions are indicated in the next paragraph.

When the non-dimensional density ratio, $\frac{\rho}{\rho_o}$, becomes less than unity, the material is under tension. When this tension becomes more negative than -15 to -25 kilobars on the equation of state plot, previously unaffected aluminum will rupture. The exact value for rupture is not known and is not directly applicable in this problem. Aluminum that has been heated by the passage of a shock front will rupture at a smaller negative value than indicated above, and the aluminum may even become a vapor and require no energy to rupture. The amount by which the density ratio, $\frac{\rho}{\rho_o}$, must be less than unity is very small and may reach zero for the formation of a spray that will prevent the formation of the pile-up of material. It is not possible to place all of the preceding information in the memory of the computer for a straight-forward solution without the overlapping of the computer program. The actual program employed more than 31,500 words of the available 32,000 words in the memory. The instructions that were given in the computer were to set any value of the density that is less than unity equal to unity and to continue. This is the probable origin of the observed apparent deviation from unity of the ratio of depth to surface radius of the crater.

Oscillations between the Shock Front and the Free Surface

As the penetration of a particle, which has impacted at hypervelocity, proceeds into the target; the particle gradually slows to a stop. Two

possibilities exist to explain the observed separation of an initial and of subsequent shocks and oscillations. (1) The high pressure from the initial impact results in a shock front that propogates faster than the penetrating particle, after the particle is slowed by loss of energy in the target. (2) There is a reflection of the shocks and the oscillations at the back of the penetrating particle. It is to be anticipated; therefore, that oscillations will occur in the region between the shock front and the free surface of the penetrating particle. There is evidence that oscillations are present. Fluctuations in the emitted light are observed and have been reported in these Progress Reports. The computer calculations that are reported in this thesis show their presence.

The computer solution for a hypervelocity impact gives information on the oscillations. Plots of the isobars, for different instants of time during the penetration, may be assembled to illustrate the presence of oscillations. Start by referring to Figure 28 on page 87 of the attached thesis. A non-related error is immediately apparent; the isobar for zero pressure must attach to and coincide with the free surface of the target outside the region of the impact. Except for this error, the pressure down the vertical axis on the drawing shows a slow increase to a maximum and then a more rapid decrease to zero at the shock front. Recall that the apparent long slope of this shock front is not a physical reality, and this was discussed in an earlier section of this preface. There is no particular evidence of an oscillation in this drawing. As the penetration proceeds, Figure 30 on page 90 shows that a low pressure zone, less than 16 megabars, occurs between the isobars for 25 and 20 megabars. This oscillation of more than 4 megabars amplitude is not negligible. As the penetration continues,

Figure 34 on page 95 shows an uneven pressure fall without much evidence of large oscillations. As the penetration proceeds and the pressure falls, the pressure contours on Figures 38 and 40 on pages 100 and 102, respectively, show uneven pressure and some evidence of oscillations. There is no evidence of pronounced oscillations of large amplitude at pressures below roughly 5 megabars.

The oscillations are believed to exist at all pressures; but are masked, more or less, below 5 megabars in comparison to the amplitudes at pressures between 15 and 25 megabars. This is another example in which the instructions to the computer are not correct, in terms of basic physical laws, and an error results. The initial shock front compresses the material up the Hugoniot curve. The details of the compression up this curve were discussed in Progress Report No. 13. The Hugoniot curve includes an increase in entropy as a consequence of the shock compression, since the entropy always increases across a shock front. The expansion behind the shock front is along a line of constant entropy and, in the absence of viscosity, the expansion is along an adiabat. After the first compression by the shock front, subsequent oscillations in the pressure may, or may not, remain on the adiabat on which they started.

The computer was instructed to follow the Hugoniot on the first compression but the first expansion was to be along an adiabat. The computer was not instructed to stay on the adiabat for subsequent compressions and expansions. As a consequence, the computer tends to have the second compression return toward the initial Hugoniot curve instead of remaining on the adiabat. This is the equivalent to having the computer drop, from the computation, some of the internal energy of the material. A second shock

front, which produces a second compression, should increase the energy content of the material from the starting position of the material as it follows the adiabat in expanding. A slow increase in the pressure, should be along the adiabat on which the material starts the compression. Without further discussion of the type of recompression which may occur, it is significant that the deviation from the correct results are the greatest below roughly 5 megabars. An inspection of the Hugoniot and the associated adiabats will show that significant deviation are largest in this pressure range. Lin Wang, one of our students, has modified the program, at the "expense" of more space in the computer memory so pressure oscillations will follow the adiabat on which the material finds itself after the original compression by the shock front.

SUMMARY OF INFORMATION DISCLOSED BY SOLUTIONS

The presented curves from the computer solution are an approximation to the actual solution for the hypervelocity impact, at vertical incidence, of a sphere on a semi-infinite slab. The reasons for the approximations were presented in the preceding discussion, and are primarily related to insufficient space in the memory of a 7094 computer. After this discussion of errors in the solution, it is desirable to mention the facts which this solution does establish.

The solution shows that the sphere penetrates, with a relatively smooth motion, into the semi-infinite slab. The impact compresses the material of the sphere and of the target ahead and beyond the sides of the sphere of the original sphere. This compression of the material of the target and sphere produces a cavity which appears behind the sphere but this cavity is only remotely related to the crater which eventually forms.

The curves which present the computer calculations apparently show rough edges and a pile-up of material around the edges of the cavity which is mentioned in the preceding paragraph. These rough edges are mostly erroneous and result from incorrect information to the computer. This subject is discussed in the preceding sections of this preface to the thesis. This pile-up of material should be ignored. In general, this "ignores" material that has been subjected to such a large shock compression, that the decompressed material, after the compression-expansion cycle, is either a plasma, a gas, or a liquid.

As the penetration of the sphere continues, highly compressed zones are formed in the combined material of the target and the sphere. These compressed zones precede and surround the region in which the sphere is penetrating. The isobars for these compressed zones assume the shape of crude, thick bottomed "bowls" with sharp, upward-pointing edges. The "bowls" become larger in diameter and deeper below the surface as the initial velocity of the sphere increases.

The material on the surface of the target remains at substantially atmospheric pressure. At atmospheric pressure, the surface distrubance from the impact can travel no faster than the velocity of sound in the elastic material of the target. More accurately, it travels at the velocity of the Rayleigh, or shear waves. The information to give this velocity is not programmed into the computer on account of the amount of space that it would require in the memory of the computer. A more detailed equation of state is required and this basic information is available to formulate a program. The surface velocity that is programmed is the so-called hydrostatic velocity which is essentially zero on the exact air-metal interface.

The shock front, which produces the highly compressed material below and on the sides of the penetrating sphere, travels at a very high velocity in the body of the target. The sharp edges of the "isobar-lines", which define the "bowl", are formed deep in the target, reach the surface ahead of the true surface disturbance, and blow off the surface material around the edges of the "bowl". These blown-off edges are the edges of the crater that is formed by the overall action of the impact.

Since the impact does not obey the laws of similitude for different velocities, or for different diameters, the impact was investigated for six velocities. Since the effect of the diameter was more difficult to formulate, it was not investigated for this particular thesis. About 222 curves, besides those that are included in this report are required to show the variation of the impact with velocity. These curves will be forwarded in the next Quarterly Progress Report.

BIBLIOGRAPHY

1. J. von Neumann and R. D. Richtmyer; Jour. App. Phys. 21, 232-237, (1950)

A HYDRODYNAMIC MODEL OF MICROMETEOROID IMPACT

By

BENARD A. SODEK, JR.

Bachelor of Science

Loyola University of the South

New Orleans, Louisiana

1959

Submitted to the faculty of the Graduate
School of the Oklahoma State
University in partial
fulfillment of the degree of
DOCTOR OF PHILOSOPHY
May, 1965

A HYDRODYNAMIC MODEL OF

MICROMETEOROID IMPACT

Thesis Approved:

Thesis Adviser

Dean of the Graduate School

Dedicated

to

my wife, Gail

PREFACE

This problem was started at the suggestion of Dr. F. C. Todd who acted as my adviser and project supervisor. I am indebted to him for his guidance, assistance, patience, and encouragement during the progress of this work.

The purpose of this research is to investigate a plausible mechanism of hypervelocity impact. The incidence of a 10^{-9} gram aluminum microparticle on a semi-infinite aluminum target is described in terms of fluid flow in two space dimensions.

Computer time for the actual production of the solution was made available by Mr. W. Merle Alexander of Goddard Space Flight Center. I have special thanks for Mr. William Cahill and his staff of this installation who greatly facilitated scheduling of computer time and who supervised the exchange by mail of computer program and results.

A number of preliminary and auxilliary computer programs associated with this project were run on IBM 650, IBM 1420, and IBM 1620 computers on the Oklahoma State University Campus.

The work was carried out under NASA Contract number NASr-7 administered through the Research Foundation of Oklahoma State University.

TABLE OF CONTENTS

Chapter		Page
I.	INTRODUCTION AND SURVEY OF THE PROBLEM	1
	Proposed Impact Theories.	2
	Statement of the Problem.	4
II.	FUNDAMENTALS OF THE INVISCID FLUID MODEL	8
	The Equations of Fluid Flow	8
	A Brief Description of Shock Waves.	14
	The Introduction of Dissipation	19
	The High Pressure Equation of State	21
	Dimensionless Differential Equations. . . .	24
III.	THE NUMERICAL METHOD	27
	The Two Dimensional Difference Equations. .	30
	Finite Difference Mesh Configuration and Cycling	39
	Quality of Solutions.	43
	Development of Computer Program	46
IV.	DEVELOPMENT AND PRESENTATION OF SOLUTIONS. . . .	50
	Initial Values.	51
	Boundary Conditions	53
	The Solutions	53
	Organization of Solutions	54
	Shock Wave Formation and Decay.	56
	Material Velocity Profiles.	62
	Pressure Profiles	67
	Density Profiles.	75
	Two Dimensional Distributions	80
	Pressure and Material Velocity Distributions	82
	Cavity Formation.	103
	Density Distributions	120
	Dissipation of the Peak Pressure.	128
	Discussion of Results	137
V.	SUMMARY AND SUGGESTIONS FOR FUTURE WORK.	139
BIBLIOGRAPHY.		141

LIST OF TABLES

Table Page

I. Polynomial Forms and Constants for Aluminum. . . 23

LIST OF FIGURES

Figure		Page
1.	Plane Shock Front	15
2.	Typical Pressure Profile of a One Dimensional Shock Wave	17
3.	One Space Dimension Finite Difference Net	29
4.	Two Space Dimension Finite Difference Mesh	32
5.	Cell Boundary Notation	34
6.	Initial Partial Area Calculation	41
7.	Computer Flow Diagram	48
8.	Initial Value Illustration	52
9.	Radial Velocity as a Function of Distance Along Axis, Case III	58
10.	Radial Velocity as a Function of Distance Along Axis, Case III	59
11.	Radial Velocity as a Function of Distance Along Axis, Case III	60
12.	Radial Velocity as a Function of Distance Along Axis, Case VI	63
13.	Radial Velocity as a Function of Distance Along Axis, Case VI	64
14.	Radial Velocity as a Function of Distance Along Axis, Case VI	65
15.	Radial Velocity as a Function of Distance Along Axis, Case VI	66
16.	Pressure Profiles Along Normal Axis, Case III	69
17.	Pressure Profiles Along Normal Axis, Case III	70
18.	Pressure Profiles Along Normal Axis, Case III	71

19. Pressure Profiles Along Normal Axis, Case III. . . 72

20. Pressure Profiles Along Normal Axis, Case III. . . 73

21. Pressure Profiles Along Normal Axis, Case III. . . 74

22. Density Profiles Along Normal Axis, Case I 76

23. Density Profiles Along Normal Axis, Case I 77

24. Density Profiles Along Normal Axis, Case I 78

25. Velocity Distribution, Case V
(Time = 7.19×10^{-11} seconds). 83

26. Pressure Contours, Case V
(Time = 7.19×10^{-11} seconds). 84

27. Velocity Distribution, Case V
(Time = 1.08×10^{-10} seconds). 86

28. Pressure Contours, Case V
(Time = 1.08×10^{-10} seconds). 87

29. Velocity Distribution, Case V
(Time = 1.44×10^{-10} seconds). 89

30. Pressure Contours, Case V
(Time = 1.44×10^{-10} seconds). 90

31. Velocity Distribution, Case V
(Time = 2.17×10^{-10} seconds). 91

32. Pressure Contours, Case V
(Time = 2.17×10^{-10} seconds). 92

33. Velocity Distribution, Case V
(Time = 2.98×10^{-10} seconds). 94

34. Pressure Contours, Case V
(Time = 2.98×10^{-10} seconds). 95

35. Velocity Distribution, Case V
(Time = 4.24×10^{-10} seconds). 96

36. Pressure Contours, Case V
(Time = 4.24×10^{-10} seconds). 97

37. Velocity Distribution, Case V
(Time = 8.96×10^{-10} seconds). 99

38. Pressure Contours, Case V
(Time = 8.96×10^{-10} seconds). 100

39. Velocity Distribution, Case V (Time = 1.52×10^{-9} seconds) 101

40. Pressure Contours, Case V (Time = 1.52×10^{-9} seconds) 102

41. Velocity Distribution, Case V (Time = 2.11×10^{-9} seconds) 104

42. Pressure Contours, Case V (Time = 2.11×10^{-9} seconds) 105

43. Velocity Distribution, Case V (Time = 5.49×10^{-9} seconds) 106

44. Pressure Contours, Case V (Time = 5.49×10^{-9} seconds) 107

45. Pressure Contours, Case IV (Time = $.691 \times 10^{-9}$ seconds) 109

46. Position of Surface at Various Times, Case IV. . . 110

47. Position of Surface at Various Times, Case IV. . . 111

48. Position of Surface at Various Times, Case IV. . . 112

49. Position of Surface at Various Times, Case V . . . 115

50. Position of Surface at Various Times, Case VI. . . 116

51. Position of Surface at Various Times, Case VI. . . 117

52. Position of Surface at Various Times, Case VI. . . 118

53. Position of Surface at Various Times, Case VI. . . 119

54. Position of Surface at Various Times, Case I . . . 121

55. Constant Density Contours, Case V (Time = 1.08×10^{-10} seconds). 122

56. Constant Density Contours, Case V (Time = 2.98×10^{-10} seconds). 123

57. Constant Density Contours, Case V (Time = 8.96×10^{-10} seconds). 124

58. Constant Density Contours, Case V (Time = 1.52×10^{-9} seconds) 125

59. Constant Density Contours, Case V (Time = 5.49×10^{-9} seconds) 126

60. Approximate Peak Pressure vs. Maximum Penetration, Case IV 129

61. Approximate Peak Pressure vs. Maximum Penetration, Case VI 130

62. Approximate Peak Pressure vs. Maximum Penetration, Case V. 131

63. Approximate Peak Pressure vs. Maximum Penetration, Case III. 132

64. Approximate Peak Pressure vs. Maximum Penetration, Case II 133

65. Approximate Peak Pressure vs. Maximum Penetration, Case I. 134

66. Position of Primary Shock Front on Normal Axis at a time when the Micrometeoroid is One-Half Embedded in the Target as a Function of Initial Impact Velocity. 136

CHAPTER I

INTRODUCTION

Micrometeoroids are defined as particles which have a mass of less than 10^{-4} grams and velocities that range from 30,000 to 240,000 feet per second. When these microparticles are smaller than 10^{-11} to 10^{-12} grams, the pressure of the radiation from the Sun will eventually push these particles outside the orbit of the earth. (1). They are detected by devices placed on space vehicles. One device that has been successfully used is a photomultiplier tube with a vapor deposited aluminum film covering the face. (2). The micrometeoroids impinging upon the face of the photomultiplier are known to produce a pulse of current through the tube. Other devices that depend on the production of a plasma by the impact are presently used.

The NASA project for which this thesis is a contribution was initiated as an analytical and limited experimental study of micrometeoroid impact on the coated photomultiplier. The project is concerned with the mechanics of impact which result in producing light to activate the photomultiplier tube and which result in producing the craters associated with hypervelocity impacts.

Proposed Impact Theories

A few published articles have reported methods to predict and analyze the impact phenomena of small particles with hypervelocities. The latter term includes all velocities in excess of the velocity of sound in the target. One article approaches the problem from the thermal damage theory. (3). In this theory, the flash of light accompanying the impact is attributed to incandescence of the target and of the micro-particle in the immediate vicinity of the impact. By this concept, the crater is caused by vaporization and explosion of some of the target. This model has been criticized for the following reasons. The crater is found to be lined with projectile material. The thermal model, however, offers no explanation for this lining effect. Conversely, it would appear that as the target material is converted to a vapor, the projectile material should also be converted to a vapor. The succeeding explosion should, therefore, hurl both surrounding target material and the projectile out of the crater. Another reason for not accepting the entire thermal damage model has been suggested by calculations based on a limited amount of experimental evidence. (4). It was found that over 50 percent of the kinetic energy is required to heat and melt the volume of target material that is removed from the crater. This leaves very little energy for evaporation and radiation processes.

Bjork (5) examined the problem of a high-velocity projectile of cylindrical symmetry impinging upon a semi-infinite

solid. Bjork used a hydrodynamic model of impact which suggests that the penetration of a projectile into the target is much the same as one fluid penetrating another. That is, the target and projectile, under the tremendous forces of impact, become fluid and the fluid projectile penetrates the fluid target. The hemispherical shape of the crater is attributed to the strong radial shock wave that is initiated at the point of impact. One defect of this model is that it does not include a mechanism for the production of light. This thesis shares a number of assumptions and procedures with the work of Bjork.

A different theory of impact has been proposed by F. C. Todd (6), project supervisor. This theory proposes that a plasma is formed by the strong radial shock from the impact. A plasma is defined as a mixture of ions and electrons. It will start to form from the application of pressure alone at a pressure of approximately 100,000 atmospheres. (7). The radiation that accompanies the impact results from the electrons in the plasma recombining to form neutral atoms. It is also proposed that a radial shock wave would account for nearly hemispherical shape of the crater. It can be seen that the proposed plasma model partially agrees with the assumptions made in both the thermal damage and hydrodynamic models of impact. The plasma model includes a radial shock which was assumed to accompany the hydrodynamic model and it also assumes that the material in the immediate vicinity of the impact regions has a high energy density as does the

thermal model. It differs from the thermal damage model in that for thermal damage, the high energy density is in the form of a high temperature; while, for the plasma model, more of the energy is in the form of recoverable potential energy.

Statement of the Problem

The subject of this thesis is the investigation of the hydrodynamic mechanism involved in the plasma theory proposed by F. C. Todd. It is particularly desired to determine whether it is possible to theoretically calculate the formation and propagation of a shock wave resulting from a hypervelocity impact.

When a microparticle, traveling at hypersonic velocities, strikes a target, a crater is formed which is many times larger than the projectile and is centered about the point of initial contact. The crater may have a small lip around its edge. Rapid sequence photographs show that a fine spray of material is ejected from the boundaries of the crater as it forms. This evidence is to be contrasted with the more familiar impact of subsonic projectiles. These leave long, deep holes in the target which are only slightly larger than the projectile itself.

Reasons for assuming inviscid, hydrodynamic flow in a hypervelocity impact have been summarized by Charters (8). His qualitative description of penetration shares a number of features with the quantitative results of this thesis. Much of the qualitative discussion that follows is based on

photographs published by Charters. The observation that the formation of the crater requires many microseconds suggests a sustained disturbance, such as from a shock wave, in contrast to an explosive reaction. The material is ejected by hydrodynamic flow along the walls of the crater. From these comments and the symmetrical shape of the crater, the hydrodynamic model appears to provide the best clarification of the results.

A basic feature of the model to be investigated is the formation of two shock waves at the position of the initial contact. One strong shock wave radiates out from the point of impact compressing and accelerating the material of the target. This shock wave precedes the penetrating microparticle into the target. The other shock wave propagates backward against the motion of the impacting microparticle. This shock wave eventually reaches the back edge of the microparticle and is reflected back into the direction of motion of the first shock.

The computer solution does not distinguish between the aluminum of the incident sphere and the aluminum of the semi-infinite target after they come into contact. The details of the impact are, consequently, a little difficult to follow and to interpret. Anticipating the general results of the solution, the impacting microparticle appears to compress the target material ahead of and surrounding itself. This results in the hydrodynamic flow of the target material up, around the entering particle and out of the target.

According to the pictures from Charters' article, this material leaves the target as spray.

The model to be studied involves the assumption of inviscid fluid behavior of the target and projectile, and it neglects heat conduction, radiation, and other forms of energy dissipation. While this characterization will be modified to a limited degree by the inclusion of a pseudo viscosity at the shock front and at large oscillations in the velocity, the proposed model remains basically that of a non-viscous fluid. It will develop that the proposed program requires over 31,500 words of space in the computer memory, and only 32,000 words are available. The inclusion of any of the many other obvious corrections to the impact problem would require an extremely large increase in the length of time on the computer.

The problem for solution is the impact of a spherical, aluminum particle of mass 10^{-9} grams. Velocities of impact are from about 15,000 to 240,000 feet per second. The target is a semi-infinite block of aluminum.

The work presented in this thesis may be briefly outlined as follows:

(1) The partial differential equations and the auxilliary equations of large-scale fluid flow are developed and converted to a dimensionless form.

(2) The dimensionless hydrodynamic equations are converted to difference equations for computer

solution.

(3) The difference equations are translated into a computer program.

(4) The computer program, combined with initial conditions and boundary conditions, gives solutions describing the initial stages of shock wave propagation and crater development for several different impact velocities when a hydrodynamic model is assumed.

CHAPTER II

FUNDAMENTALS OF THE INVISCID FLUID MODEL

When a microparticle with a velocity of 36 kilometers per second impacts on a target, the pressure is calculated to be millions of atmospheres. (4,5). At such extreme conditions, both projectile and target are considered to be non-viscous fluids. The necessary mathematical formulas to describe inviscid flow exist, are well known, and are proven by experiment. They are the three equations for the conservation of mass, energy and momentum. Boundary conditions and equations of state for the materials of the microparticle and the target are required to describe conditions on each side of the impact. The entropy must also increase across the shock front. These equations do not have a closed solution or a practically useful approximate solution. The mathematics are generalized as far as possible and prepared for solution by numerical methods which utilize a high speed electronic computer.

The Equations of Fluid Flow

The basic equations of the hydrodynamic model are obtained by the application of conservation laws to a perfect fluid. Let S be a closed surface, fixed in space and

enclosing a volume, τ ; then the increase of mass inside this surface is

$$\frac{\partial}{\partial t}\int_\tau \rho \, d\tau = \int_\tau \frac{\partial \rho}{\partial t} \, d\tau$$

In this equation, ρ is the density, dt and $d\tau$ are increments of time and volume. The rate of flux through S is

$$-\int_S \rho \, \vec{V} \cdot d\vec{s}$$

where $\vec{V}$ is the material velocity and $\vec{s}$ is a small element of the bounding surface. The rates must be equal.

$$\int_\tau \frac{\partial \rho}{\partial t} \, d\tau = -\int_S \rho \vec{V} \cdot d\vec{s}$$

which by means of the divergence theorem becomes

$$\int_\tau \left[\frac{\partial \rho}{\partial t} + \vec{\nabla} \cdot (\rho \vec{V}) \right] d\tau = 0$$

Since the volume τ is quite arbitrary, the integrand must vanish for all volumes.

$$\frac{\partial \rho}{\partial t} + \vec{\nabla} \cdot (\rho \vec{V}) = 0 \qquad 2.1$$

This is the expression for conservation of mass.

The conservation of momentum is derived in a similar manner. Consider a volume, τ , of fluid that is bounded by a closed surface S . If p is the hydrostatic pressure, the force acting on the volume, V , is

$$-\int_S p \, d\vec{s}$$

Transforming to a volume integral,

$$-\int_S p \, d\vec{s} = -\int_\tau \vec{\nabla} p \, d\tau$$

The force per unit volume acting on the fluid is

$$f = -\vec{\nabla} p$$

This is the largest force considered in fluid mechanics. Using Newton's Second Law,

$$\rho \vec{F} + \rho \frac{d\vec{V}}{dt} + \vec{\nabla} p = 0$$

where $\vec{F}$ represents the resultant of any body forces acting on the fluid. Body forces such as gravitational, magnetic, or electric, are not important in the hydrodynamic model for this application and $\vec{F}$ is set equal to zero. The equation of motion is now written,

$$\rho \frac{d\vec{V}}{dt} + \vec{\nabla} p = 0 \qquad 2.2$$

The equation expressing conservation of energy can be obtained by analogy with the conservation of mass equation. The relation expressing continuity of total energy is

$$\rho \frac{d\mathcal{E}}{dt} = -\vec{\nabla} \cdot (p \vec{V}) \qquad 2.3$$

where $\mathcal{E}$ is the total energy per unit mass.

An auxilliary equation is necessary to relate the pressure, p, to other fluid variables.

$$p = p(\rho, e) \qquad 2.4$$

This is the equation of state which yields the pressure as a

function of the density and the specific internal energy. There are two forms in which these equations can be tied to a physical region. The Eulerian reference frame deals with the values of dependent variables at fixed points in space and time. The Lagrangean system describes the motion of a fluid in terms of the trajectories of individual elements. In most cases and particularly for two and three dimensional cases, Euler's representation is preferable from a mathematical and a physical point of view, according to Courant and Friedricks (8).

Previous solutions of large scale fluid motion in two, or three, dimensions have usually employed rectangular or cylindrical coordinates. An examination of experimental evidence and of earlier analytic approaches indicates that a radial, or polar, coordinate system is the best representation for this particular problem. The shapes of craters from high velocity impacts are virtually perfect hemispheres. This would indicate that the transfer of energy from projectile to target is largely accomplished by means of radial flow. This description complicates the representation of the impacting sphere, but the desire to portray the formation and propagation of the expected shock front is an overriding consideration. Since experimental evidence of the actions of target and projectile shows no azimuthal effects, symmetry of the solution about an axis normal to the semi-infinite target (that is, the z-axis) will be used in writing the equations in polar form.

Using a few identities, the vector forms of the hydrodynamic flow equations, are easily converted to scalar, polar form. The necessary expansions are

$$\nabla \cdot \vec{F} = \frac{1}{r}\left(\frac{\partial}{\partial r}(r F_r) + \frac{\partial F_\theta}{\partial \theta}\right)$$

$$\nabla \varphi = \left[\, \partial\varphi/\partial r \,,\ 1/r(\partial\varphi/\partial\theta) \,\right]$$

and $\nabla \cdot \varphi \vec{F} = \varphi \nabla \cdot \vec{F} + \nabla \varphi \cdot \vec{F}$.

where $\vec{F}$ is a vector quantity and φ is a scalar.

The conservation of mass becomes

$$\frac{\partial \rho}{\partial t} = -\frac{\partial(r \rho u)}{r \partial r} - \frac{\partial(\rho w)}{r \partial \theta} \qquad 2.5$$

The new variables u and w are the radial and tangential components of the material velocity vector, $\vec{V}$.

The polar equations expressing conservation of momentum are not so easily obtained. The original equation is equivalent to two scalar equations, one for each component of the velocity,

$$\rho \frac{du}{dt} = -\frac{\partial p}{\partial r}$$

$$\rho \frac{dw}{dt} = -\frac{\partial p}{r \partial \theta}$$

Remembering that for a scalar φ ,

$$\frac{d\varphi}{dt} = \frac{\partial \varphi}{\partial t} + \vec{V} \cdot \nabla \varphi$$

the first equation is rewritten,

$$\frac{u}{r}\frac{\partial(ru)}{\partial r} + \frac{w}{r}\frac{\partial u}{\partial \theta} + \frac{\partial p}{\partial r} = -\frac{\partial u}{\partial t}$$

This equation will now be put into a form appropriate for "conservative" differencing by adding a term, $u\frac{\partial \rho}{\partial t}$, to each side and using equation 2.5. The result is

$$\frac{\partial(\rho u)}{\partial t} = -\frac{\partial p}{\partial r} - \frac{\partial(r\rho u u)}{r\,\partial r} - \frac{\partial(\rho w u)}{r\,\partial \theta} \qquad 2.6$$

The equation for the other velocity component is obtained in a similar way,

$$\frac{\partial(\rho w)}{\partial t} = -\frac{\partial p}{r\,\partial \theta} - \frac{\partial(r\rho u w)}{r\,\partial r} - \frac{\partial(\rho w w)}{r\,\partial \theta} \qquad 2.7$$

The formula describing conservation of energy is also manipulated into a conservative form.

$$\frac{\partial(\rho e)}{\partial t} = -\frac{\partial(r p u)}{r\,\partial r} - \frac{\partial(p w)}{r\,\partial \theta} - \frac{\partial(r\rho u e)}{r\,\partial r} - \frac{\partial(\rho w e)}{r\,\partial \theta} \qquad 2.8$$

Since the conservation of momentum requires two equations, the three conservation conditions require four equations, 2.5 to 2.8. Two more relations are required to solve for the propagation of a shock wave. These are an equation of state and the condition that the entropy increase across the shock front. These last two requirements may be incorporated into an equation of state based on the Hugoniot curve. This modified equation of state is represented in functional notation by equation 2.4 and this relation will be discussed in more detail in a following section. Although the equation of state involves only three variables, auxiliary relations are needed

to interrelate five unknowns the density, ρ ; the velocities, u and w ; the internal energy, e ; and the pressure, p .

A Brief Description of Shock Waves

Shock waves are only dilatational waves in a non-viscous fluid medium, which has negligible resistance to shear. For this reason, the flow of highly compressed solids may be represented by the equations of hydrodynamic flow. In the propagation of a shock front, the pressure rises to a high value in a very thin zone. This infinitesimal region of rapidly changing pressure, density, and internal energy appears as a discontinuity in the equations for hydrodynamic flow.

To obtain solutions, it is necessary to derive conditions that relate the state of the material on one side of the shock front to that on the other side. The conditions are usually called the Rankine - Hugoniot conditions.

Consider a plane shock front, as illustrated in Figure 1, traveling with a velocity of propagation Σ into stationary material at pressure p_0 , density ρ_0 , and specific internal energy e_0 . The encompassed material is accelerated to a particle velocity σ by the passage of the shock front and is compressed to a density $\rho > \rho_0$. The state of the shocked portion of the medium is related to the undisturbed state by a series of conservation equations:

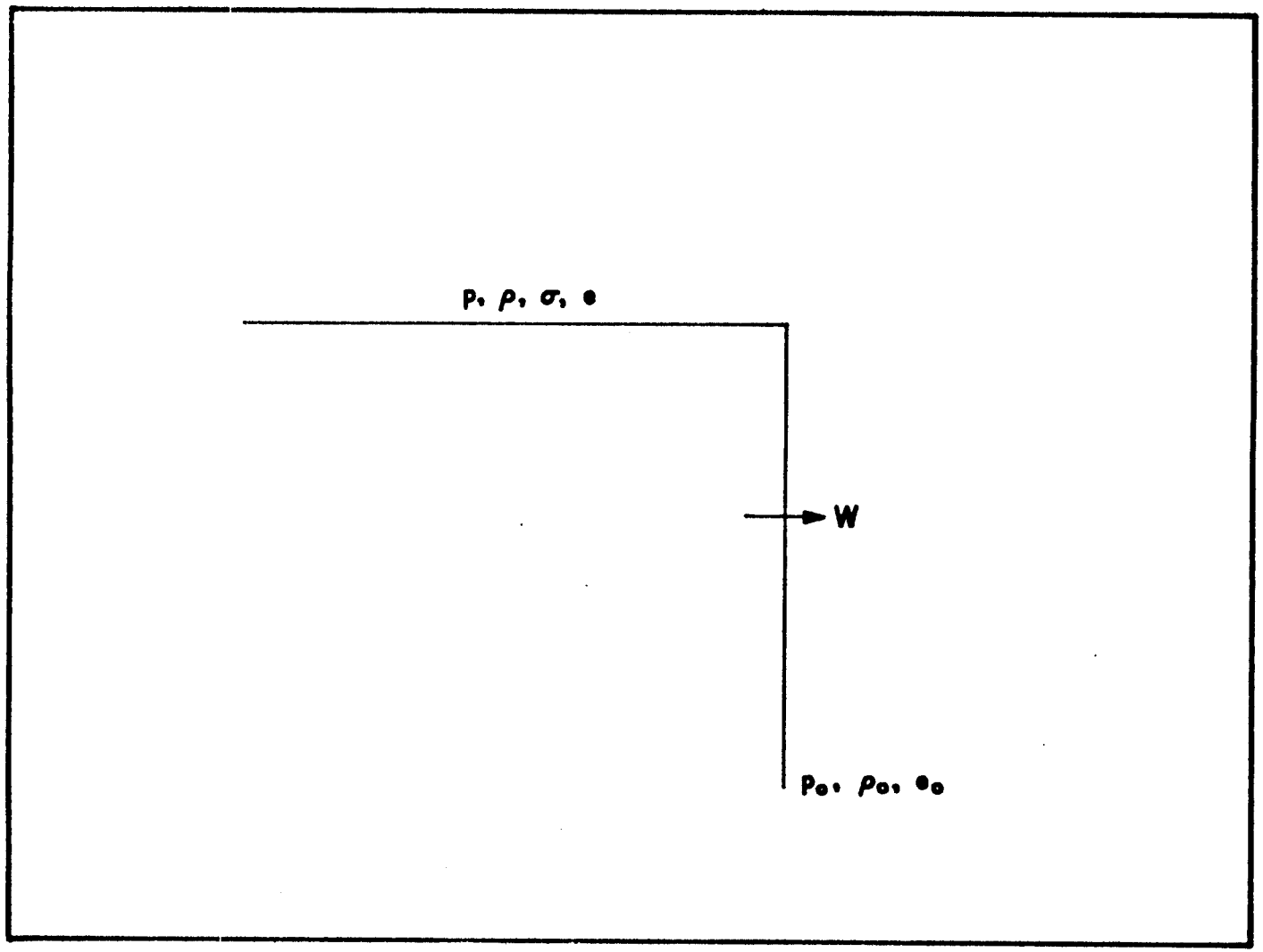

Figure 1. Plane Shock Front

Conservation of mass

$$\rho_0 \Sigma = \rho(\Sigma - \sigma)$$

Conservation of momentum

$$p - p_0 = \rho_0 \Sigma \sigma$$

Conservation of energy

$$p\sigma = \rho_0 \Sigma (e - e_0 + \sigma^2/2)$$

These can be combined to give the Rankine - Hugoniot energy equation

$$e - e_0 = \frac{1}{2}(V_0 - V)(p + p_0)$$

where $V = 1/\rho$.

These equations involve five parameters of the shocked state. One more relation, an equation of state, is required before the specification of one variable is sufficient to permit the calculation of the other four. When the equation of state is given in the form e = e (p,V), it may be combined with the Rankine - Hugoniot energy equation to yield a relation between the pressure and the specific volume. Such an expression is known as the "Hugoniot Curve" or simply as the "Hugoniot." This Hugoniot is unique for a given material, as are an isotherm or an adiabat. This special pressure volume curve represents the totality of the p,V points which may be reached by a shock transition from an initial state p_0, V_0.

A typical pressure profile for a one dimensional shock wave is indicated in Figure 2. Ahead of the shock front the material is undisturbed. At the head of the wave the pressure,

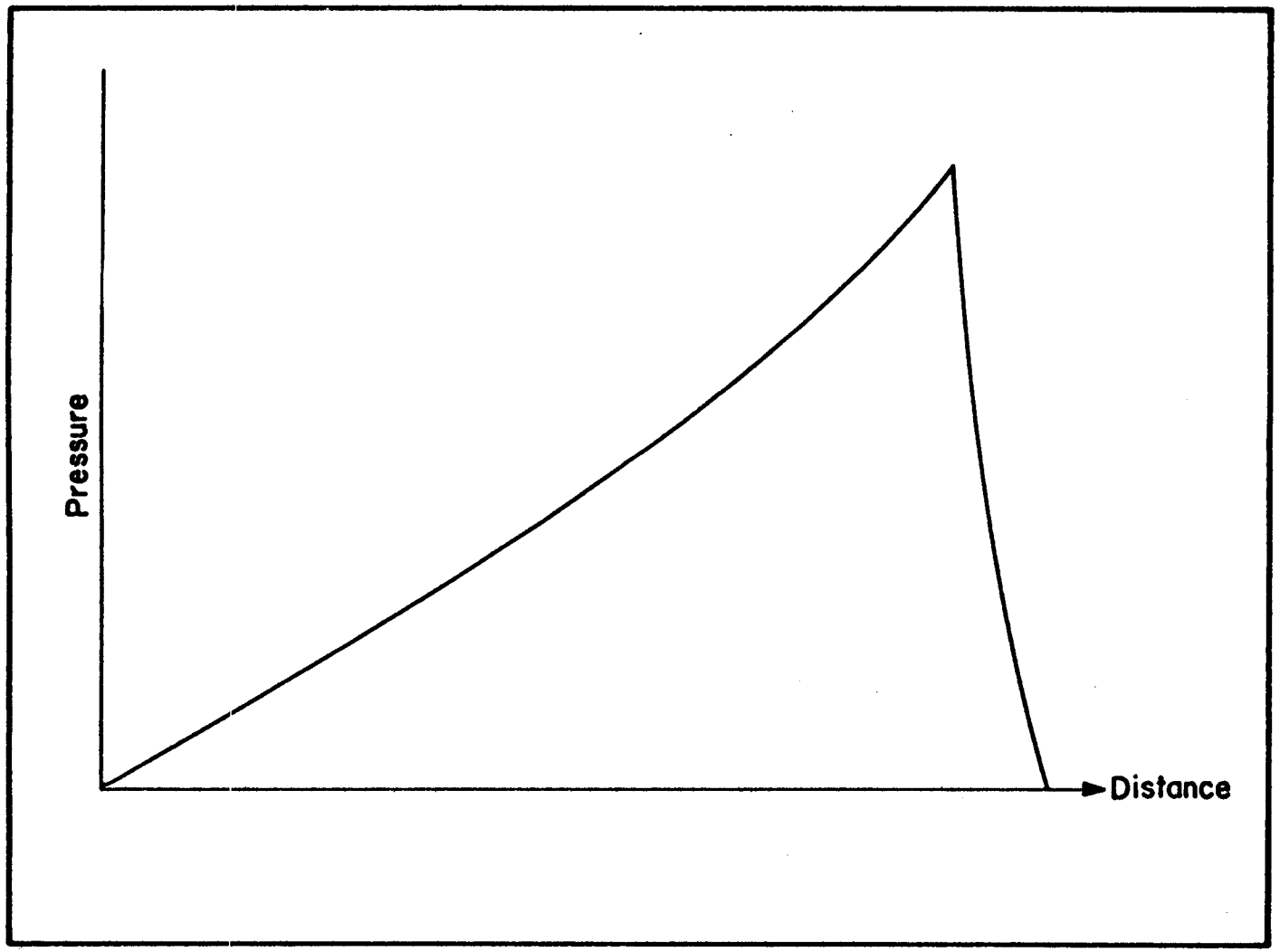

Figure 2. Typical Pressure Profile of a One Dimensional Shock Wave

p increases almost instantaneously to its peak value and then decreases toward zero behind the shock front. This jump marks the position of the advancing shock wave the propagation velocity, Σ, of the shock front is supersonic with respect to the undisturbed material, that is

$$\Sigma > C_0$$

where C_0 is the velocity of sound in the uncompressed medium ahead of the shock front. The propagation velocity, σ, for disturbances behind the front is greater than the shock velocity

$$\sigma + c > \Sigma$$

where c is the velocity of sound in the medium behind the shock front. The region of decreasing pressure is referred to as a rarefaction wave, or a simple expansion wave. The peak pressure is relieved by means of this rarefaction. The rarefaction gradually changes the entire profile as the shock progresses. The shock front has the shape of a hemisphere, it will move forward as a distrubance of decreasing peak pressure. From the assumption of an inviscid fluid, the pressure might be expected to decrease to zero at infinity. The computer solution by the method of von Neuman and Richtmyer requires the introduction of a pseudo-viscosity term that speeds the decay of the amplitude.

One further specification must be included in the Rankine-Hugoniot conditions for a strong shock wave. Entropy must increase across the shock front. The passage of a shock wave requires an increase in entropy of the supporting

medium. This dissipation is not yet provided in the Eulerian flow equations or the Rankine-Hugoniot equations. Fortunately, this further condition on shock propagation as well as the Rankine-Hugoniot relations can be put into a modified set of partial differential equations directly from the Eulerian flow equations presented above.

The Introduction of Dissipation

Shock surfaces appear in the differential equations as points where the velocity, density, internal energy and other variables of the fluid are discontinuous. The Rankine-Hugoniot jump conditions relate the two sides of the shock front. The Eulerian flow equations provide sufficient conditions for solutions in regions away from both sides of the shock (9). The process of applying the Rankine-Hugoniot conditions as boundary conditions on the flow equations; and thereby, solving the problem of the propagation of a shock wave is known as shock fitting.

J. von Neumann and R. D. Richtmyer (10), in order to avoid the difficulties inherent in solving two sets of conservation equations, devised a method of automatically handling shock motion in the numerical solution of the differential equations. Their method treats shocks automatically in a digital computer. It is based on the introduction of an artificial dissipative mechanism which has some analogy to the viscosity and the heat conduction which do exist in real fluids. The introduction of this artificial, dissipative

mechanism, or pseudo-viscosity, into the differential equations tends to smear the shock wave and change it from a discontinuity to a short region in which the variables change rapidly, but continuously. Even though this method does away with explicit application of the boundary conditions, the Rankine - Hugoniot conditions still hold across the shock and the approximation of smearing out the shock can be made to represent a transition zone as accurately as desired by limiting the width of the shock.

The artificial dissipative mechanism is introduced in the form of a pseudo-viscosity term which can be added to the pressure. Originally a term proportional to the square of the velocity gradient was used. Practical tests and analyses carried out by Landshoff (11) indicate that a linear combination of terms proportional to the first and second powers of the velocity gradient gave better results in the numerical calculation of shock problems. A similar expression has been used in the present work. The dissipation is designated as q and is given by

$$q = -c_1^2 \nabla\cdot\vec{V}\,(c_2 + |\nabla\cdot\vec{V}|) \qquad 2.9$$

where c_1 and c_2 are disposable constants. Setting $c_2 = 0$ would give the original von Neumann-Richtmyer equation. In the polar frame of reference, q is

$$q = -c_1^2\left(\frac{\partial(ru)}{r\,\partial r} + \frac{\partial w}{r\,\partial\theta}\right)\cdot\left(\left|\frac{\partial(ru)}{r\,\partial r} + \frac{\partial w}{r\,\partial\theta}\right| + c_2\right) \qquad 2.10$$

The Eulerian flow equations are easily converted to their new

form by replacing p by the sum of p and q.

The modified equations describe, not only isentropic flow; but also allow the description of large fluid motions such as shock waves. The theoretical formulation of the hydrodynamic model is complete except for a relation between the pressure and other fluid parameters. A thermodynamic equation of state which is valid at high pressures will be presented in the next section. This will allow the statement of the problem in a consistent set of equations which can be solved by the numerical method of finite differences.

The High Pressure Equation of State

One of the most general forms of an inviscid equation of state is the Mie-Gruneisen equation (12). This assumes a material in which the internal energy can be expressed as the sum of a thermal energy term and a volume dependent energy term. One form of the equation is

$$p - p_H = \frac{\gamma}{V}(e - e_H) \qquad 2.11$$

where p_H and e_H are the pressure and internal energy on the shock state curve, γ is a slowly varying function of the density called the Gruneisen ratio and V is the specific volume, $V = 1/\rho$.

The construction of an extended equation of state in the relatively low pressure range is based on the evaluation of the Hugoniot pressure, and the Gruneisen ratio from experimental information. The best source of data is from the

work at Los Alamos. Walsh, Rice, and McQueen (12) have performed numerous shock wave experiments which have given the Hugoniot curve for aluminum up to one megabar. In this region, the dependence of γ on the specific volume has also been determined. For convenience, these curves are expressed by equations of the following form,

$$S(x) = \sum_{n=0}^{3} A_n x^n$$

where S represents p_H or γ, $\mu = \frac{V_0}{V} - 1 = \rho/\rho_0 - 1$, and the A_n are constants. An application of the Rankine - Hugoniot energy relation allows the calculation of the internal energy along the Hugoniot curve once p_H is known.

Theoretical consideration is needed to extend the equation of state into the multi-megabar regions. It is believed that at pressures greater than approximately twenty megabars, the Fermi-Thomas (13) statistical model of atoms yields reasonable pressure volume relations at a temperature of absolute zero. Equation 2.11 together with an extrapolation of the Gruneisen ratio provides knowledge of the Hugoniot curve. This further knowledge can be used to refine the extrapolated value of the Gruneisen ratio.

The gap in the equation of state between one and twenty megabars is filled by interpolating the Hugoniot curve and the Gruneisen ratio between the experimentally and theoretically known points. This information is presented in numerical fits of the same form as equation 2.12. The necessary constants are given in Table I. A complete description

TABLE I

POLYNOMIAL FORMS AND CONSTANTS

FOR ALUMINUM

$$S(x) = \sum_{n=1}^{3} A_n x^n$$

ZERO DEGREE ISOTHERM, $S(x) = p_K$

V/V_o	A_1	A_2	A_3	Pressure (in megabars)
1.000 to .579	0.680	1.536	.468	0.000 to 1.486
.579 to .450	-1.574	5.116	-.206	1.486 to 5.003
.450 to .260	-8.715	11.620	-.620	5.003 to 52.00

HUGONIOT, $S(x) = p_H$

V/V_o	A_1	A_2	A_3	Pressure (in megabars)
1.000 to .650	.765	1.659	.428	0.000 to 1.000
.650 to .518	1.150	-.852	3.998	1.000 to 3.570
.518 to .300	-2.194	4.035	2.604	3.570 to 52.00

GRUNEISEN RATIO, $S(x) + \gamma_0 = \gamma$

V/V_o	A_1	A_2	A_3	
1.000 to .650	-5.193	12.098	-12.5500	2.13
.650 to .518	-4.513	6.800	- 3.7800	2.00
.518 to .300	-1.355	.439	.0404	1.59

of the process of constructing a multi-megabar equation of state has been published previously. (4,14).

The existence of an adequate equation of state now allows the collection of the equations which describe the proposed impact model. These will be put in a convenient form for numerical solution.

Dimensionless Differential Equations

For convenience in using a fast computer, all variables in the problem are scaled to prevent production of numbers outside the capability of the computer. A dimensionless form of the equations would also permit investigation of the possibility of applying results to problems involving different initial values.

The choice of a reference length is the first step in reducing the set of relations to a dimensionless form. This length, α , will be related to the size of the impinging micrometeoroid.

$$\alpha = f(r_M) \qquad 2.13$$

where r_M is the radius of the projectile. Radial distances are now measured in units of r/α ,

$$R = r/\alpha \qquad 2.14$$

Other variables are similarly made dimensionless.

$$\begin{aligned} D &= \rho/\rho_0 \\ P &= p/p_0 \qquad & Q &= q/p_0 \\ U &= u/c_0 \qquad & W &= w/c_0 \\ E &= e/e_0 \end{aligned} \qquad 2.15$$

The values of ρ_0 and p_0 are chosen quite arbitrarily. The quantities c_0 and e_0 are related to ρ_0 and p_0. The independent variable, t, is changed to the new parameter, T, by the relation,

$$T = c_0 t/\alpha \qquad 2.16$$

The angular variable, θ, is dimensionless.

The definitions in equations 2.14 - 2.16 can be substituted into the fluid equations that were given previously. The equation for conservation of mass becomes

$$\frac{\partial D}{\partial T} = -\frac{\partial(RDU)}{R\,\partial R} - \frac{\partial(DW)}{R\,\partial\theta} \qquad 2.17$$

The equations for conservation of momentum are now written

$$\frac{\partial(DU)}{\partial T} = -\frac{\partial(P+Q)}{\partial R} - \frac{\partial(RDUU)}{R\,\partial R} - \frac{\partial(DWU)}{R\,\partial\theta} \qquad 2.18$$

and

$$\frac{\partial(DW)}{\partial T} = -\frac{\partial(P+Q)}{R\,\partial\theta} - \frac{\partial(RDWU)}{R\,\partial R} - \frac{\partial(DWW)}{R\,\partial\theta} \qquad 2.19$$

These were made dimensionless by choosing c_0 so that

$$c_0^2 = p_0/\rho_0$$

The conservation of energy equation can be expressed in terms of the new variables if the quantity e_0 is subject to the following condition,

$$e_0 = p_0/\rho_0 = c_0^2$$

The new equation is

$$\frac{\partial(DE)}{\partial T} = -\frac{\partial(R(P+Q)U)}{R\,\partial R} - \frac{\partial(R(P+Q)W)}{R\,\partial\theta} - \frac{\partial(RDUE)}{R\,\partial R} - \frac{\partial(DWE)}{R\,\partial\theta} \qquad 2.20$$

The equation of state is simply transformed.

$$P = PH + \gamma D(E - EH) \qquad 2.21$$

where PH is p_H/p_0 and EH is e_H/e_0 ; γ is dimensionless.

The auxiliary equation for the artificial viscosity may be obtained by considering the constants A_1^2 and A_2 as resulting from the formulas

$$A_2 = C_2\, c_0/\alpha$$
$$A_1^2 = C_1^2\, \rho/\alpha^2$$

The constants, A_1^2 and A_2 , are chosen empirically to provide the correct order of magnitude for the viscous pressure term, rather than to fulfill theoretical relations to other parameters.

$$Q = -A_1^2\left(\frac{\partial(RU)}{R\,\partial R} + \frac{\partial W}{R\,\partial\theta}\right)\left(\left|\frac{\partial(RU)}{R\,\partial R} + \frac{\partial W}{R\,\partial\theta}\right| + A_2\right) \qquad 2.22$$

With the equations in the desired dimensionless form, it is now necessary to convert them to difference equations. The next chapter will discuss the method of finite differences. The required difference equations will also be obtained.

CHAPTER III

THE NUMERICAL METHOD

A consistent set of equations was obtained in the last chapter, which govern the space and time dependence of the material functions in the microparticle and the target. It is now necessary to solve these simultaneous equations.

There is no known analytic solution for this system of equations, and it is not anticipated that one will be found in the immediate future. (15). The highly developed state of electronic computers, such as the IBM - 7090 or IBM - 7094, makes the use of numerical methods feasible for reasons of both time and relative simplicity of processing. A well-posed, initial-value problem in fluid mechanics may be formulated and the method of finite differences employed to convert the differential equations to algebraic difference equations. These difference equations may be readily solved on the large computers.

To indicate the way in which the equations are differenced, consider a function $f = f(x,t)$. The change in this function with time can be approximated as,

$$\Delta f(x,t) = f(x,t+\delta t) - f(x,t)$$

where δt is a small time increment. This operation is defined as a forward difference. A backward difference is

$$\Delta f(x,t) = f(x,t) - f(x,t-\delta t)$$

A more widely used and usually more accurate type of difference is the central difference

$$\Delta f(x,t) = f(x, t+\tfrac{1}{2}\delta t) - f(x, t-\tfrac{1}{2}\delta t)$$

The accuracy of all three formulas depends on the size of the time increment, δt. The partial derivative may be written

$$\frac{\partial f}{\partial t} = \frac{\Delta f}{\delta t} = \frac{f(x, t+\frac{1}{2}\delta t) - f(x, t-\frac{1}{2}\delta t)}{\delta t}$$

when central differencing is employed.

As an example of a complete equation translation, that is, the transformation of a partial differential equation to an algebraic finite difference equation, consider the equation of continuity in one dimension. A one space dimension net is illustrated in Figure 3. The symbols, δx and δt represent small increments of the independent variables, x and t. The grid, or finite difference mesh, for x and t is defined as the set of cells numbered, J, and the times labeled, N.

$$J = 1,2,3,\ldots\ldots, J_{final}$$

$$N = 0,1,2,3,\ldots, N_{final}$$

A function value f(x,t) can be represented at the center of any cell in the net as

$$f(J\cdot\delta x\,;\, N\cdot\delta t) \equiv f_J^N$$

A function value at either side of a cell is

$$f_{J-1/2}^N \qquad\qquad f_{J+1/2}^N$$

for a time, $N\cdot\delta t$.

The continuity equation is

$$\frac{\partial \rho}{\partial t} = -\frac{\partial(\rho v)}{\partial t}$$

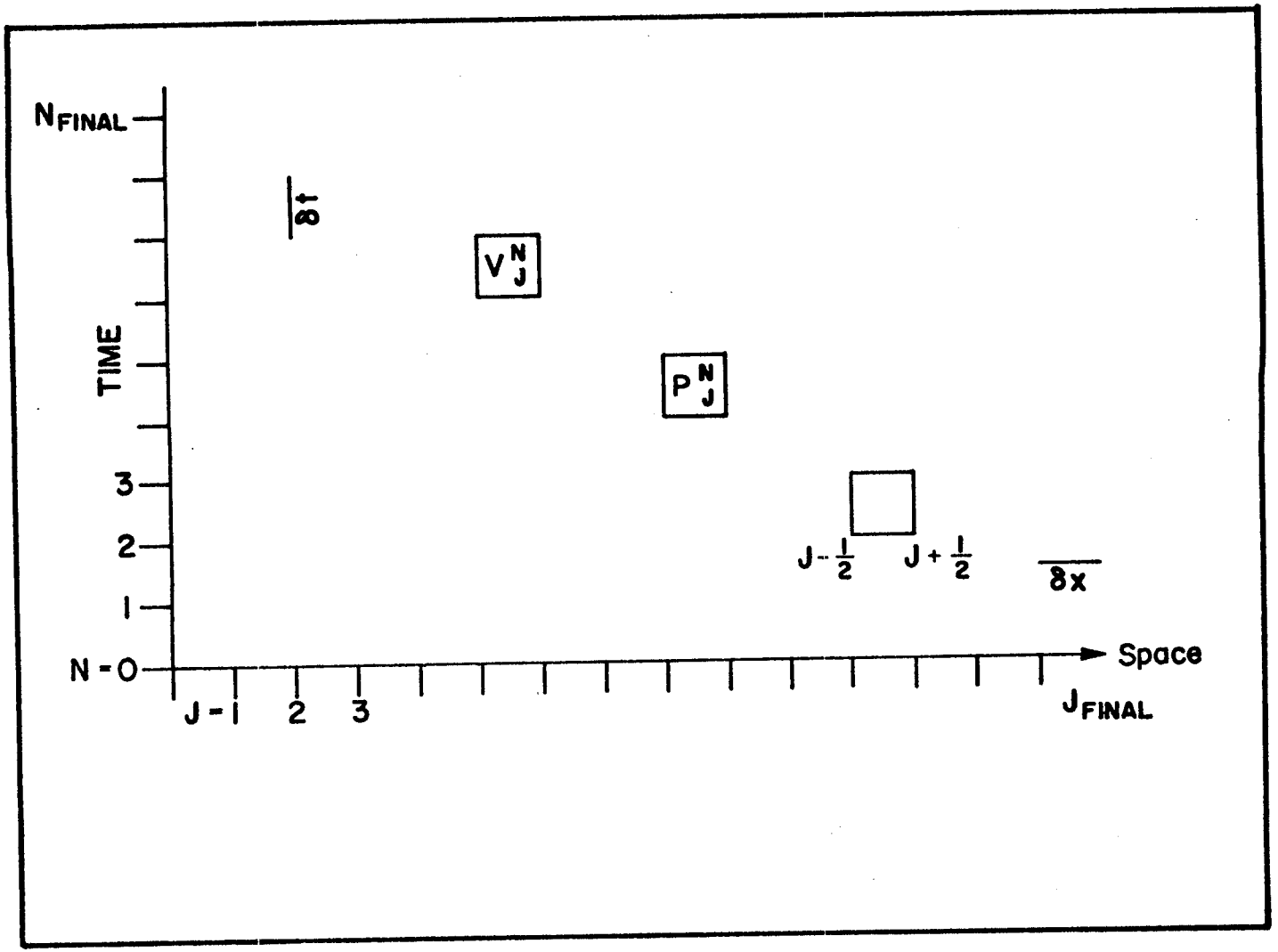

Figure 3. One Space Dimension Finite Difference Net

where v is the linear flow velocity. Values of ρ_J and v_J will be considered as representative values of the density and velocity at the center of the J-th cell. A simple application of central differencing yields

$$\frac{\rho_J^{N+1} - \rho_J^N}{\delta t} = - \frac{(\rho v)^N_{J+1/2} - (\rho v)^N_{J-1/2}}{\delta x}$$

Central differencing is used for the space derivatives while a forward difference replaces the time derivatives. This is the general choice made in all equations to be discussed. The use of forward time differencing is desired to conserve memory space in the computer. Such a procedure requires only two sets of space points in storage at any stage of the calculation. The substitution indicated above gives usable approximations for all net points except the cells, J = 1 and J = J_{final}. Such special cases require the use of forward and backward differences to replace the prescribed, central differences.

The Two Dimensional Difference Equations

The problem for solution has spherical symmetry and, for this reason, the equations for solution were converted to spherical coordinates. Since the problem has symmetry, a vertical impact may be followed, after a judicial selection of coordinates, by plots on only a part of one quadrant in a single plane. The coordinates are R and θ. For a normal impact, the axis of R for $\theta = 0$ is taken vertically through the initial point of contact between the microparticle and

the surface of the semi-infinite slab. The origin of coordinate, at which R = 0, is taken at a little more than twice the diameter of the microparticle above the point of initial impact. The plot of the entire affected volume of the impact is obtained by rotating the selected plane-mentioned above the vertical line R for $\theta = \frac{\pi}{2}$. The region of impact on the plane is divided into a number of cells, as shown in Figure 4. The equations are differenced for this mesh. The individual cells are designated in space by M in R direction and L in the θ direction; so that,

$$M = 1,2,3,\ldots, M_{final} = MF$$
$$L = 1,2,3,\ldots, L_{final} = LF$$

The time is measured in units of N·DT, where DT is a small but finite increment. The radius at the center of each cell is given by

$$R_M = RO + DR \cdot (M - .5)$$

and at the sides of a cell by

$$R_{M-1/2} = DR \cdot (M - 1), \quad R_{M+1/2} = DR \cdot M + RO$$

The other two boundaries of a cell are rays of constant angle, which are separated by a constant, $D\theta$. The area of any cell at a distance, R_M, from the orgin is

$$AA_M^L = R_M \cdot DR \cdot D\theta$$

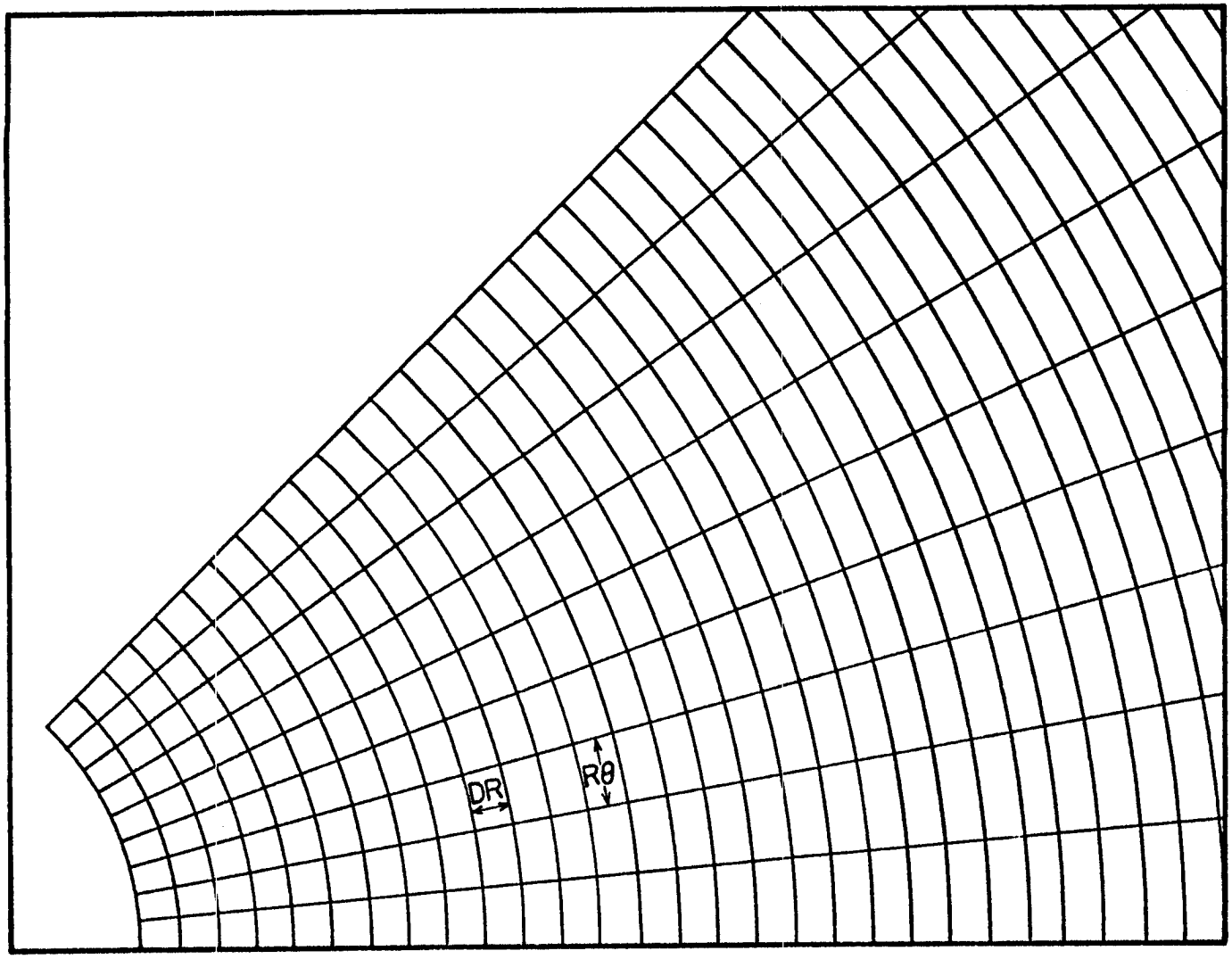

Figure 4. Two Space Dimension Finite Difference Mesh

Values of the density, the pressure, the pseudo-viscosity, the two components of the material velocity, and the energy are defined at the center of each cell and are regarded as average properties of the material within a cell. Each variable is designated as f_M^L . This identification follows from above and refers to cell number M along R and the cell number L in the Θ direction. Given values for all cells at a time $T=0$, the problem is to carry the values of the quantities stored for each mesh point forward by a small, later time, DT.

Forward time differences are used for all time derivatives and all spatial derivatives are initially written in terms of central differences. Equation 2.17 can now be written as

$$\frac{D_M^{L\,N+1} - D_M^{L\,N}}{DT} = -\frac{R_{M+1/2}^{L\,N} D_{M+1/2}^{L\,N} U_{M+1/2}^{L\,N} - R_{M-1/2}^{L\,N} D_{M-1/2}^{L\,N} U_{M-1/2}^{L\,N}}{R_M \cdot DR} - \frac{D_M^{L+1/2\,N} W_M^{L+1/2\,N} - D_M^{L-1/2\,N} W_M^{L-1/2\,N}}{R_M \cdot D\theta}$$

To compress notation, see Figure 5, quantities at M, L -1/2 are designated side one; at M - 1/2,L, side two; at M, L+1/2, side three; and at M+1/2,L, side four. Using this shorthand, and factoring AA_M^L in the denominator, the finite difference form for the conservation of mass equation becomes

$$D_M^{L\,N+1} = D_M^L + \frac{DT}{AA_M^L}\left[D\theta\left((RDU)_2 - (RDU)_4\right) + DR\left((DW)_1 - (DW)_3\right)\right] \qquad 3.1$$

All quantities on the right are for time N•DT. If these are

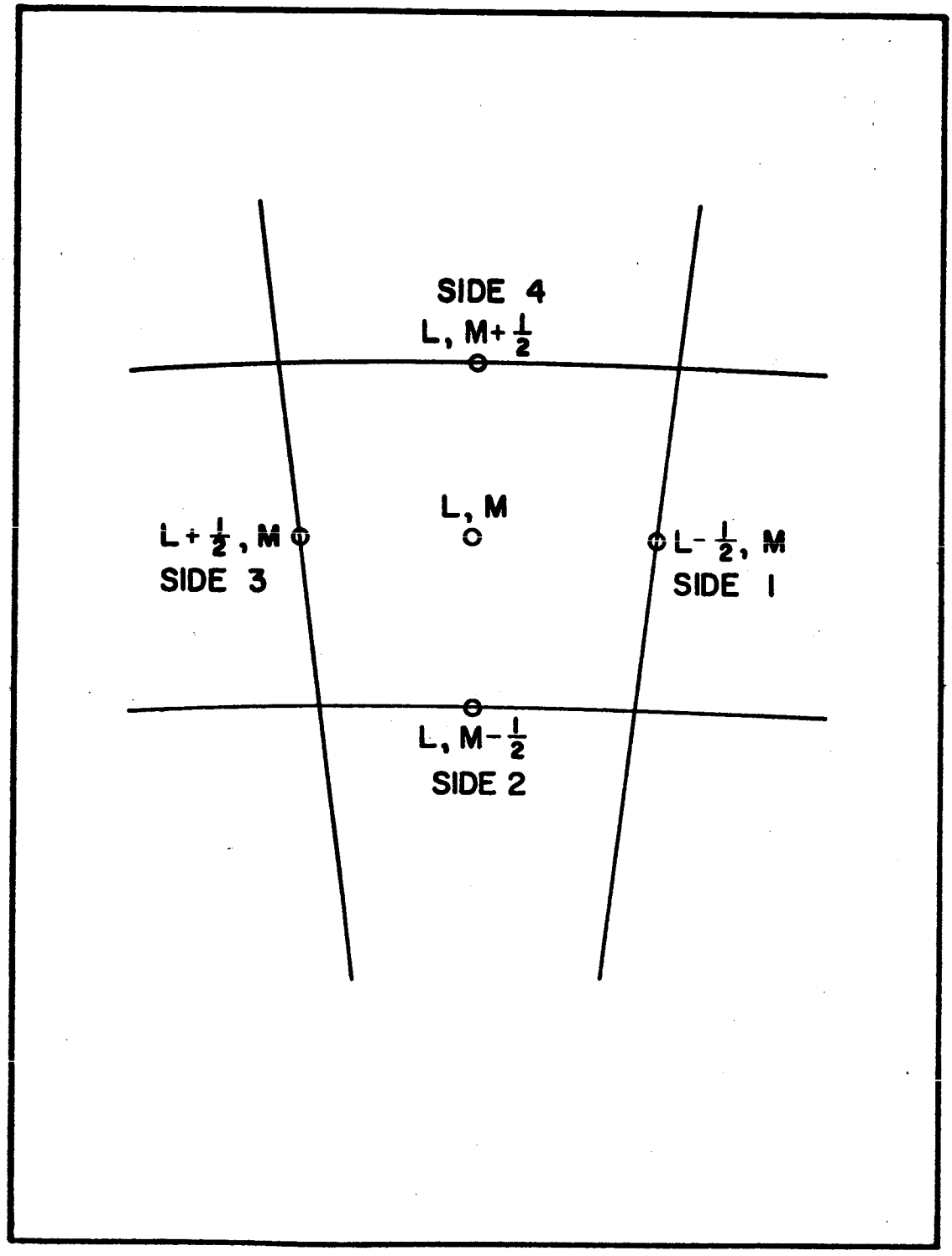

Figure 5. Cell Boundary Notation

all known, or prescribed, then the density, $D_M^{L\ N+1}$, for the time (N+1)·DT can be calculated.

The other conservation equations are treated similarly.

Radial equation of motion:

$$(DU)_M^{L\ N+1} = (DU)_M^L + \frac{DT}{AA_M^L}[R\cdot D\theta((P+Q)_2 - (P+Q)_4) + D\theta((RDU)_2 U_2 - (RDU)_4 U_4) + DR((DW)_1 U_1 - (DW)_3 U_3)] \qquad 3.2$$

Tangential equation of motion:

$$(DW)_M^{L\ N+1} = (DW)_M^L + \frac{DT}{AA_M^L}[DR((P+Q)_1 - (P+Q)_3) + D\theta((RDU)_2 W_2 - (RDU)_4 W_4) + DR((DW)_1 W_1 - (DW)_3 W_3)] \qquad 3.3$$

Conservation of energy:

$$(DE)_M^{L\ N+1} = (DE)_M^L + \frac{DT}{AA_M^L}[D\theta(R(P+Q)_2 U_2 - R(P+Q)_4 U_4) + DR((P+Q)_1 W_1 - (P+Q)_3 W_3) + D\theta((RDU)_2 E_2 - (RDU)_4 E_4) + DR((DW)_1 E_1 - (DW)_3 E_3)] \qquad 3.4$$

The two auxiliarly equations are independent of time and are simply translated

$$P_M^L = PH + G\cdot D_M^L(E_M^L - EH) \qquad 3.5$$

The new parameters are easily identified:

$$PH = (p_H)_M^L \qquad G = \gamma_M^L \qquad EH = (E_H)_M^L$$

All three are functions of the density

$$PH = A\cdot T + B\cdot T^2 + C\cdot T^3$$

$$EH = T\cdot PH/2(T+1)$$

$$G = G_0 + A'\cdot T + B'\cdot T^2 + C'\cdot T^3$$

where T = μ = $D^L_M - 1$. The parameters A,B,C, G_0 ,A', B', C' represent constants in the fitted polynomial functions.

The formula for the pseudo-viscosity is

$$Q^L_M = - \frac{A_1^2}{AA^L_M} (Y) \cdot (|Y| + A_2) \qquad 3.6$$

where $Y = D\theta [(RU)_4 - (RU)_2] + DR [W_3 - W_1]$

The above system of equations is explicit and the solution may be moved forward, continuously, by means of simple algebra. Equation 3.1 gives a value for the new density, which is then used to find the new velocities from equations 3.2 and 3.3. Continuing with these known values, internal energy is found from equation 3.4. At the new time level, the quantities D^{N+1} , E^{N+1} , U^{N+1} , and W^{N+1} enable the additional equations to be solved for new values of the pressure, P, and the pseudo-viscosity, Q. The new profiles (set of values $f^{L\ N+1}_M$) then become the starting point for the next advance in time.

The formulated equations have values defined at cell boundaries which are not actually carried in the problem. Consider

$$f^L_{M+1/2} = f(\Theta_j, R_i + \tfrac{1}{2} DR)$$

This is most easily replaced by

$$f^L_{M+1/2} = (f^L_{M+1} + f^L_M) / 2 \qquad 3.7$$

which is a simple averaging formula. Unfortunately, if all half-step expressions in the flow equations were replaced by approximations of this type (which is designated as Type I),

the resulting system would be unconditionally unstable. (16). This means that any solution that is obtained numerically would become oscillatory as time progresses, and the amplitude of the oscillations would increase without limit. This difficulty may be avoided by the selection of other types of formulas for the approximations. These methods correspond to a more accurate approximation of the derivative, while the system of flow equations remain formally in a central differencing representation. Essentially, one dimensional forms are used, since values on the sides one and three are differenced for one dimension in the L direction for each M. Values on sides two and four are differenced in the M direction for each L. Only values at the (+) 1/2 sides are discussed since transition to the (-)1/2 side is effected by subtracting one from the cell index.

To replace the unsuccessful averaging method, equation 3.7, which is Type I, consider two other approximating formulas,

Type II
$$f_{J+1/2} = \begin{cases} f_J & V_T > 0 \\ 0 & V_T = 0 \\ f_{J+1} & V_T < 0 \end{cases} \qquad 3.8$$

Type III
$$f_{J+1/2} = \begin{cases} (6f_J + 3f_{J+1} - f_{J-1})/8 & V_T > 0 \\ 0 & V_T = 0 \\ (6f_{J+1} + 3f_J - f_{J+2})/8 & V_T < 0 \end{cases} \qquad 3.9$$

The quantity V_T is a test velocity, either $(U_M^L + U_{M+1}^L)$ or $(W_M^L + W_M^{L+1})$. Since V_T indicates the direction of fluid flow, the difference approximation responds to changes in flow direction. Type II differencing yields a

forward or a backward difference formula depending on the sign of V_T . Cell values found from this approximation result in a diffusion, or second order smearing effect. (16). Numerical stability of the solution is improved by this diffusion. The magnitude of this effect assists in avoiding excessive spreading of the shock fronts in the finite difference net. Simple velocity and energy terms are evaluated by use of Type II differencing.

Type III differencing is the result of a quadratic fit of $f(x)$ through the point of interest. Type III is a better approximation than either Type I or II, since four cell values contribute to the function value. Mass flow terms and densities are found by Type III differencing. The stability of the equations resulting from use of Types II and III differencing allows the use of Type I differencing for some function values. A more extensive discussion of these formulas and their application may be found in works by Longley (16) and Sodek (14).

At certain points of the net, the Type III approximation may not be used since values for four cells are not available. Near the points L = 1 and L = L_F, M = 1, and M = M_F, Type I differencing is used for all quantities in order to avoid the difficulty of having the computer seek nonexistent cells. Pseudo-points are defined for cells not actually in the mesh by means of formulas developed by Ables (17). For a point just prior to L=1, say LO, the functional value for use in Type I differencing is given by

$$f_M^{LO} = 3f_M^1 - 3f_M^2 + f_M^3 \qquad 3.10$$

Similarly, for a cell labeled LF+ 1 which is just past the last defined cell,

$$f_M^{LF+1} = 3f_M^{LF} - 3f_M^{LF-1} + f_M^{LF-2} \qquad 3.11$$

These same expressions are used for points MO and MF+ 1 which are defined exactly as LO and LF+1.

The selection of means for evaluating all terms in the modified flow equation provides an algebraic procedure, very straightforwardly programmed for a digital computer. Then the equations will yield a solution for two-dimensional, fluid motion, including shock waves and other large-scale fluid movements.

Finite Difference Mesh Configuration and Cycling

The selection of a single plane to illustrate the solution and to provide the net that is required for the computer solution was discussed earlier in this chapter. Both the microparticle, before impact, and the free surface of the semi-infinite slab must be included in the plane. A possible positioning of a polar coordinate system on a practical plane is illustrated in Figure 4. The microparticle is represented by a semicircle of radius R_M. The position of the face of the semi-infinite target is initially given by

$$R \sin\theta = S \qquad 3.12$$

where S is a constant distance measured in the same units as R. In such a mesh, there are three possible kinds of cells; cells full of aluminum, empty cells, and mixed cells, which are partially filled with aluminum and partially empty.

These mixed cells contain a material - vacuum boundary. Each mixed cell is marked with a parameter called the partial area, A_M^L . It is a quantity which signifies the amount of area of a cell that is filled by aluminum.

The initial information to the computer program is the free velocity of the microparticle, V_o, together with the locations and partial areas of the mixed cells.

The circumference of the micrometeoroid is given by the equation of a circle in polar coordinates,

$$b^2 - a^2 + R^2 - 2bR\sin\theta = 0 \qquad 3.13$$

where a is the radius of the circle with center at $(b, \frac{\pi}{2})$. The partial area of a cell is determined by computing the points of intersection of this equation with the coordinate lines of constant R and constant θ and then by integrating between these limits. This process is illustrated in Figure 6. The diagram shows a typical mixed cell in the lower half of the projectile. There is a sign change for the upper half of the microparticle. These calculations were made independently of the main computer program on an IBM-650.

The motion of the microparticle as well as the boundary of the target is followed by changing the partial areas in the mixed cells and by the appearance and disappearance of mixed cells. The fluid parameters of a mixed cell are calculated in the manner that is outlined, above, for aluminum cells. The major problem posed by the existence of mixed cells is that of changing the partial areas in time. Perhaps the simplest possible method is to use an approximate formula

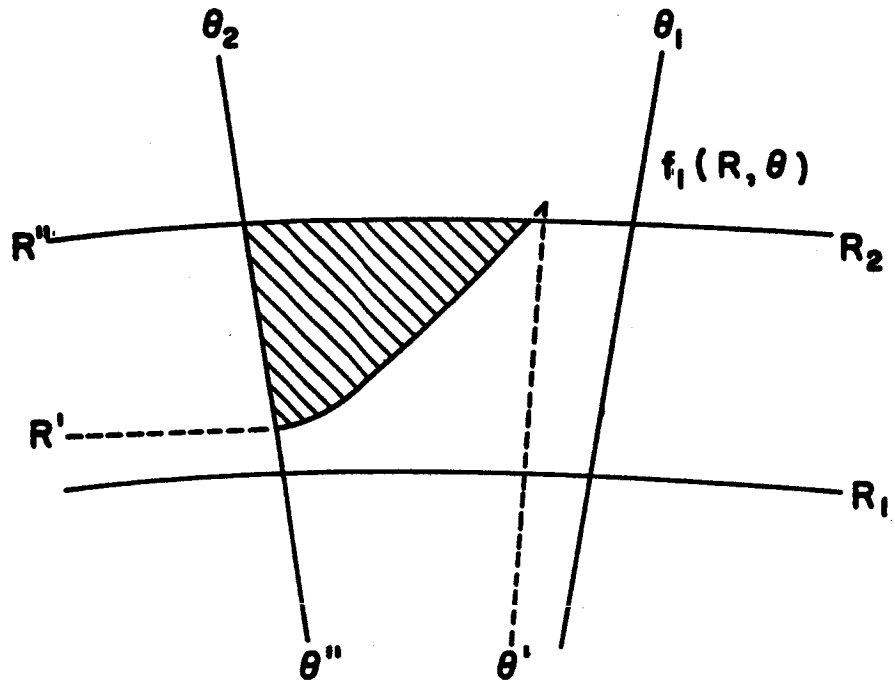

$f_1(R, \theta)$ is the equation of a semicircle.

$R_1, R_2, \theta_1, \theta_2$ are cell boundries.

$R', R'', \theta' \theta''$ are limits of integration.

$$A = \int_{\theta'}^{\theta''} \int_{R'}^{R''} \left[R_2 - f_1(R, \theta)\right] \, dR \, d\theta$$

Figure 6. Initial Partial Area Calculation

based on the known velocity components.

$$A_M^{L\,N+1} = A_M^L - \Delta R \cdot \Delta \Theta \qquad 3.14$$

where

$$\Delta R = U_M^L \cdot DT$$
$$\Delta \Theta = W_M^L \cdot DT$$

and DT is the elapsed time of one iteration cycle.

The calculation of the new partial areas is the last step of a calculation cycle. The whole mesh has been moved forward by a time step, DT. The mixed cells, which may contain a moving boundary, must be changed from time to time. A test must be made after the end of each time step to ascertain whether any of the mixed cells should be replaced by either a full, or an empty cell. Either possibility requires the construction of a new mixed cell. The partial area of a mixed cell might be calculated greater than the actual area of the cell, or as vanishingly small. In both cases, the cell is changed.

In summary, the solution is obtained as follows, the values of all parameters are found by successive applications of equations 3.1 through 3.6 for all full and mixed cells. The parameters of an empty cell cannot be changed by these equations. Empty cells are changed only by movements of mixed cells. Then, the new partial areas are found and mixed cell changes are made, if necessary. This procedure can then be repeated to give a numerical solution for the whole region as time increases with each calculation cycle.

Quality of Solutions

There are two important questions to be asked concerning the accuracy of a numerical solution to an initial value problem. (18):

1. Do both the partial differential equations and the difference equations possess unique solutions?
2. If the answer to 1 is yes, is the solution that is obtained by solving the difference equations, step by step, actually a sufficient approximation to the true solution of the given problem?

Full and completely rigorous answers to these questions are not available. A unique solution is judged to exist if the physical problem is well defined. It is generally believed that the compressible fluid equations give rise to a system of partial differential equations which define a well-posed, initial-value problem. (19).

The second question concerns the convergence of the approximate solution to the true solution. The true solution is not known for comparison. The system of difference equations is examined, somewhat empirically, for convergence. Different combinations of the increments, DR, DΘ, and DT are used and the resulting solutions are compared. If these different solutions agree very closely, then a good solution is probably being obtained.

A more encouraging condition can be suggested from the Equivalence Theorem of Lax (20):

> Given a properly posed initial value problem and a finite-difference approximation to it that satisfies the consistency condition, stability is the necessary and sufficient condition for convergence.

The consistency condition requires that the resulting numerical solution depend continuously on the initial data and that the difference equations go over to the differential equations as DT, DR, and Dθ approach zero. The first part of the condition is satisfied by the mechanism of the finite difference method by which the solution progresses from the known to the unknown. The second part of the consistency condition is satisfied, since this is the usual method of deriving the hydrodynamic flow equations. With the idea established that stability implies convergence, the concept of stability will be examined.

Since numerical approximation methods are used, it is expected that there is a small difference between the true solution and the computer solution,

$$\epsilon = f(R, \theta, T) - f(M \cdot DR, L \cdot D\theta, N \cdot DT)$$

The solution is stable if this error remains small or grows smaller. The solution is unstable if ϵ grows without limit. When the computer results indicate profiles with exceptional, oscillatory behavior, the particular solution is judged unstable. It has been determined that instability can be corrected by the proper choice of the mesh ratio, $\Delta\vec{X}/DT$. (21). The position vector is $\vec{X} = [R, \theta]$.

One well-known relation in the field of fluid dynamics is the Courant condition (22),

$$\Delta\vec{X}/DT \equiv c_m > c$$

that is, the mesh speed c_m must be greater than the sound speed which is the greatest velocity at which disturbances may be propagated from place to place in an elastic medium. For problems involving shocks and large material velocities, this restraint is insufficient.

Richtmyer (22) has shown for some cases a more suitable requirement is

$$c_m > c + |\vec{V}|$$

where $\vec{V}$ is the material velocity. This condition recognizes that disturbances move with the velocity of sound plus the velocity of the flowing medium.

In the problem to be discussed, the medium is usually highly compressed. The flow velocity and the sound velocity are roughly of the same order of magnitude. The following approximation, then, is made to the above condition,

$$\Delta\vec{X}/DT \geq 2\vec{V}$$

In one-dimensional tests, however, this relation prescribed a mesh ratio which was about five times too large. (14). In practice, DR and Dθ are fixed and DT is varied to satisfy requirements for stability. The actual condition used to check stability is written

$$DT \leq \frac{1}{10}\sqrt{\frac{(DR)^2 + R_0^2(D\theta)^2}{\hat{U}^2 + \hat{W}^2}} \qquad 3.15$$

where $\hat{U}$ and $\hat{W}$ are the maximum flow velocity components occurring in the solution and R_0 is a typical radius of the finite difference mesh.

Development of Computer Program

The computer code for solving the finite difference equations was written for an IBM-7090 computer. The size of the computer was demanded by the requirement that an accurate numerical approximation of the solution be obtained. Tests have shown that between fifty and one hundred divisions are needed for good resolution in each space direction. In the radial direction, the net was marked by sixty cells. In the angular direction, there were initially thirty-five cells covering a sector of 45°. The IBM-7090 has a storage capacity of approximately 32,000 words. Of this storage, about 25,000 words were used for storage of variables for each point of the finite difference mesh. There were twelve parameters defined and stored for each fluid cell:

D, Density in the cell.

U, radial velocity.

W, tangential velocity.

E, internal energy.

P, pressure.

Q, artificial dissipation.

CU, radial velocity at time N+1.

CW, tangential velocity at time N+1.

CE, internal energy at time N+1.

A, partial area (if any). NT, a name tag denoting the kind of cell; (+) for a full, aluminum cell, (-) for a mixed cell, and (0) for an empty cell.

CD, density in a cell at time N+1.

The computer code was written in FORTRAN and in FAP. FORTRAN is a high level computer language which, with slight changes, is acceptable to a wide assortment of large digital computers. It is not, however, the basic machine language of any machine and must, therefore, be translated into the basic machine language of the computer being used. This is accomplished generally, in two steps; the first being a translation to a symbolic assembly language, the second being to assemble the symbolic language program into a basic machine language program. FAP, FORTRAN ASSEMBLEY PROGRAM, is the symbolic language associated with Fortran II. The translation process required by programs written in FORTRAN is less efficient, that is, produces more instructions, than programs written in FAP or basic binary machine language. In order to conserve storage, part of the computer code 'DRAW', developed to solve the modified flow equations, was written in the symbolic language. The final program occupied about 6,500 words of the computer's memory.

To solve the difference equations on a 7090, a logical calculation path must be developed for use by the computer. This process is illustrated, in a rather general way, by Figure 7. Calculations are performed for each dependent variable in each cell corresponding to the directions of the

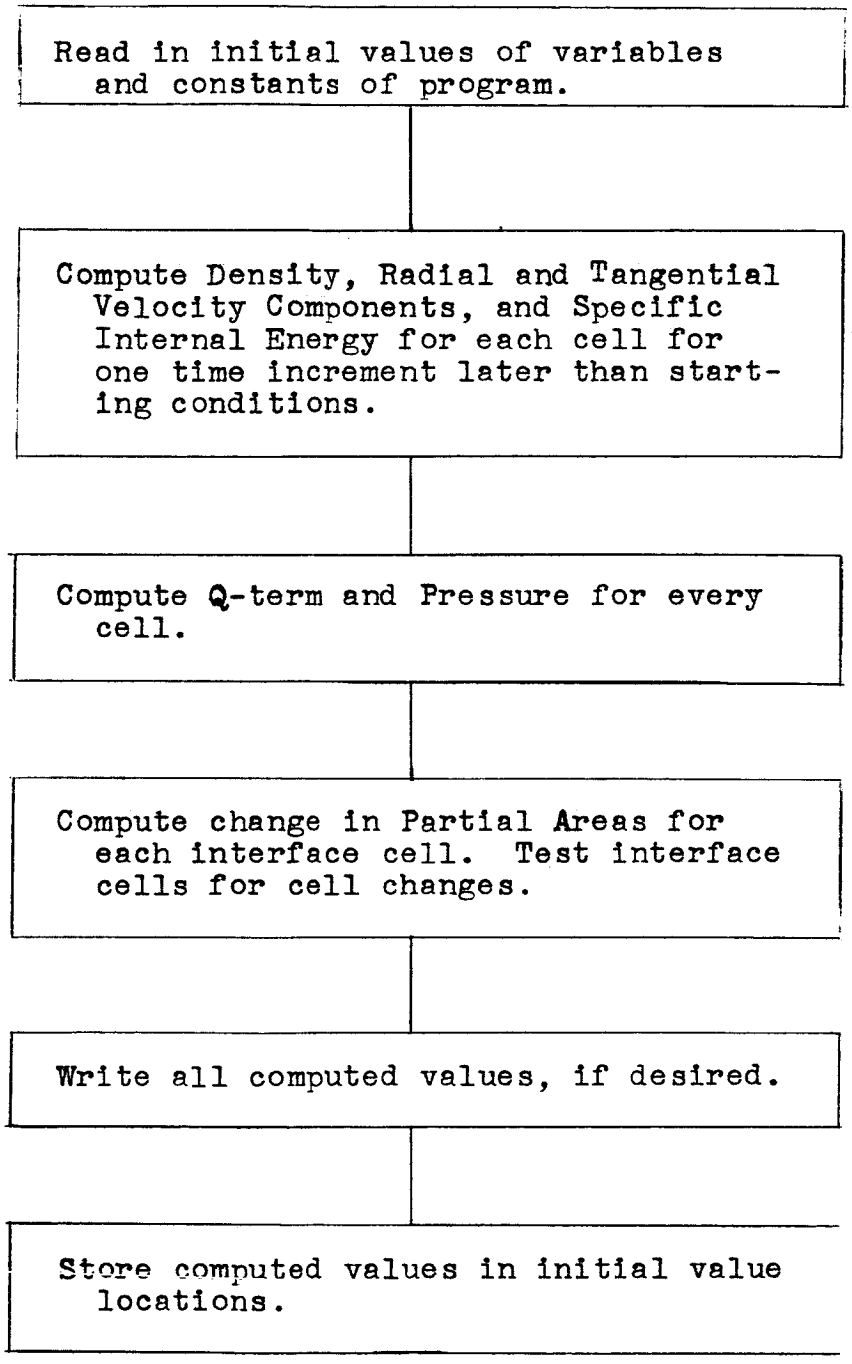

Figure 7. Computer Flow Diagram

difference equations. Other monitoring is required and performed by the computer code to check the mesh configuration and impose boundary conditions.

The cycling of the program would be as follows: one first calculates the values at time N+1 for the whole mesh using equations 3.1-3.4 for all full and mixed cells. Equation 3.14 is used to find the new partial area for all mixed cells. Boundary cell changes are then made if there are any. The new values of pressure and artificial dissipation are then found from equations 3.5 and 3.6. After the completion of a cycle, the results may, or may not, be printed out under computer program control. The new values for the variables replace the initial values so that the cycle may begin again.

CHAPTER IV

DEVELOPMENT AND PRESENTATION OF SOLUTIONS

The set of difference equations developed and programed for a computer solution have sufficient versatility to yield a solution for any arbitrary initial values and boundary conditions. The basic initial value necessary for a solution is the free space velocity of the incident micrometeoroid. The physical properties of aluminum under normal conditions supply the further necessary initial value information. Boundary conditions must be applied to the modified flow equations to insure the proper representation of material-vacuum-interfaces and symmetry properties assumed in the problem.

After obtaining the solutions for six different impact velocities, the numerical data is reduced by selective plotting of the space variation of the fluid variables at different instants of time. This chapter presents a survey of the information obtained by using the hydrodynamic model.

A series of curves illustrating the typical behavior of the pressure, velocity, and density are shown as functions of space and time. Further analysis of crater growth and peak pressure decay are also portrayed graphically. The dominant features of the solutions for all impact velocities

considered are the appearance of two shock waves at the point of initial contact and the formation of a cavity behind the penetrating projectile. Flow patterns peculiar to the spherical shape of the incident micrometeoroid are also displayed.

Initial Values

The basic operation of the finite difference method consists of moving from the known to the unknown. A completely specified net at one time is advanced by a small step in time. The action is then repeated indefinitely to develop a numerical solution. To start the solution, at time equal zero, a simple configuration is chosen. Just prior to the beginning of the calculations, the leading point of the micrometeoroid is in contact with the semi-infinite target. This is called the point of impact and lies on an axis normal to the target. The material velocity of the projectile is identical with its free space velocity, V_o. The material of the target is at rest. Both projectile and target are considered to be inviscid fluids during the flow that follows the impact. The density of both bodies is that of normal aluminum. Other fluid parameters such as the internal energy and pressure, and the pseudo viscosity are initially zero. Figure 8 illustrates the prescribed conditions.

In addition to these initial values, further conditions must be applied during the running of the computer program.

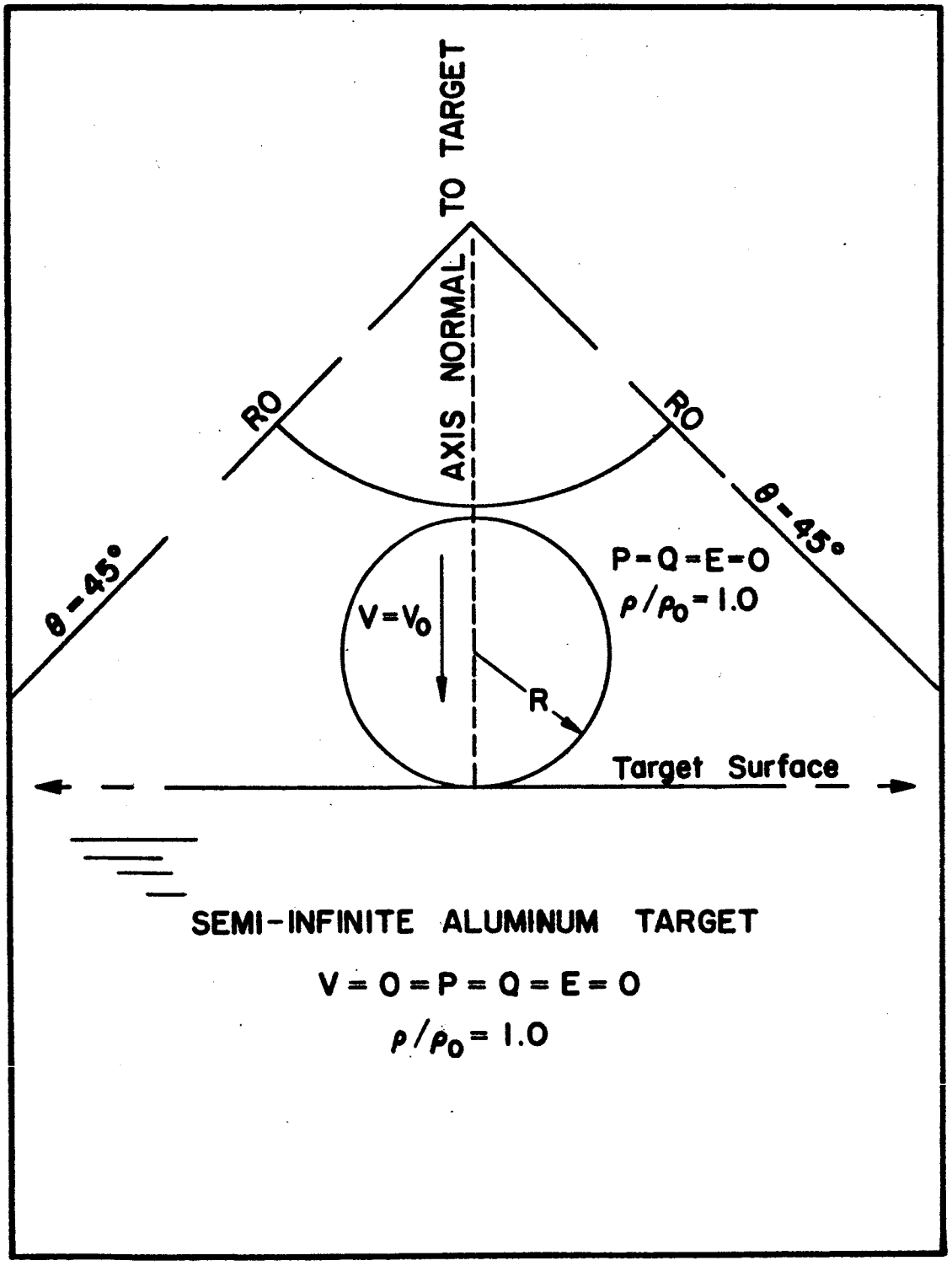

Figure 8. Initial Value Illustration

Boundary Conditions

Several boundaries appear in the formulation of the impact problem. Each must be subject to specialized treatment. The region of interest is taken as a sector of one quadrant (see Figure 8) of a polar coordinate system with the variables R and Θ. The initial point of contact is on the axis. The application of this condition is accomplished by requiring that no mass flow across this axis. A material-vacuum interface requires specification of zero pressure on such a line. This is accomplished with respect to the finite difference mesh by setting the pressure in a cell containing some aluminum material and some empty space equal to zero on the side or sides of the cell adjacent to the vacuum. Apart from this restriction of no applied force, the aluminum-vacuum boundaries are free to move and are moved as indicated by the velocity of the solid material in the mixed cell. As material flows out, density cannot be less than in the original solid. The computer program also monitors the differencing schemes to prohibit averaging across an interface. Fluid properties are not averaged between empty and full cells.

The Solutions

The finite difference method that is described in the previous chapter, complemented by the necessary initial conditions and boundary specifications was used to obtain

solutions for the hydrodynamic model for six different impact velocities. The numerical results evaluate the density, the pressure, the specific internal energy, and the two components of the material velocity at cell centers; that is these variables as functions of R and Θ, at discrete instants of time. The quantity of numerical data produced by the computer is enormous. The description provided by the hydrodynamic model is best presented in the form of graphs which show the preceeding variables at selected instants as the impact proceeds in time. The bulk of the solutions are presented in a special report, "Two Dimensional Plots of Solutions for a Hydrodynamic Model of Microparticle Impact." This report is available at the Research Foundation of Oklahoma State University. The following sections give illustrations of the important results and the nature of the solutions.

Organization of Solutions

The six velocities selected for computations range from slighty over the velocity of sound in aluminum to near the fastest possible velocity of a micrometeoroid in our solar system. The six velocities are:

Case I: V_o = 5.68 km/sec. = 17,620 ft/sec.

Case II: V_o = 15.16 km/sec. = 49,720 ft/sec.

Case III: V_o = 23.69 km/sec. = 77,000 ft/sec.

Case IV: V_o = 36.00 km/sec. = 118,000 ft/sec.

Case V: V_o = 47.38 km/sec. = 155,400 ft/sec.

Case VI: $V_o = 60.64$ km/sec. = 200,900 ft/sec.

A number of initial impact velocities were used in the calculations in order to investigate differents velocity regions. Since nonlinear equations are used to describe the phenomena, one sample case cannot be scaled with the velocity. The principles of similitude do not apply here.

The step by step description of the early progress of the hypervelocity impact are first illustrated graphically by profiles which show the variation of material velocity and density along the normal axis of the target at different times. Two dimensional plots are shown in which a plane bounded by the axis of symmetry and for θ equal to a constant. The volume distribution of the variables is obtained by rotating the two dimensional plots around the normal axis. The values at an instant of time are shown by lines of constant density, by isobars, and by arrows that show the magnitude and direction of the velocity. Since the volume distributions of all the variables is symmetric about the axis of symmetry, the velocity is entirely contained in the two dimensional plot.

The illustrations presented show the initiation of shock waves at the point of impact and subsequent dissipation as larger areas and free surfaces are encountered. Flow patterns for the pressure and material velocity for Case V is presented with comments on the chief features. Graphs of the time history of free surface motion are then presented for several of the cases considered.

A late time difficulty is pointed out in a group of figures showing constant density fields for Case V. The resulting disturbance apparently does not move quite correctly in the lateral direction. This inconsistency can be traced to faults in the equation of state used to complete the governing set of partial differential equations. These faults are primarily associated with failure to include densities below the initial density of target and microparticle.

A final analysis is made, for all six cases, which traces the rapid dissipation of peak pressure developed in the target.

Shock Wave Formation and Decay

The most noticeable features of the hydrodynamic solutions are the two shock waves which originate from the point of initial contact. Two compressive waves of approximately equal strength appear soon after the start of the calculations. One moves into the target and the other into the projectile. The shock wave into the micrometeoroid is reflected from the vacuum-material boundary as an expansion wave which races to weaken the primary shock wave traveling into the target. This primary wave also decays as the area it affects increases. As the primary front penetrates greater distances into the target, more and more material is compressed which decreases the energy density in the propagating disturbance.

The processes of shock wave formation and subsequent decay are illustrated in the first series of graphs in Figures 9 through 24. To amplify the points of discussion, shock profiles, which are curves of function values versus distance, are presented for several fluid variables along a line near an axis normal to the target. The motion of the fluid is very nearly one dimensional along such a line. On the axis, variables are functions of the radial distance. Results for typical cases are taken from solutions involving several different impact velocities. Each Figure is marked along the distance scale in units of the micrometeoroid radius, R. The measurements start from the point of initial contact, S. In those graphs in which the back edge of the micrometeoroid or back edge of the fluid material is contained, the position is labeled with the letter B.

The radial component of the material velocity is the first parameter shown for Case III in which the micrometeoroid has an impact velocity of 23.69 km/sec. The deceleration of the micrometeoroid and the motion of the target material can be seen in Figures 9 through 11. Values of the radial velocity are given in terms of the impact velocity at six widely separated instants of time.

The appearance of two shock waves is evident in both parts of Figure 9. The shock wave moving into the onrushing projectile stands slightly below the point of initial contact, S. This shock front is almost stationary since its progress is retarded by the fast moving micrometeoroid.

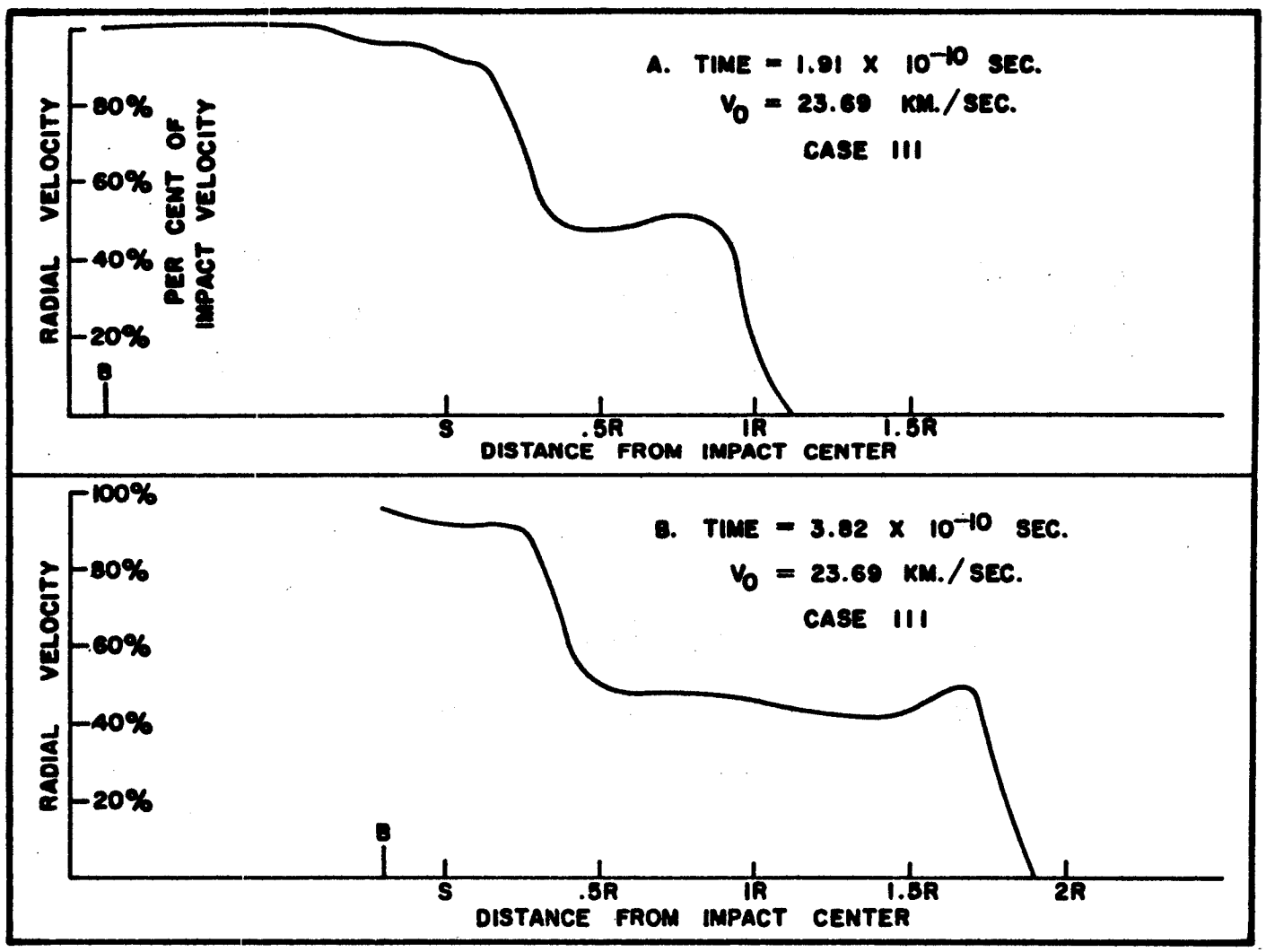

Figure 9. Radial Velocity as a Function of Distance Along Axis, Case III

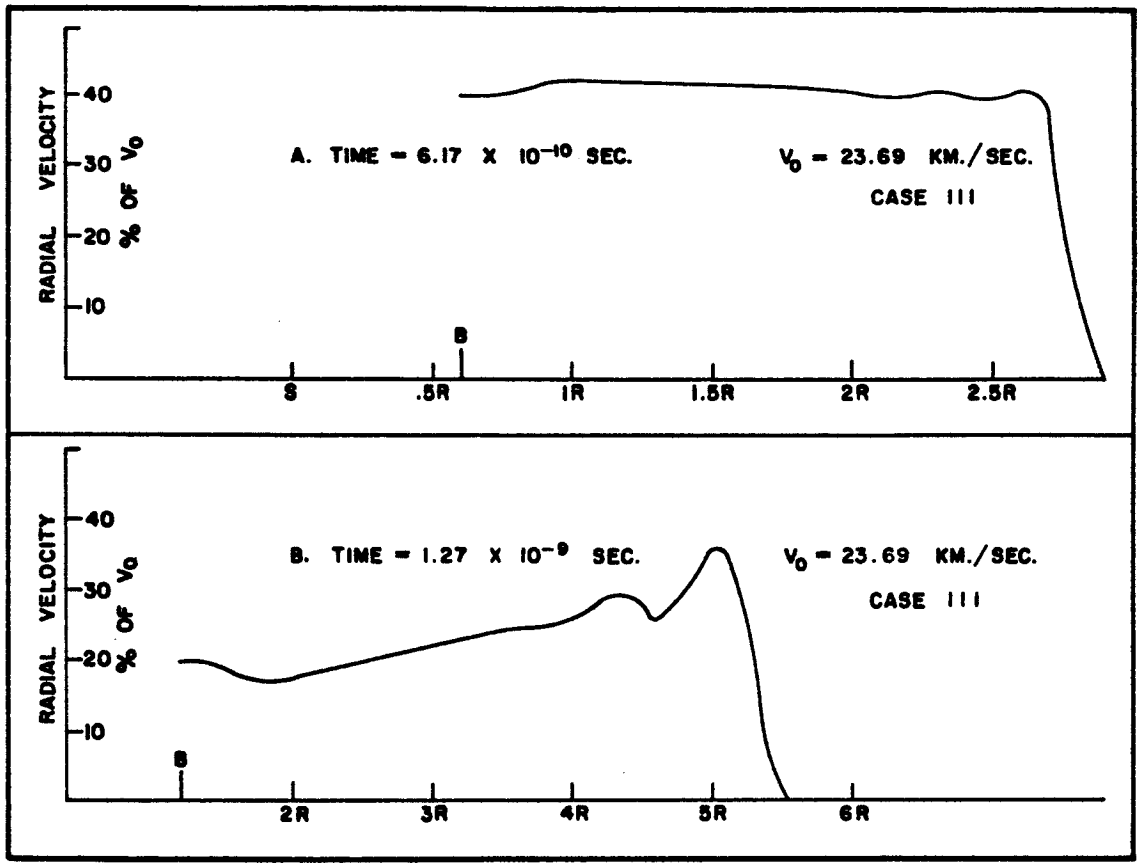

Figure 10. Radial Velocity as a Function of Distance Along Axis, Case III

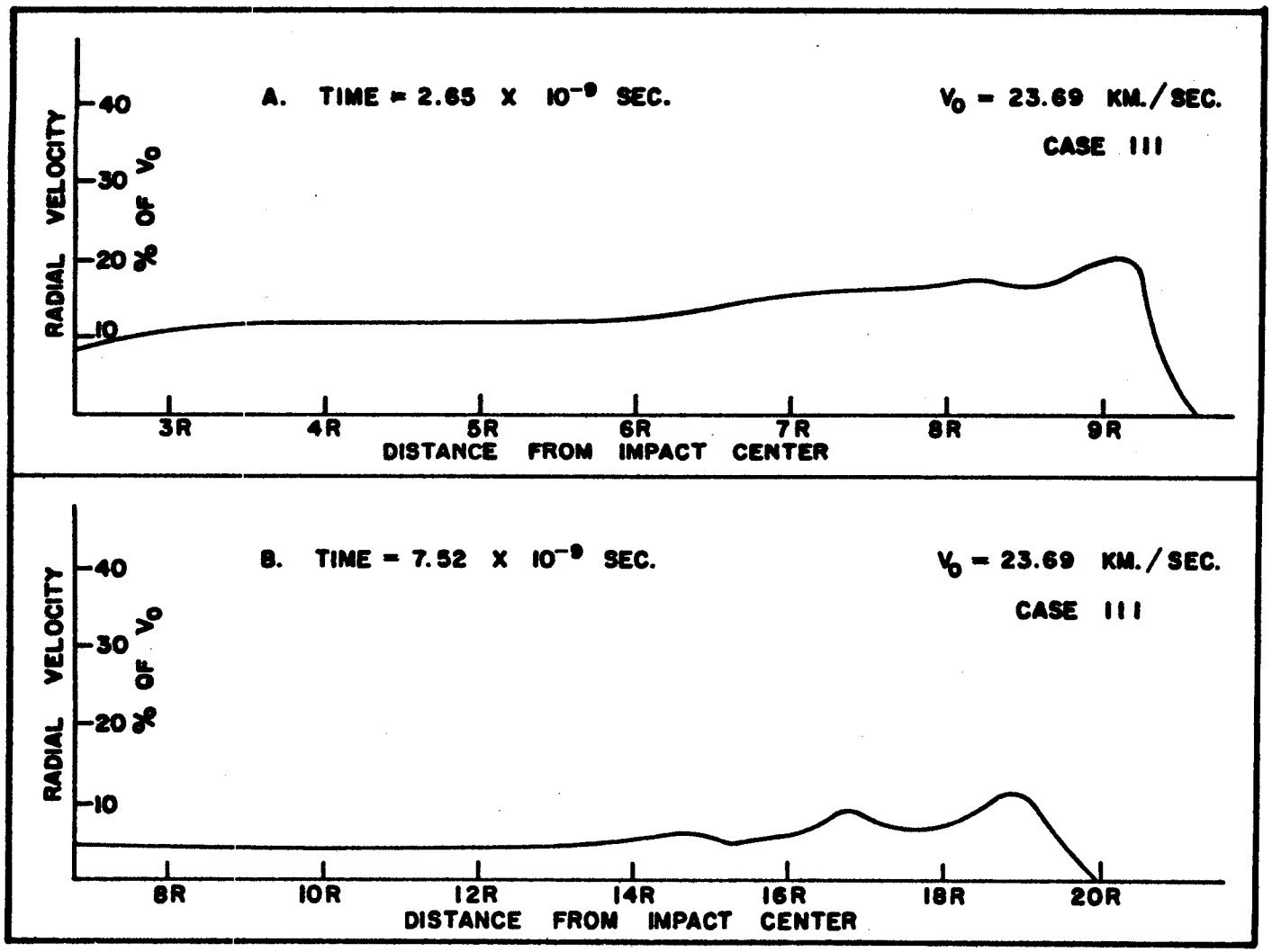

Figure 11. Radial Velocity as a Function of Distance Along Axis, Case III

The primary shock wave propagates rapidly into the target. This material velocity imparted by the primary front slightly exceeds one-half the original free space velocity of the impinging particle, and would increase above one-half as the particle becomes smaller and smaller. A flat plate of aluminum on a semi-infinite slab of aluminum would give exactly one-half the velocity. (23).

In time, the shock wave traveling to the rear of the micrometeoroid reaches the back edge. It is reflected as a rarefaction wave. The modification of the primary shock wave caused by material expansion is shown in Figure 10. If the target and projectile had been of different materials, this first reflection could result in a tension wave proceeding from the free surface. Since the impact process started with aluminum on aluminum, no negative pressures occur.

Further propagation of the shock wave provides an illustration of the decay of the primary shock wave as large amounts of previously undisturbed aluminum are engulfed. Ultimately, this shock front will reduce to a sound wave of vanishingly small amplitude. The hydrodynamic model does not apply to such late stages of the impact and the computer solution must be terminated before material properties such as yield strength play an important role. Late time calculations presenting results still valid under the fluid model are shown in Figure 11. The shock has traveled a great distance, about twenty times the original radius,

but is still able to compress the material sufficiently to give a velocity about ten per cent of the initial impact velocity.

Material Velocity Profiles

Similar results are available for Case VI, which involves the highest incident velocity, 60.64 km/sec. The labeling is similar in Figures 12 through 15 to that used in the previous discussion. The phenomenon noted are again in evidence but occur on a faster time scale. Two shock transitions are apparent in Figures 12 and 13. Free surface reflection and propagation of rarefaction waves lead to decay of the primary shock wave. Development and indication of the geometrical dissipation are shown in Figures 13 through 15. The vertical scale is changed in the last few graphs to allow observation of some detail in the shock wave structure.

Comparison of a few results of Cases III and VI show some points of dissimilarity. The primary shock caused by the more extreme impact, Case VI, is stronger than that resulting in Case III. At a point 20R, the stronger shock can still compress material to a state for which the material velocity is approximately fifteen per cent of the initial value of the impact velocity, 12 km/sec. This compares with the ten per cent value, about 2.5 km/sec., marking Case III at the same distance of shock penetration. The wake, consisting of flowing material long since passed over by the shock front and subject to the continuing action of

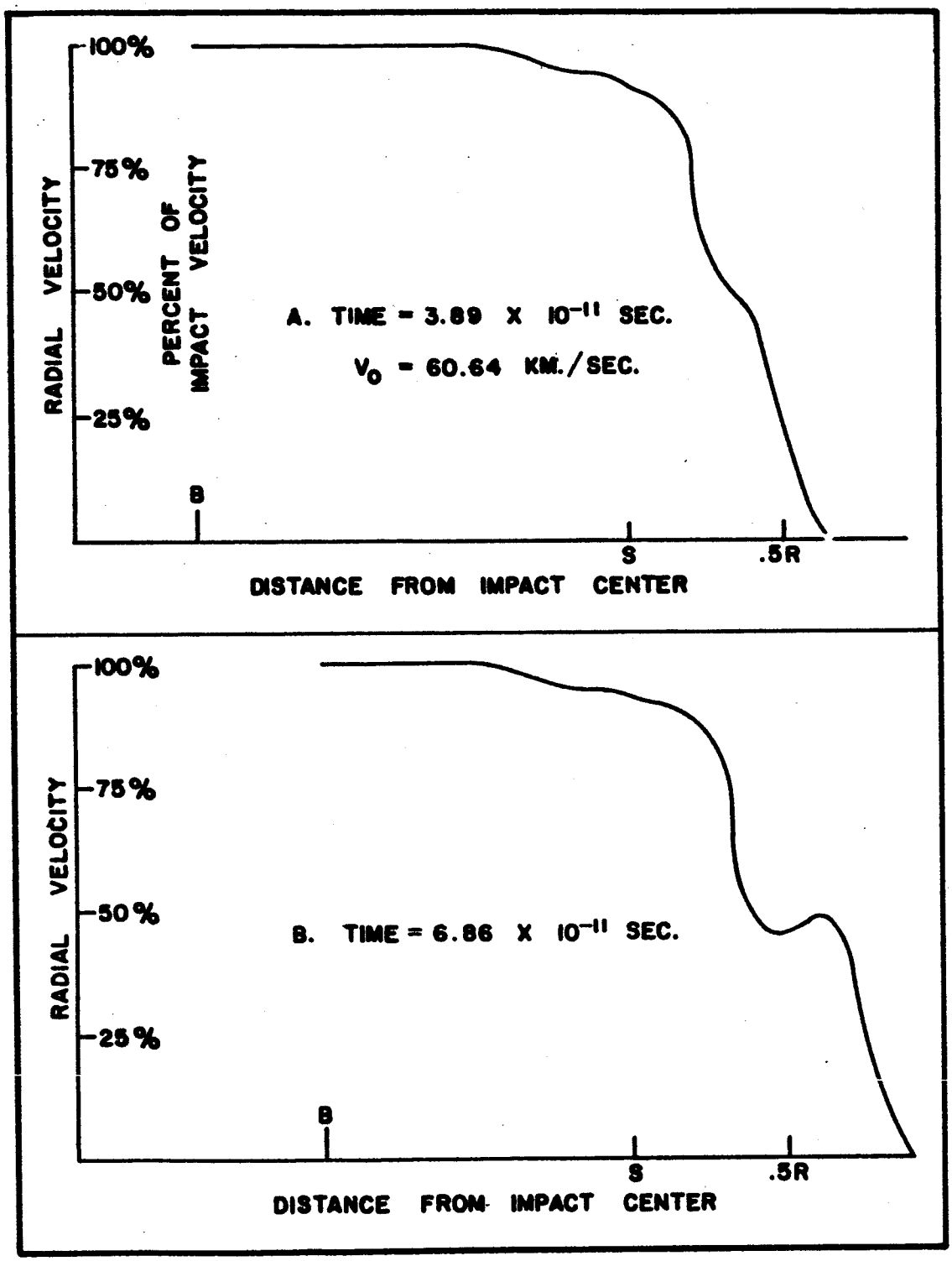

Figure 12. Radial Velocity as a Function of Distance Along Axis, Case VI

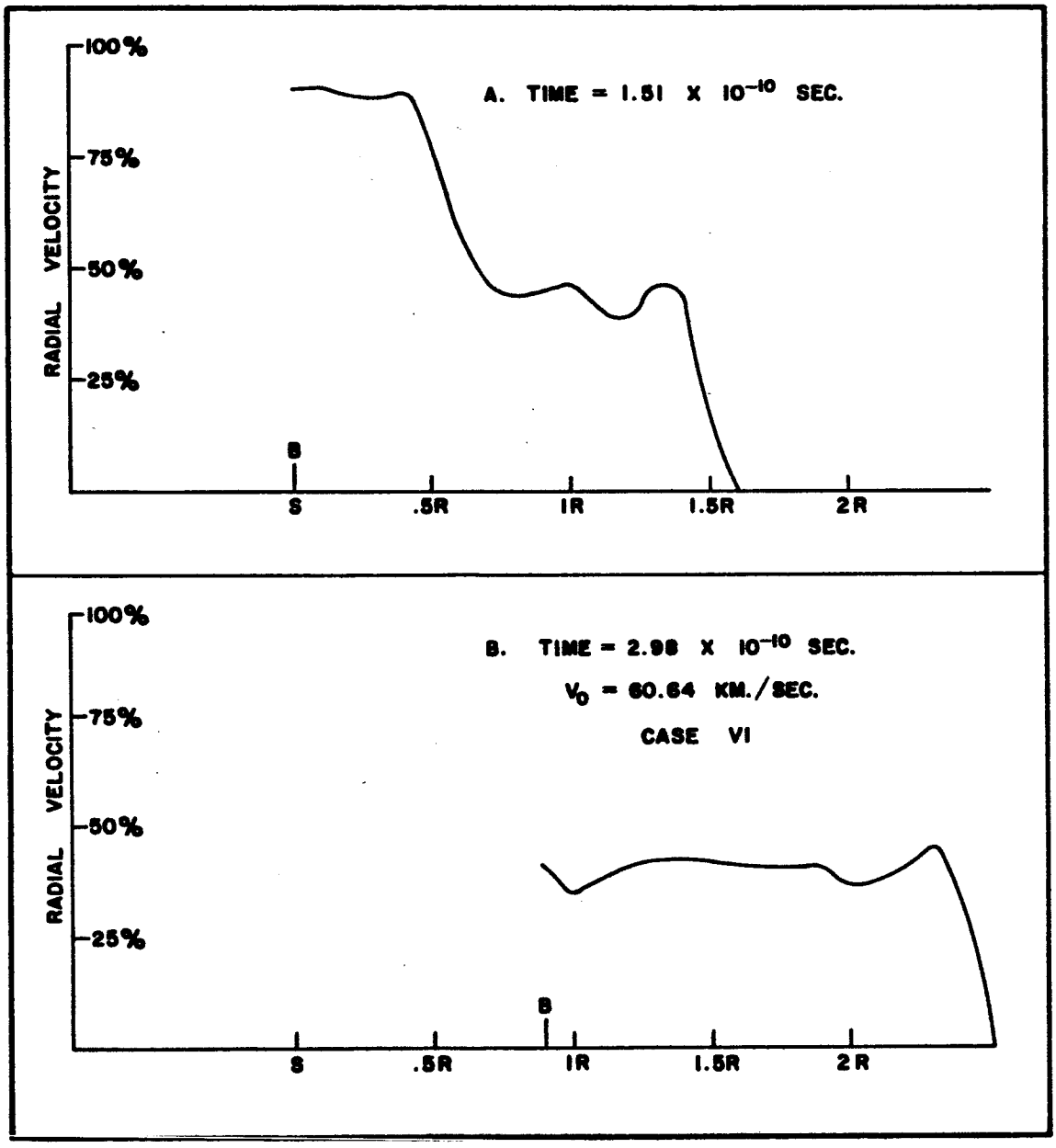

Figure 13. Radial Velocity as a Function of Distance Along Axis, Case VI

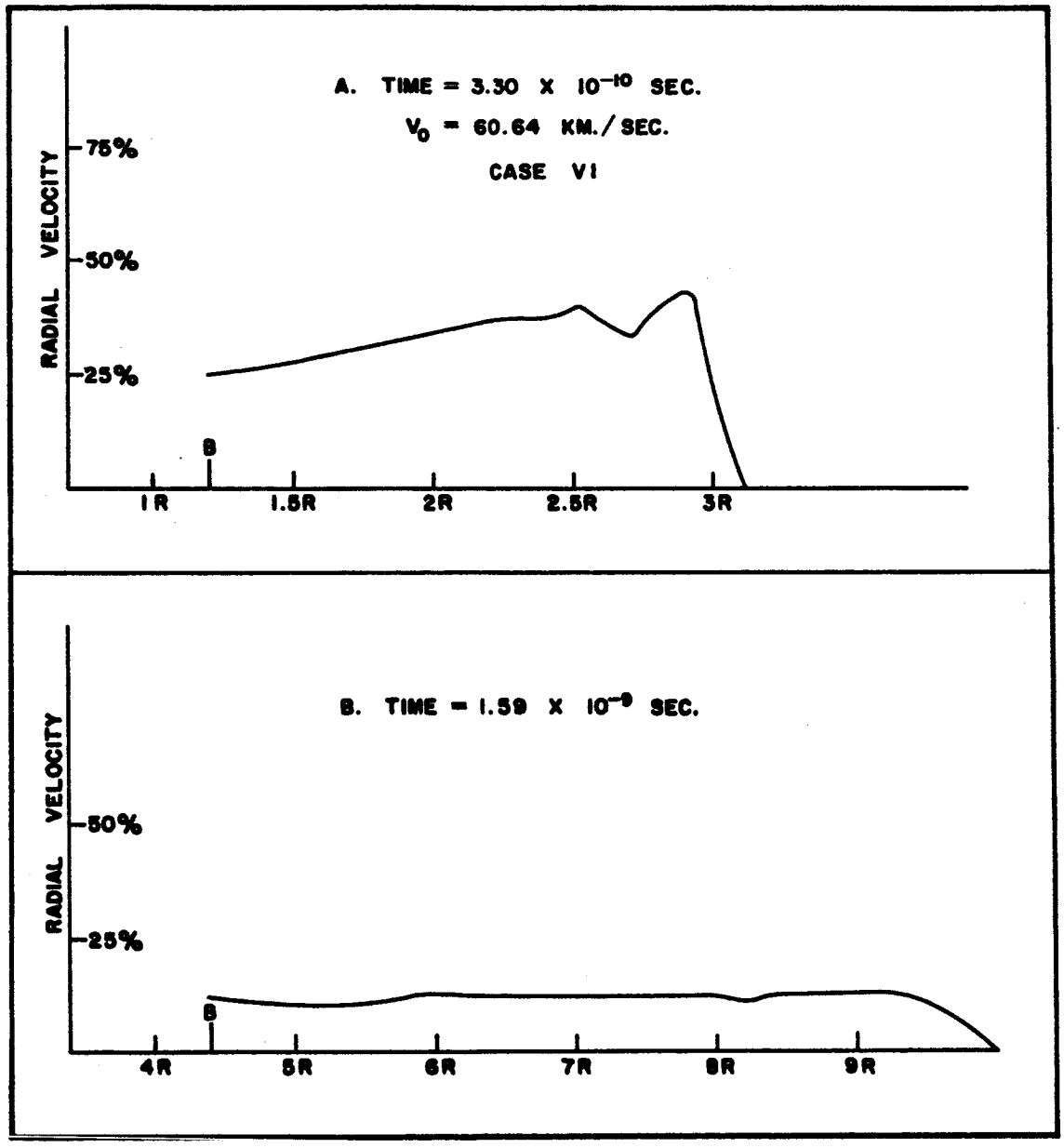

Figure 14. Radial Velocity as a Function of Distance Along Axis, Case VI

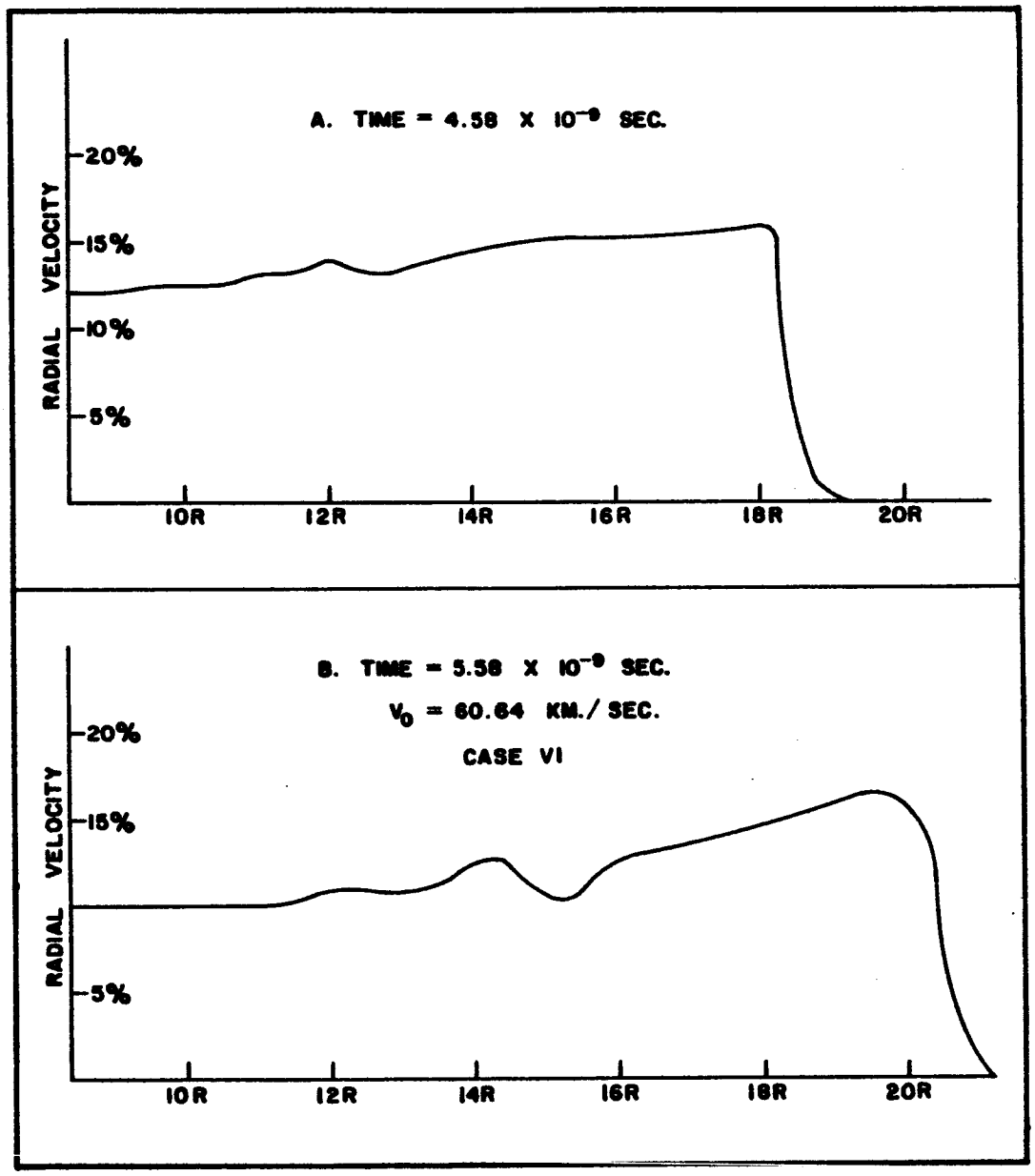

Figure 15. Radial Velocity as a Function of Distance Along Axis, Case VI

rarefaction waves, is also left in a more active state of motion than for the lower velocity impact case. Further illustrations of full two dimensional material velocity vectors depicting the gross motions of target and projectile will be presented and discussed in a later section.

The behavior of the material velocity is unique compared to the other fluid model parameters. At the start of the calculation, all aluminum material is in its normal undisturbed state. The micrometeoroid has initially a very large material velocity which represents the free space velocity of the particle. This leads to the distinctive velocity distributions at initial stages of the impact.

Pressure Profiles

Other fluid parameters, such as pressure or density, illustrate more graphically the growth of the affected volume which occurs after impact. An initial peak, slightly displaced below the point of first contact, indicates the start of shock wave formation. Approximate square wave profiles show the establishment of two shock waves. Reflection and propagation of expansion waves from the vacuum-aluminum boundary, where the pressure is equal to zero, are again seen to contribute to the decay of the primary shock wave.

The next series of curves show the pressure as a function of distance along a line near the 90° axis. The pressure is given in units of megabars. Each megabar is approximately

one million atmospheres. Distance is measured in units R, the radius of the micrometeoroid, from the starting point of fluid interaction, S . This series of curves show sample results for Case III, V_o = 23.69 km/sec, in Figures 16 through 21.

Early stages of pressure development are illustrated in Figure 16. The first results given by the finite difference scheme are for only a few cells of the mesh and must be interpreted as containing oscillations.

Reflection of a strong pressure front from the free surface will begin soon after the time profile shown in Figure 17-A. This release wave combined with declining peak pressures at the head of the distrubance can be followed in Figures 18, 19, and 20. In the pressure curves, there seems to be a spurious peak at the front of the shock wave; that is higher pressures than would be expected. This is due in part to the effect of the pseudo viscosity in the numerical calculation. The value of the coefficients in the expression for the pseudo viscosity were kept at very small values, with greater smoothing effects on the flow profiles being obtained from the structure of the finite difference equations. This was done to avoid losses in moving the particle through the cells of the finite difference mesh. The reduction in value of the pseudo viscosity results in larger oscillations in the variables, particularly the pressure and the specific internal energy, than in previous hydrodynamic calculations. (4,14).

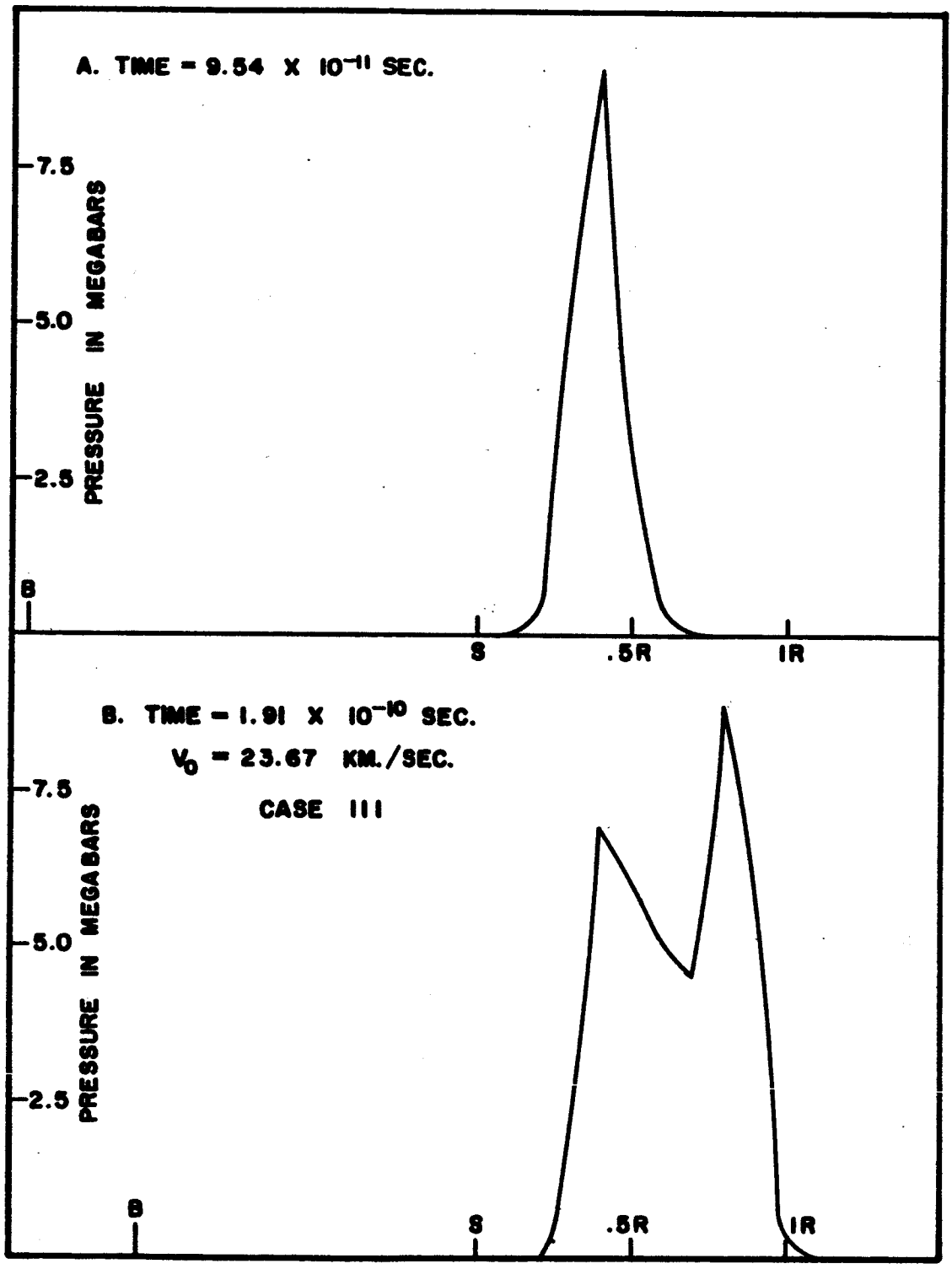

Figure 16. Pressure Profiles Along Normal Axis, Case III

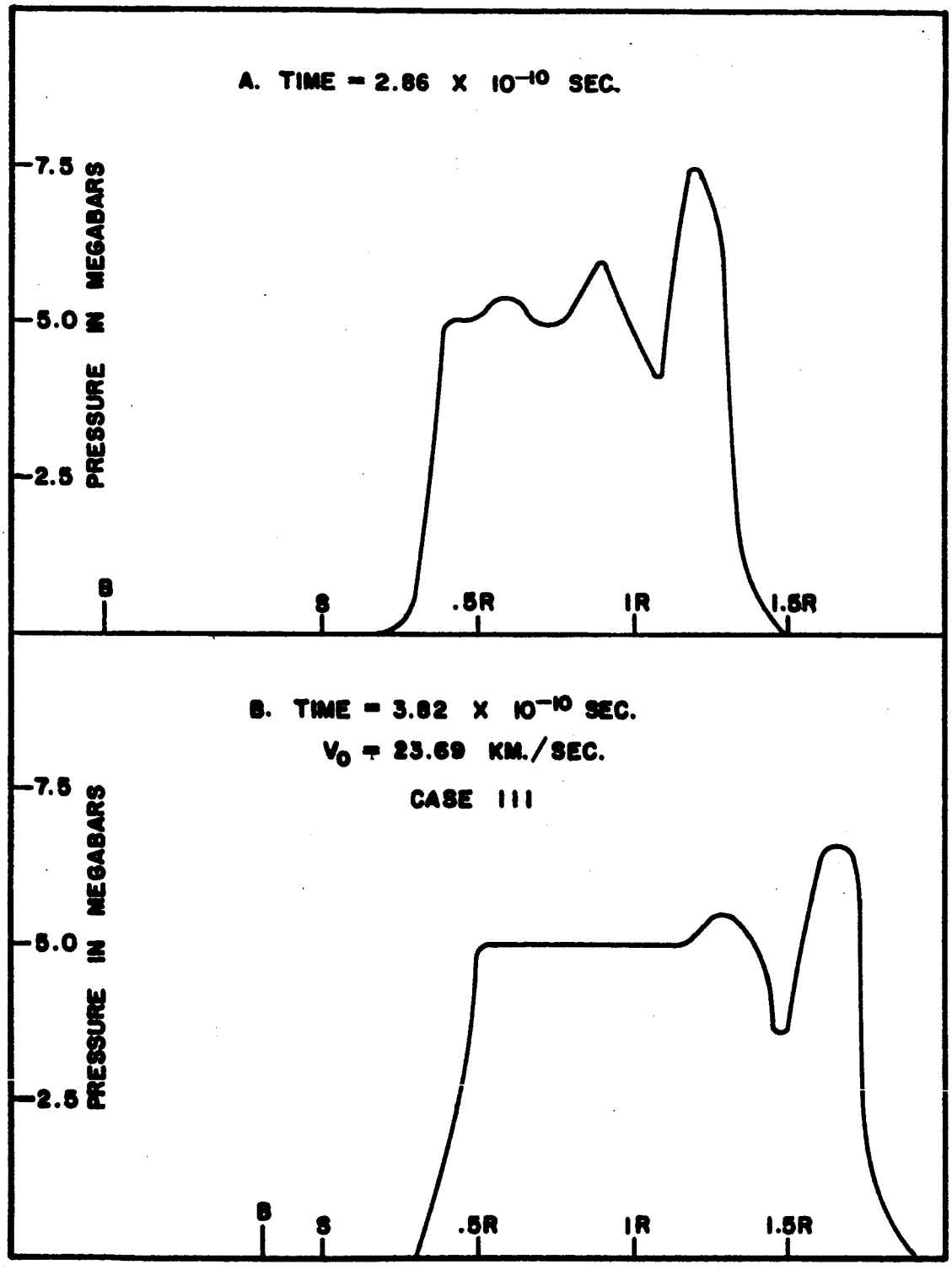

Figure 17. Pressure Profiles Along Normal Axis, Case III

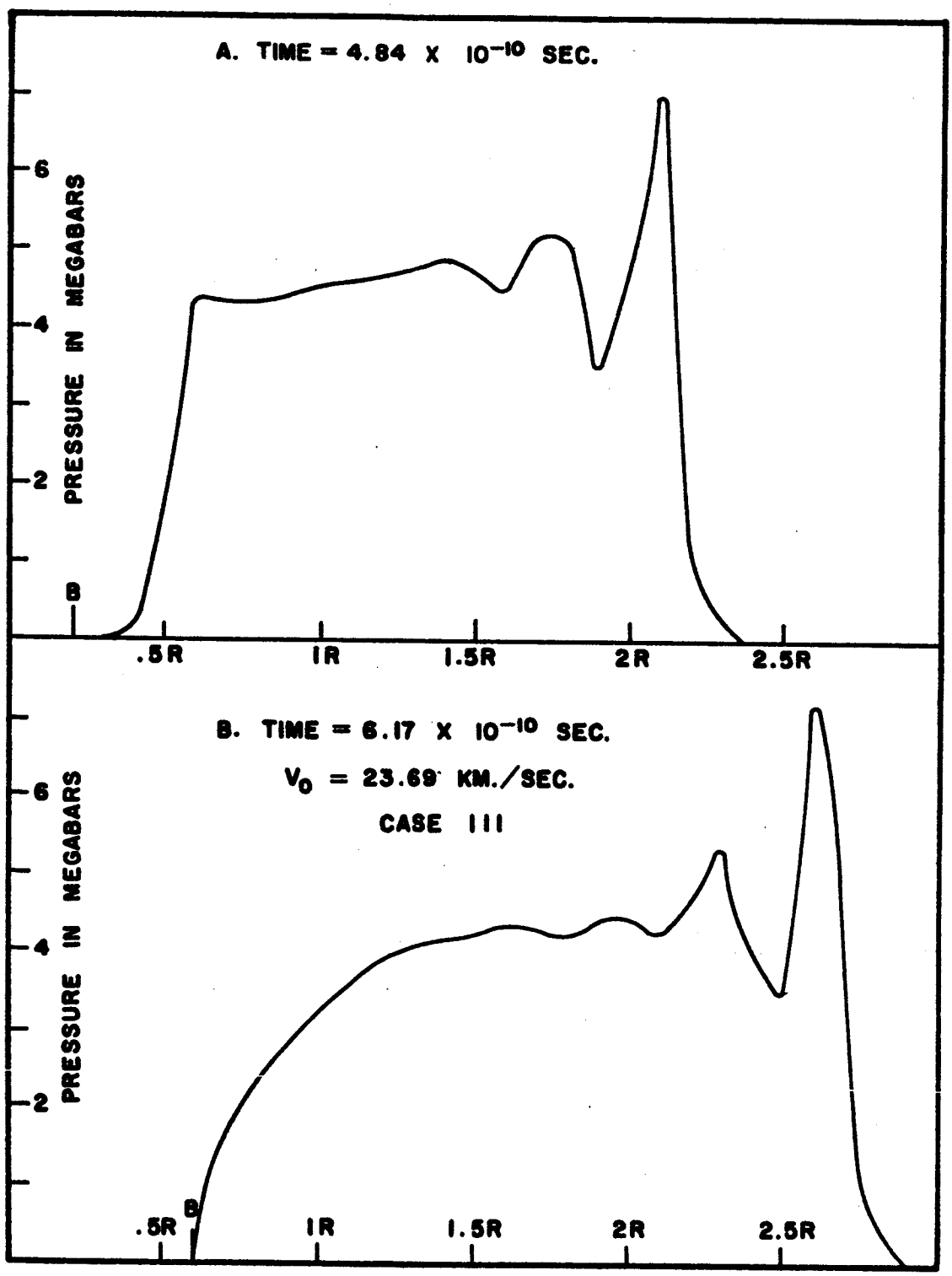

Figure 18. Pressure Profiles Along Normal Axis, Case III

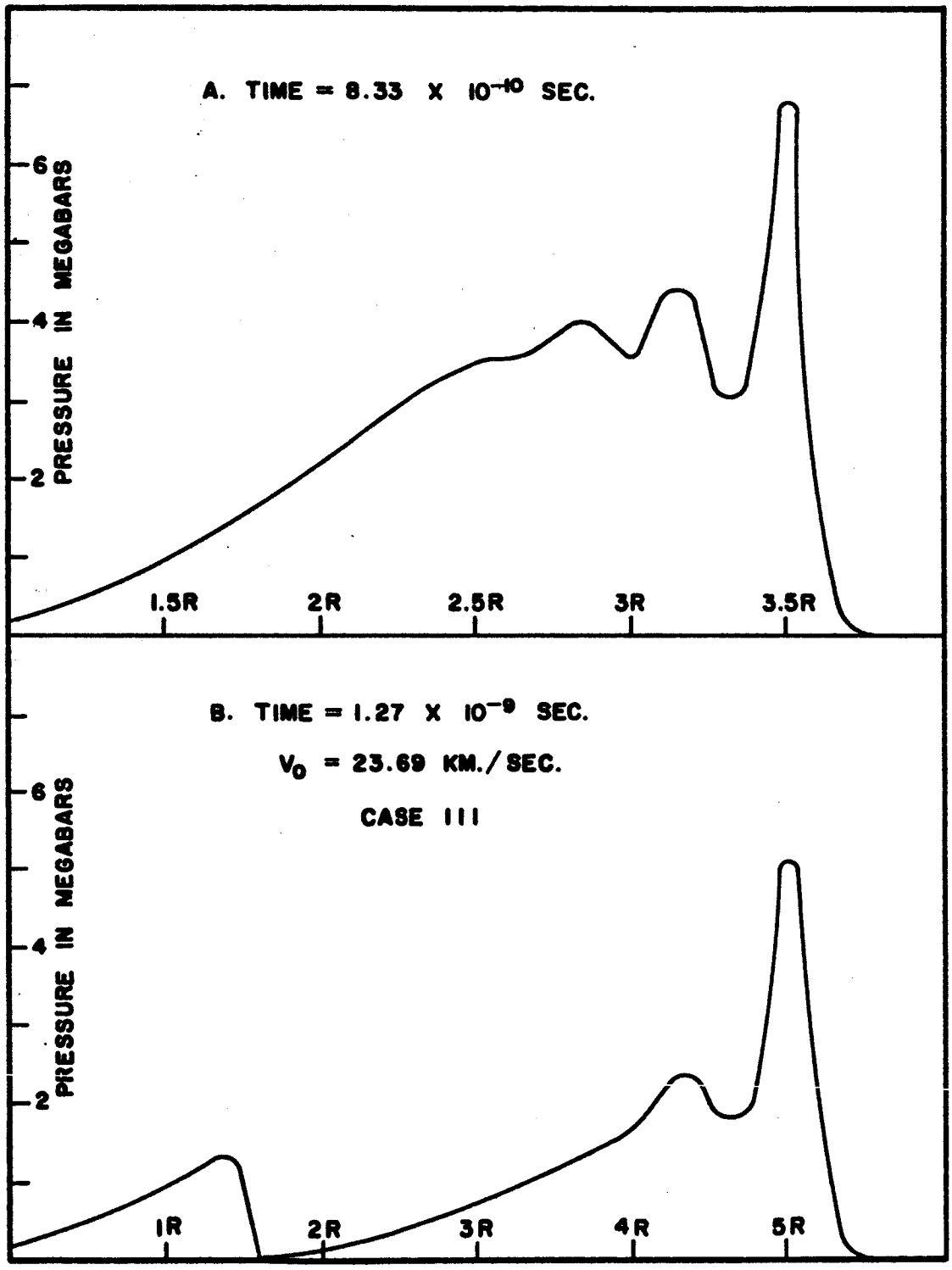

Figure 19. Pressure Profiles Along Normal Axis, Case III

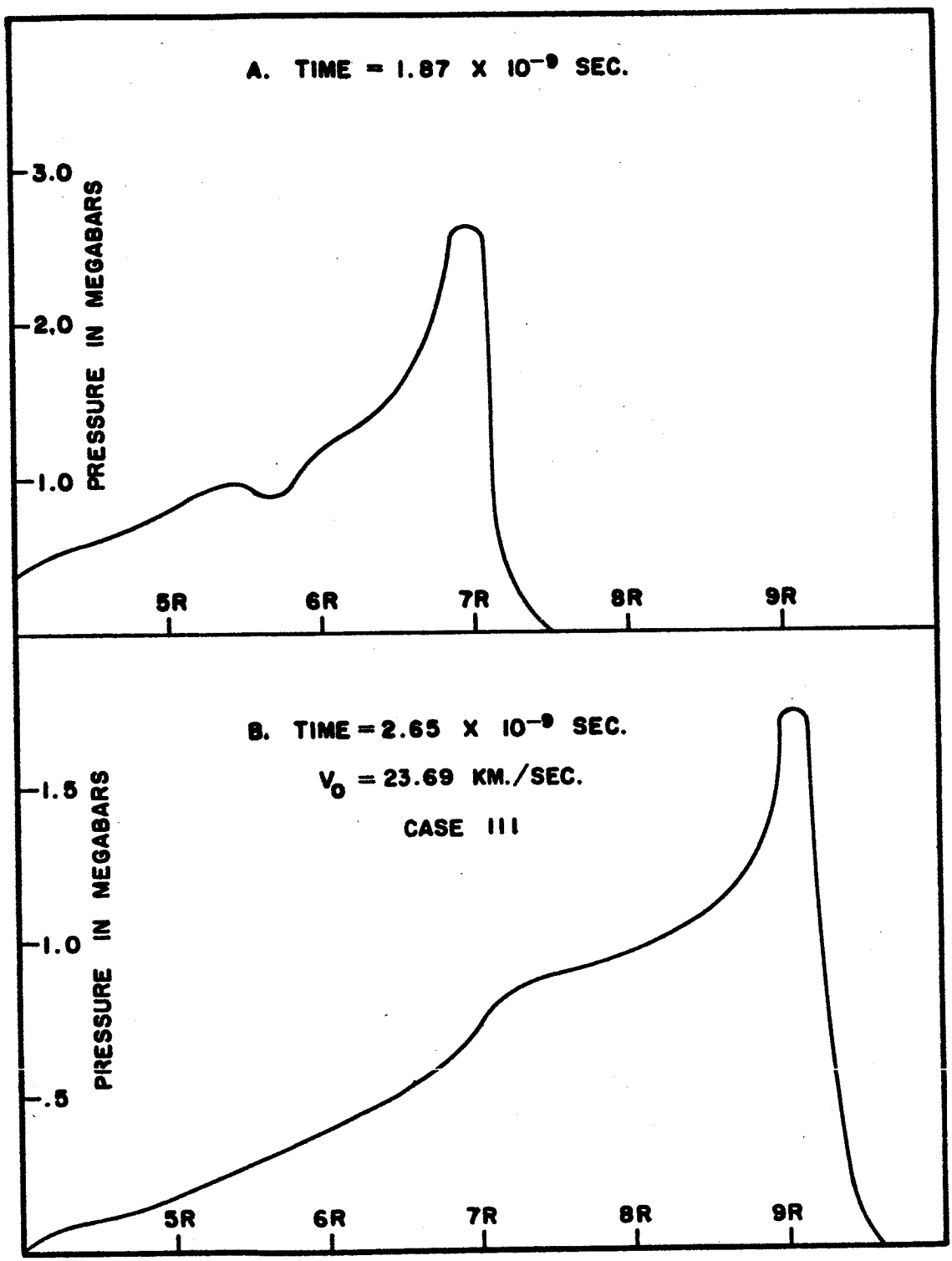

Figure 20. Pressure Profiles Along Normal Axis, Case III

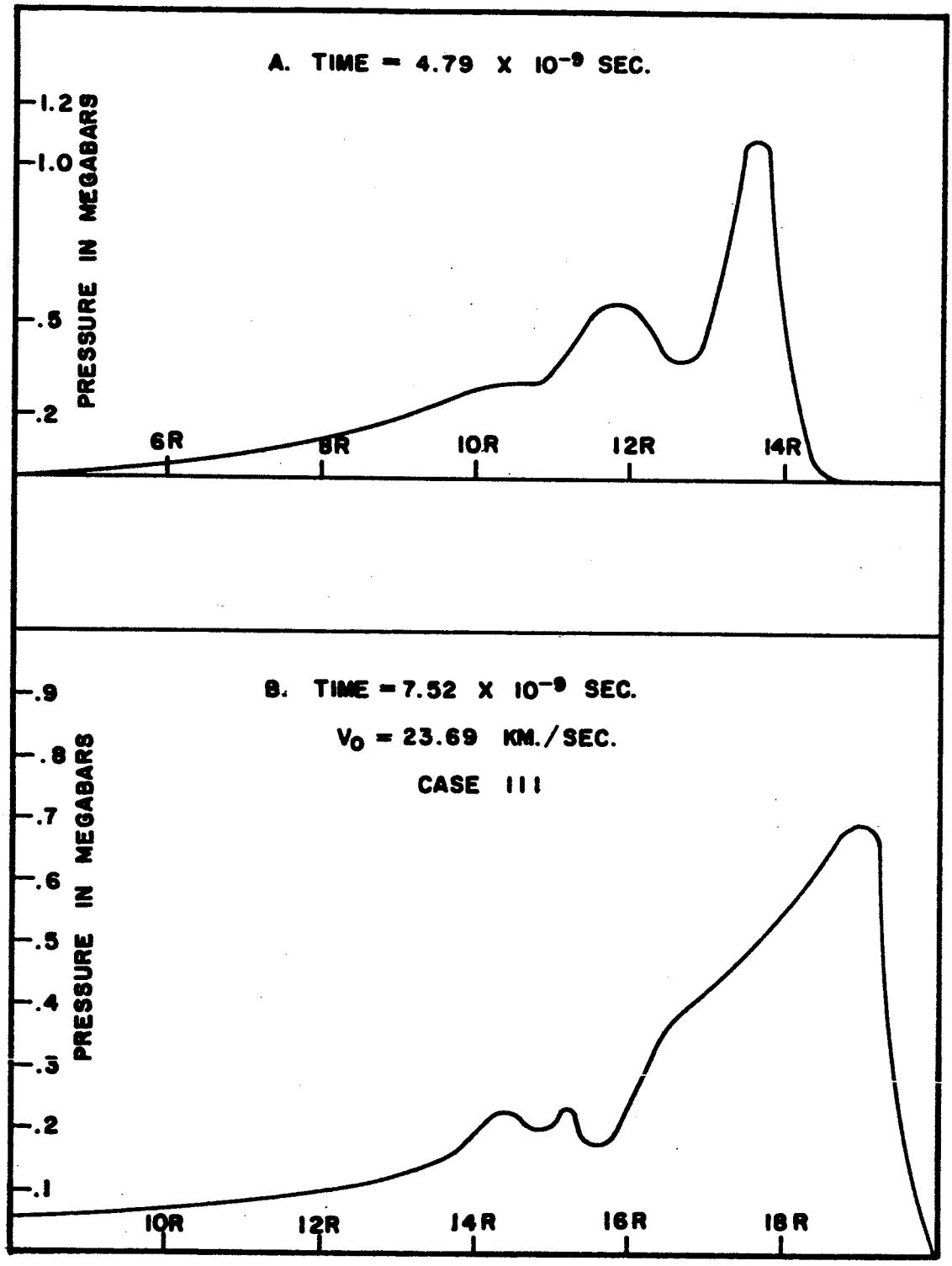

Figure 21. Pressure Profiles Along Normal Axis, Case III

Profiles, such as those in Figure 19, can also be affected by irregularities along lines of the finite difference mesh away from the normal axis. The change in scale of the plots of the pressure in Figures 19, 20, and 21 reflect the drastic decay as the compressive power of the shock front grows weaker.

Density Profiles

The density behavior of the fluid model is quite closely related to the pressure of the fluid. Complete specification of the fluid state requires the internal energy, the pressure and the density. There is a unique relationship between the density and pressure only at shock points, that is peak value points, of the difference net. The state of the material away from a shock front is found on an expansion adiabat determined by the peak pressure to which the material has been subjected. Results taken from full field contour maps are given for the density in Figures 22 through 24. The initial impact velocity was 5.68 km/sec. This was the lowest velocity considered and is called Case I. This velocity is only slightly higher than the velocity of sound in aluminum, 5.63 km/sec. There is some doubt concerning the validity of the hydrodynamic model at such a low velocity, but experimental results agree with the values obtained in the numerical solutions (23). Pressures on the order of several hundreds of kilobars are not carried to

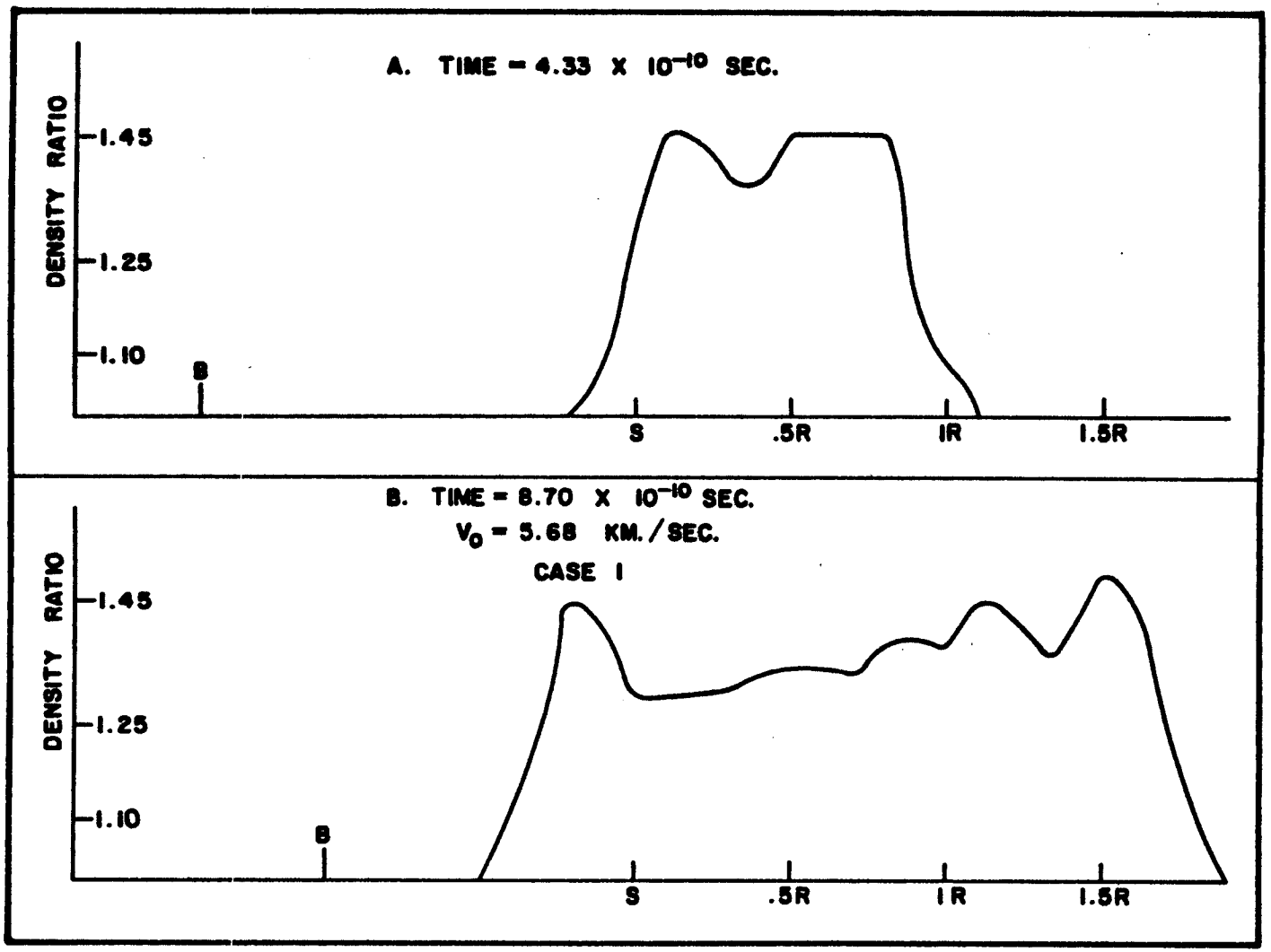

Figure 22. Density Profiles Along Normal Axis, Case I

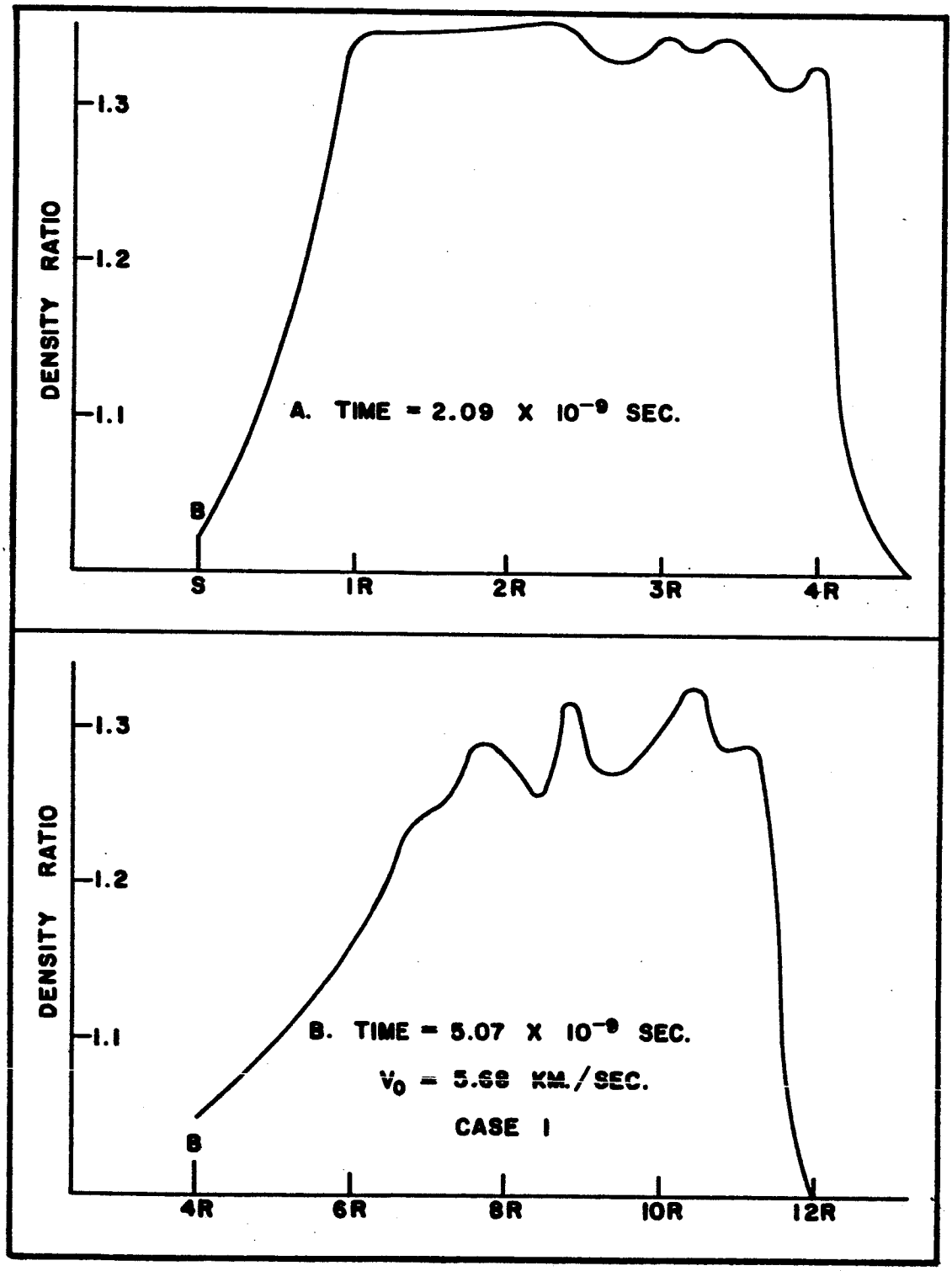

Figure 23. Density Profiles Along Normal Axis, Case I

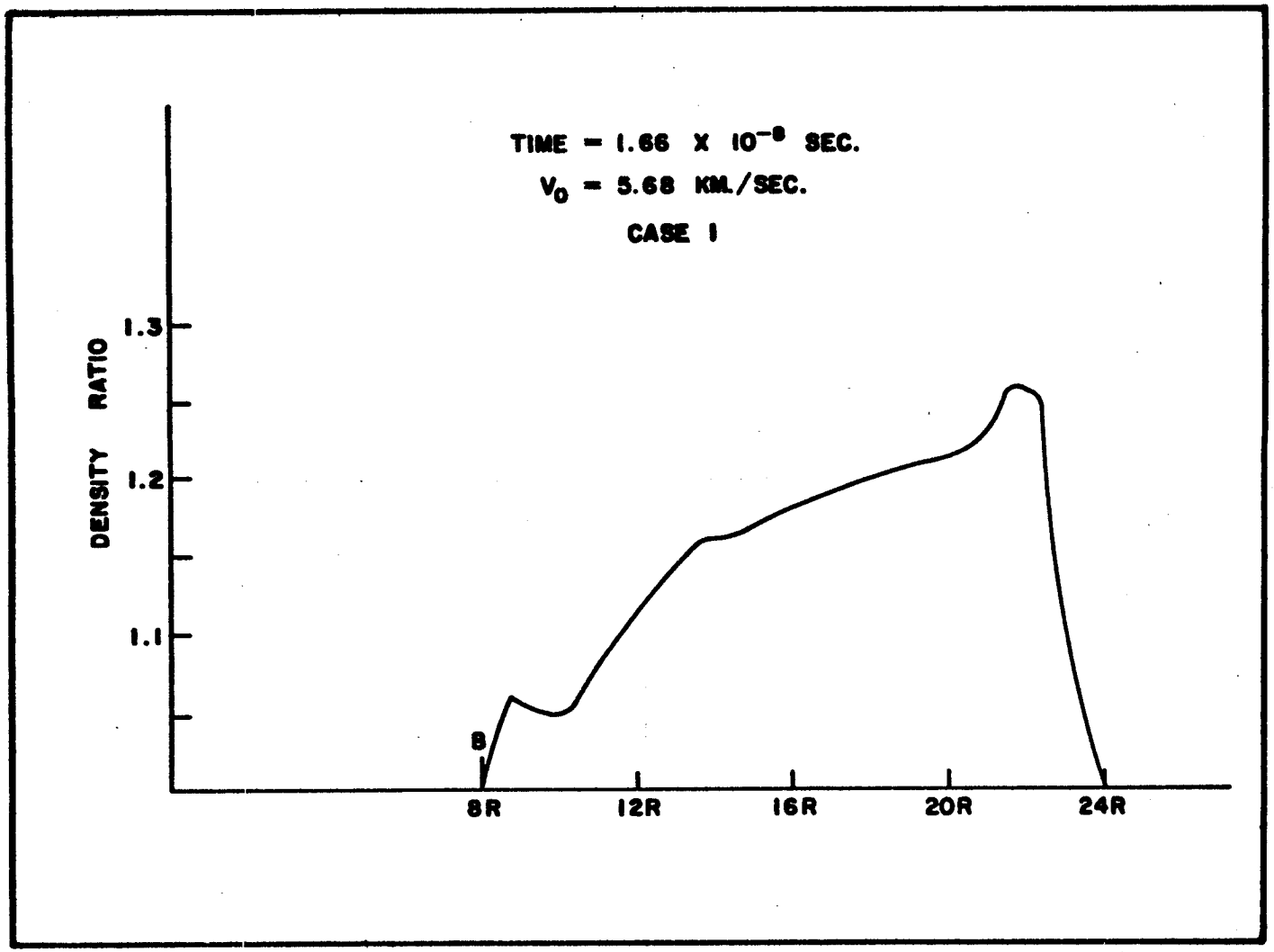

Figure 24. Density Profiles Along Normal Axis, Case I

to times when pressures differ significantly from hydrodynamic pressures.

The density is drawn as a function of radial distance on a line near the axis of symmetry. The density value is given as the ratio of material density at a point to that of normal aluminum. This low velocity case offers one new feature in the description of hypervelocity impact. The two shock waves are able to propagate further in both directions when the micrometeoroid is half way into the target. The projectile moves somewhat more slowly into the target than in the other cases considered. This can be interpreted as a greater transfer of energy from micrometeoroid to target. A relatively stronger and broader primary shock front propagates into the target. The somewhat slower decay is also evident in results showing surface motion during the initial stages of fluid distortion.

Events take place on a longer time scale for Case I. This is in accordance with the much slower impact velocity. The results of all Figures are for times reduced from the non-dimensional times for a 10^{-9} gram micrometeoroid of radius $R = 4.41 \times 10^{-4}$cm.

The establishment of two shock waves as viewed through profiles of the material density is illustrated in Figures 22 and 23. A typical one dimension shock profile is seen in Figure 24 which is for a time after reflection from the free surface has taken place.

Full two dimension results of the hydrodynamic model are shown for one case, Case V, in the next section.

Two Dimensional Distributions

The hypervelocity impact of a micrometeoroid on a semi-infinite target puts the material of the target in motion and produces a large scale disturbance of the flowing aluminum. A series of two dimensional maps showing the fluid pressure and material velocity distribution drawn from the numerical solutions of the hydrodynamic model are presented in this section. These curves were drawn for Case V, in which a micrometeoroid impacts at a velocity of 47.38 km/sec.

A qualitative survey of the features associated with hypervelocity impact has been given by Charters (8). This description will be discussed now since the present solution embodies a number of observed effects.

The impact is accompanied by a flash of light. Radiation can be observed form the immediate vicinity of the impact. This is not shown by the hydrodynamic equations since they contain no radiation producing mechanism. If the governing equations were supplemented by a more realistic equation of state which includes ionization and radiation energy, and changes in the conservation equations, it is believed that the plasma state formed by the impact would give radiation.

The shock waves discussed are observed in high speed

experiments. One, referred to as the primary shock wave, radiates out form the point of impact, compressing and accelerating the material of the target ahead of the on-rushing sphere. Another wave moves back into the projectile opposite to the notion of the projectile. The result of these two movements is an approximately stationary shock front moving very slowly beyond the point of initial contact.

As the back edge of the micrometeoroid passes the position of the original target, a depression or crater starts to form. Most of the flow is in a radial direction, but some material moves around the crater edge and is ejected. These features seen in the laboratory are also evident in the numerical solution. The opening of a cavity and the movement of target material above the original target surface are both very striking in the solutions presented. This escape of material occurs in all six velocity cases calculated.

The shock wave which is reflected from the free surface as a rarefaction wave eventually overtakes the primary shock wave. This latter wave penetrates great distances into the target. The expanding crater follows at a distance. Between the two, a shell of highly energetic matter, compressed by the shock and stretched by the rarefaction, is found. The strength of the shock wave decreases as its volume of action increases, and as it is overtaken by rare-faction waves originating at the free surface of the material. These features of hypervelocity impact are

displayed in the hydrodynamic solutions.

Ultimately, the plastic and elastic properties of the target material void the perfect fluid assumptions and the final size and shape of the crater cannot be fixed. This difficulty can be remedied by consideration of an equation of state describing aluminum and by investigation of the transition from fluid to elastic flow.

Individual matched distributions of the pressure and material velocity are given for different instants of time for Case V. The material velocity is portrayed by scaled vectors representing the velocity of material at the tail of the vector. Pressure contour maps are obtained by connecting points of equal pressure on different radial lines. Distances are indicated on the normal axis in units of the micrometeoroid radius, R. The times shown are for the typical 10^{-9} gm micrometeoroid. Results for these two variables are presented in Figures 25 through 44.

Pressure and Material Velocity Distributions

The micrometeoroid enters the target quite rapidly. An early time velocity distribution is shown in Figure 25. Most of the velocity vectors are parallel to the normal axis and represent the free velocity of the micrometeoroid. The vectors near the roiginal surface line and below this line are reduced in magnitude and oscillate about this direction.

The pressure distribution in Figure 26 shows the highest pressure attained in this particular impact case. Two

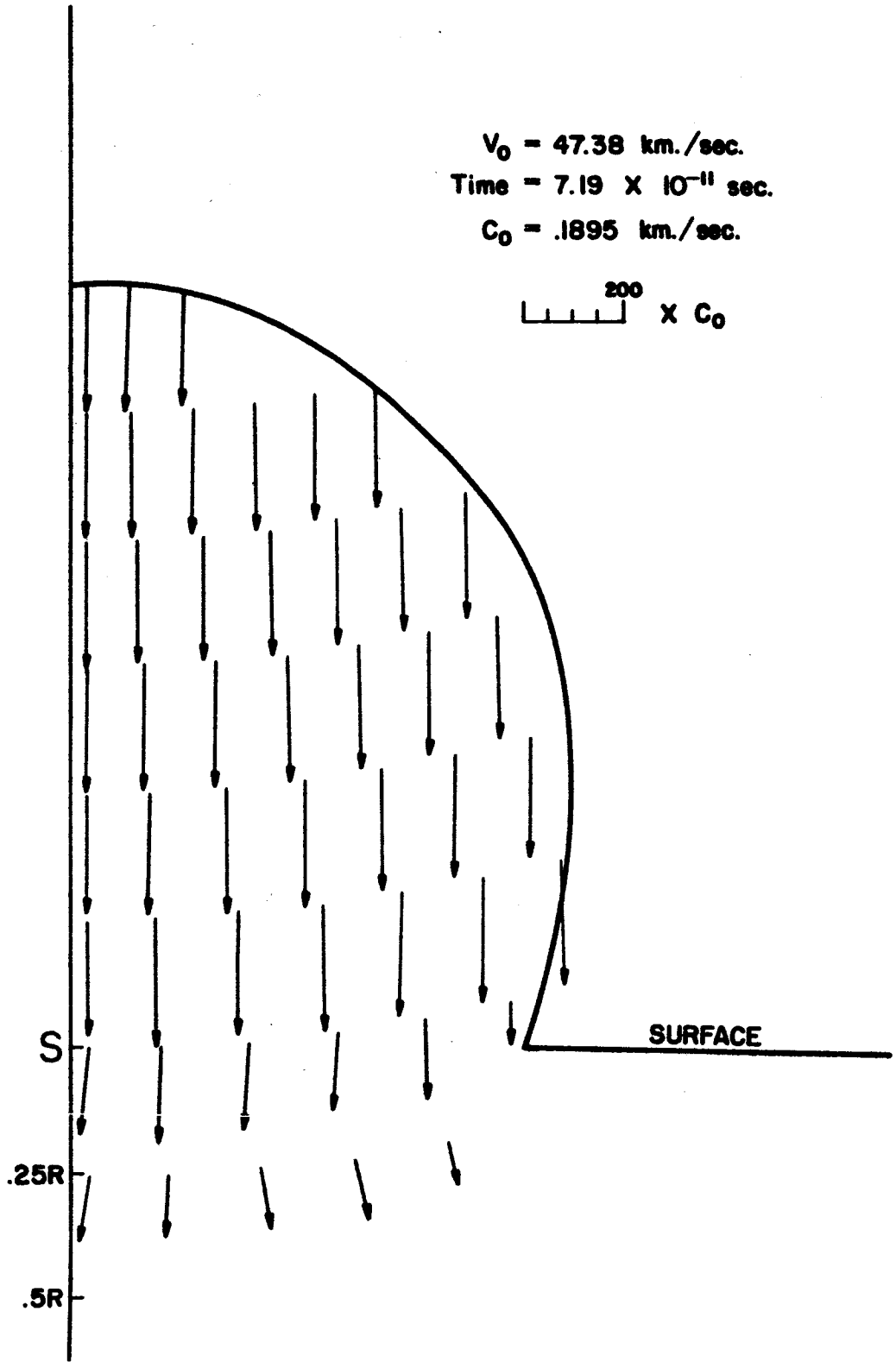

Figure 25. Velocity Distribution, Case V (Time = 7.19×10^{-11} seconds)

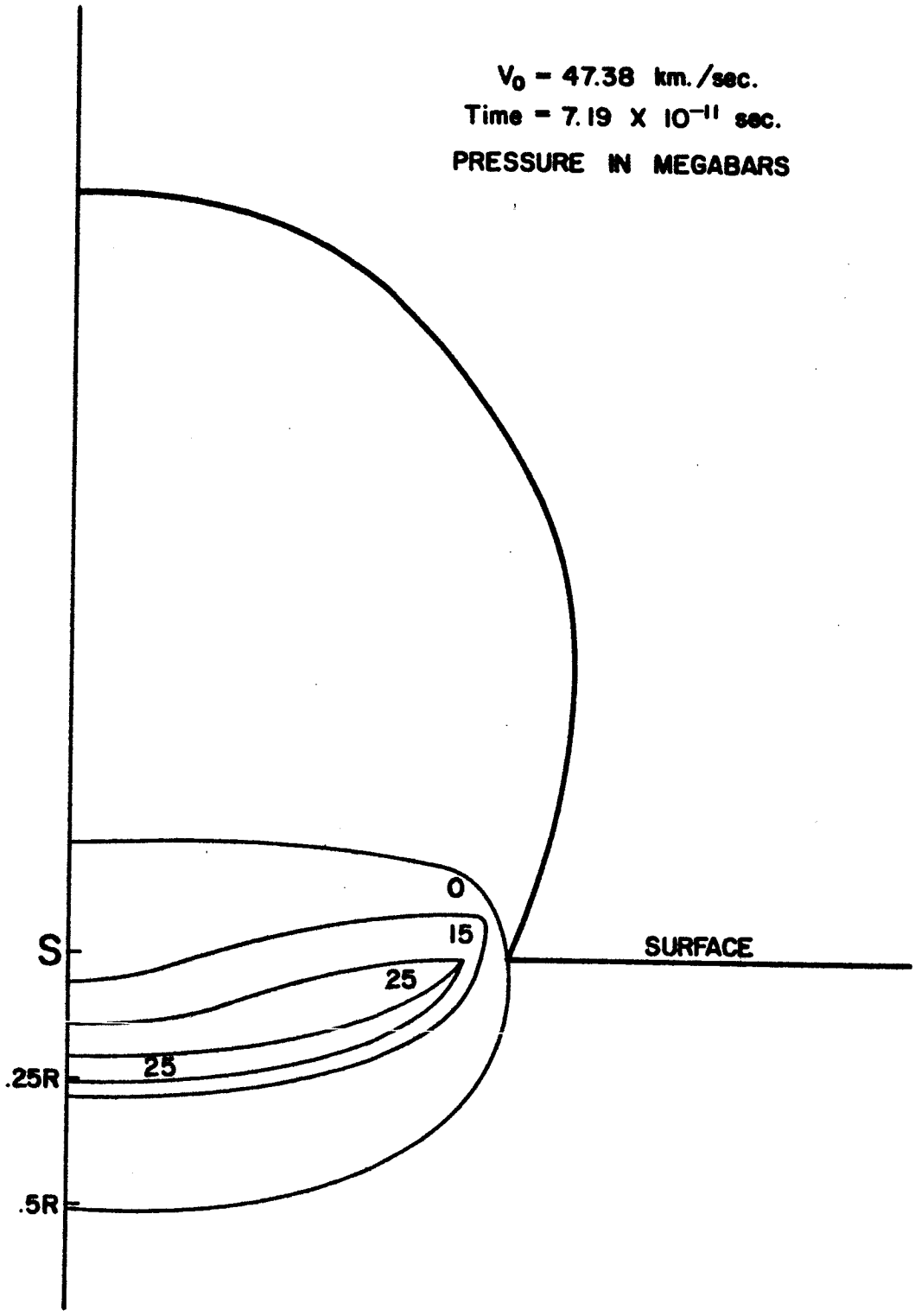

Figure 26. Pressure Contours, Case V (Time = 7.19×10^{-11} seconds)

approximately equal shocks will be formed from the pressure peak shown. There is some assymetry apparent in Figure 26 and subsequent plots due to the geometry of the entering projectile and the initial division of material velocity. The material of the micrometeoroid has initially high velocity while the material of the target is undisturbed. Some general undulations are seen in the contour maps and may also be discerned by careful inspection of the velocity distributions. This is caused by the particular choice of times and points included in the results and by the nature of numerical solutions.

At a time when about one-half of the micrometeoroid has penetrated the semi-infinite target, the primary shock wave covers an area on the curve (volume in the micrometeoroid) slightly less than one-half of the micrometeoroid area (volume). This quantitative extent of the primary shock wave at the mid-penetration point, has been found to vary with the velocity.

The velocity distribution in Figure 27 illustrates the start of the expansion period of the disturbance. Material moving from the straight line path of the onrushing micrometeoroid has been put in motion by the primary shock wave rather than by direct contact with the projectile. The maximum pressure developed, in Case V, is twenty-five megabars. The extent of this peak pressure is shown in Figure 28. In an idealized treatment of this impact, the peak pressure would extend to the surface. In the numerical

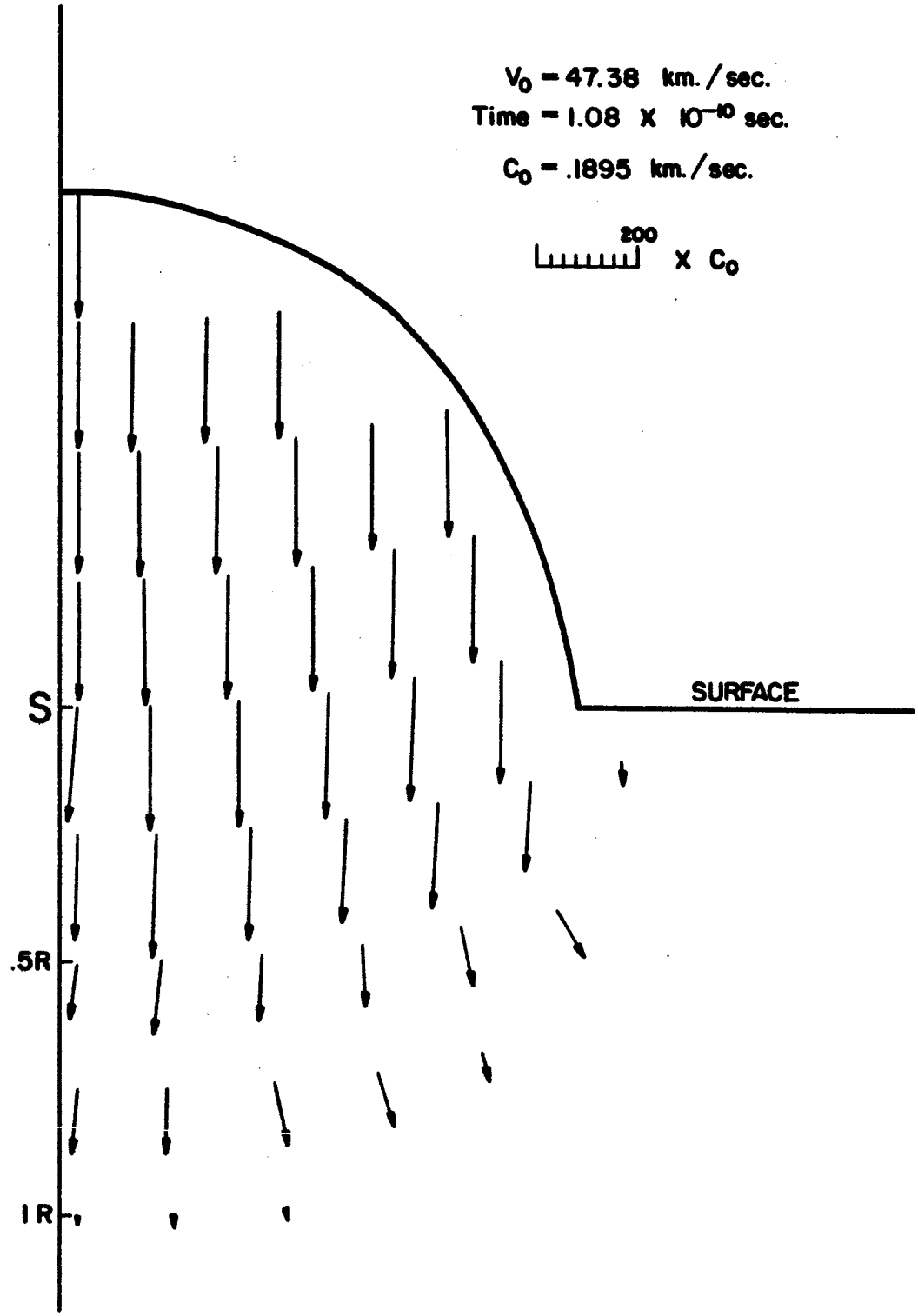

Figure 27. Velocity Distribution, Case V (Time = 1.08×10^{-10} seconds)

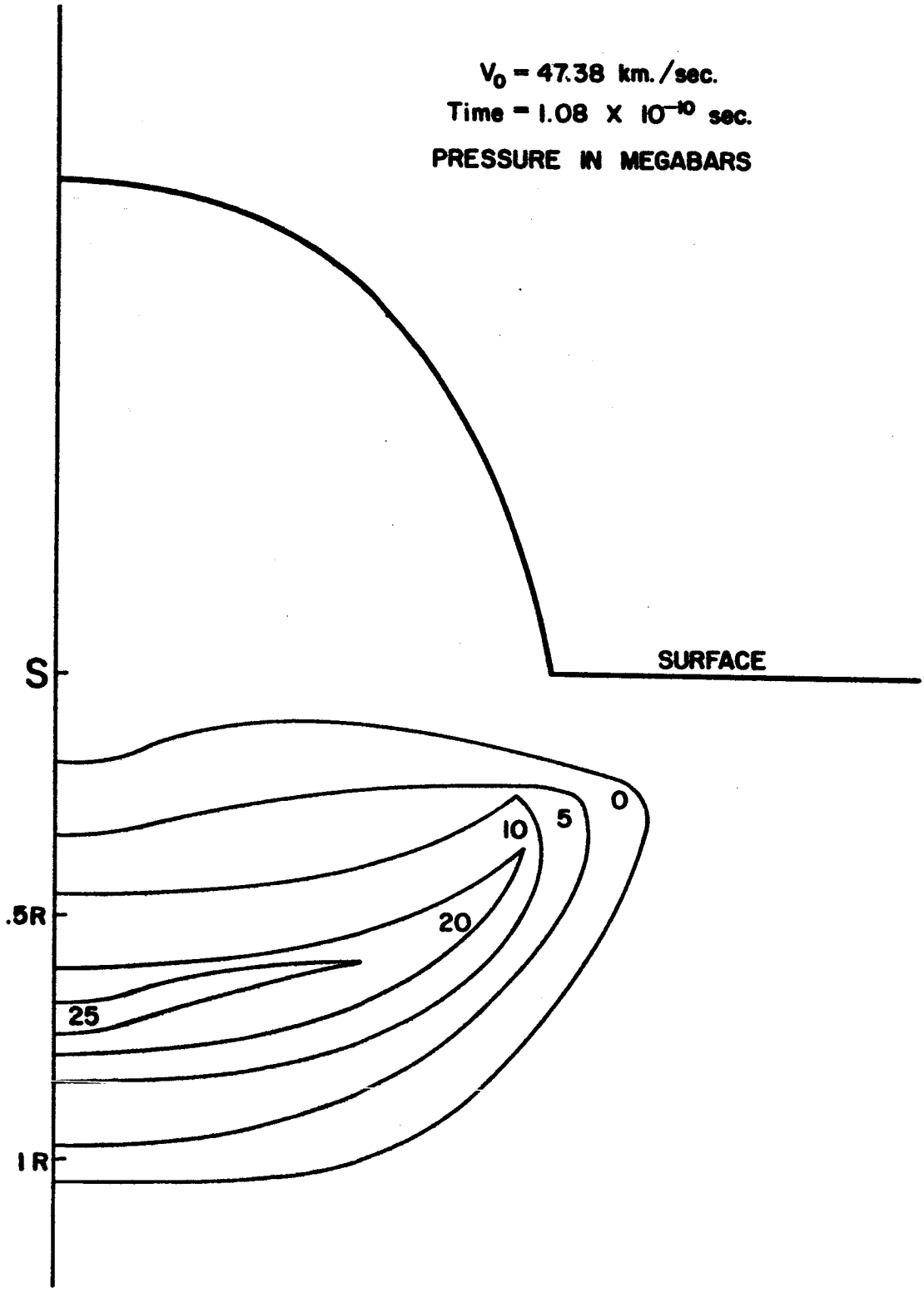

Figure 28. Pressure Contours, Case V (Time = 1.08×10^{-10} seconds)

calculations, however, the motion of fluid particles, is communicated from cell to cell in the mesh covering the region of interest. The model chosen probably depicts the physical situation rather well; the peak pressure occurs near the normal axis under the maxium thrust developed by the impinging sphere.

At slightly later times, the radial character of the fluid disturbance can be seen. The material of the target has a strong tendency to expand away from the regions of direct impact with a material velocity of magnitude approximately one-half the free space velocity of the micrometeoroid. The shape of the disturbed portion of the target material, and the micrometeoroid, can be seen from the pressure distribution in Figure 30. It is near this time that free surface effects begin to influence the solution. The indicated irregularity, in Figure 29 and 30, near the joining of projectile and target is attributed to reflection between the free surface and expanding shock waves.

By compressing the material of the target, the incident particle moves into the target. This continuing action eventually causes a depression in the original target surface. The shape of the crater, as seen in Figure 31, is primarily a result of the geometry of the impinging particle and the effects of the rearward moving shock front. Velocity vectors corresponding to V_o, the initial impact velocity, are seen near the point S. This indicates that some of the original micrometeoroid still retains its

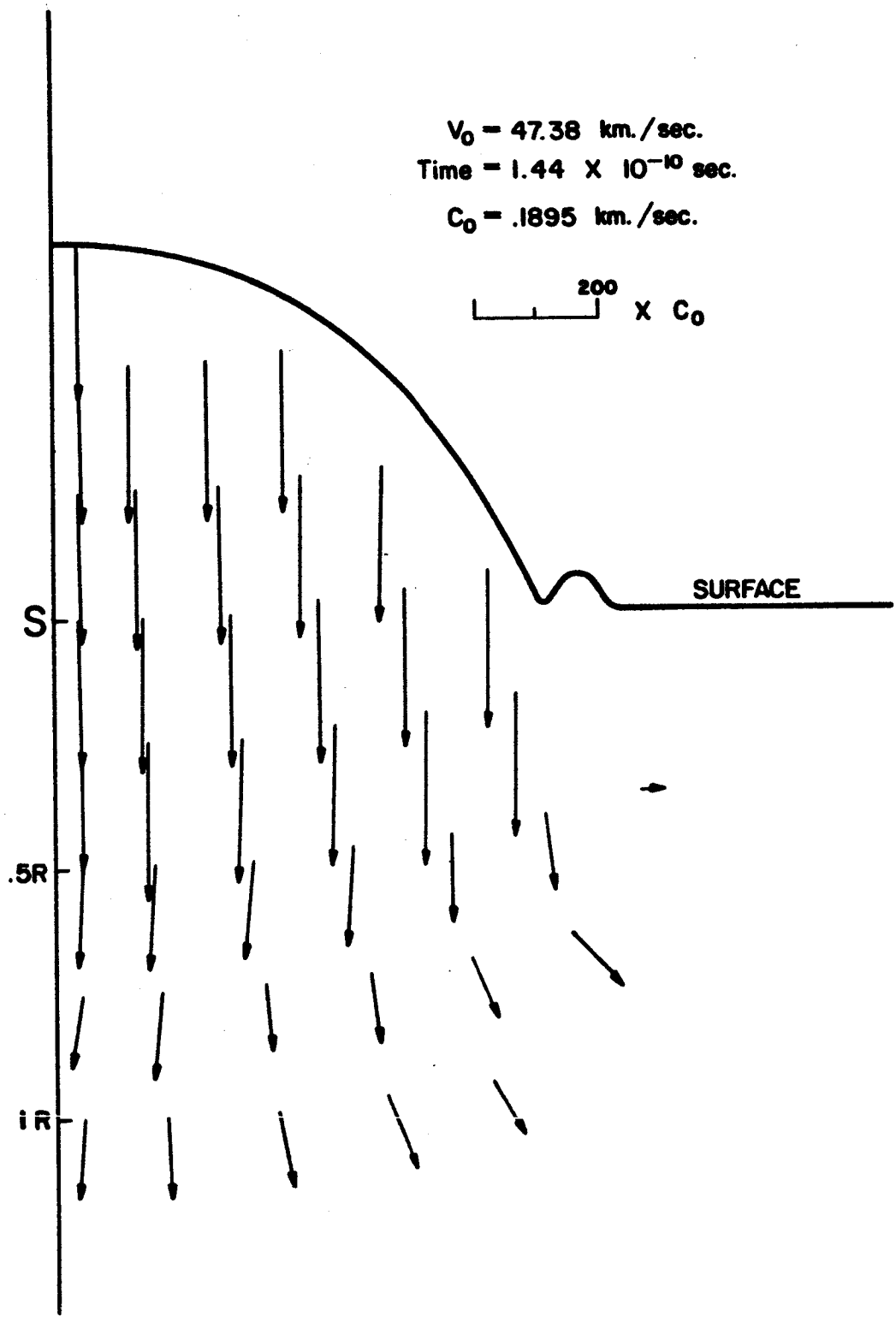

Figure 29. Velocity Distribution, Case V (Time = 1.44×10^{-10} seconds)

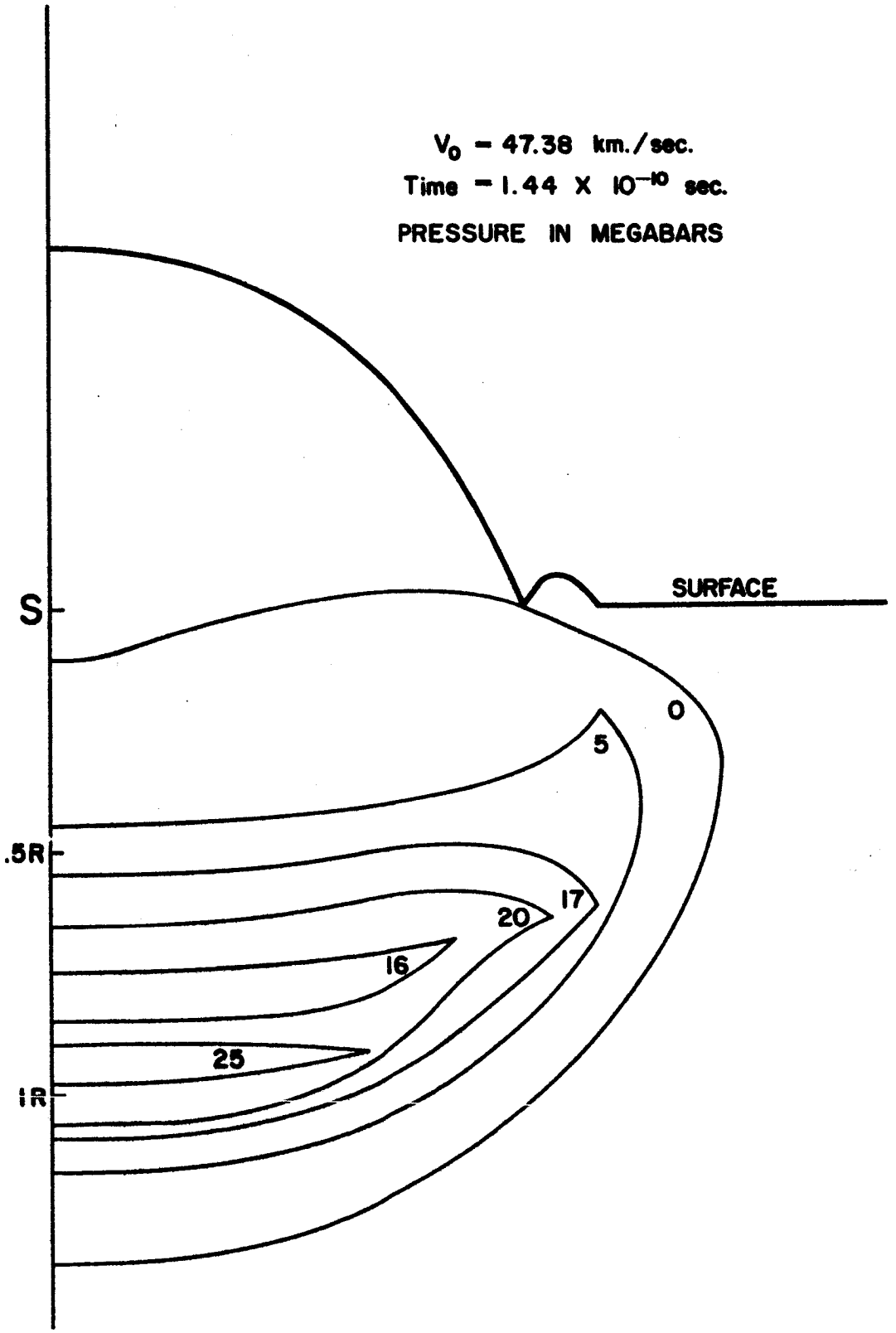

Figure 30. Pressure Contours, Case V (Time = 1.44×10^{-10} seconds)

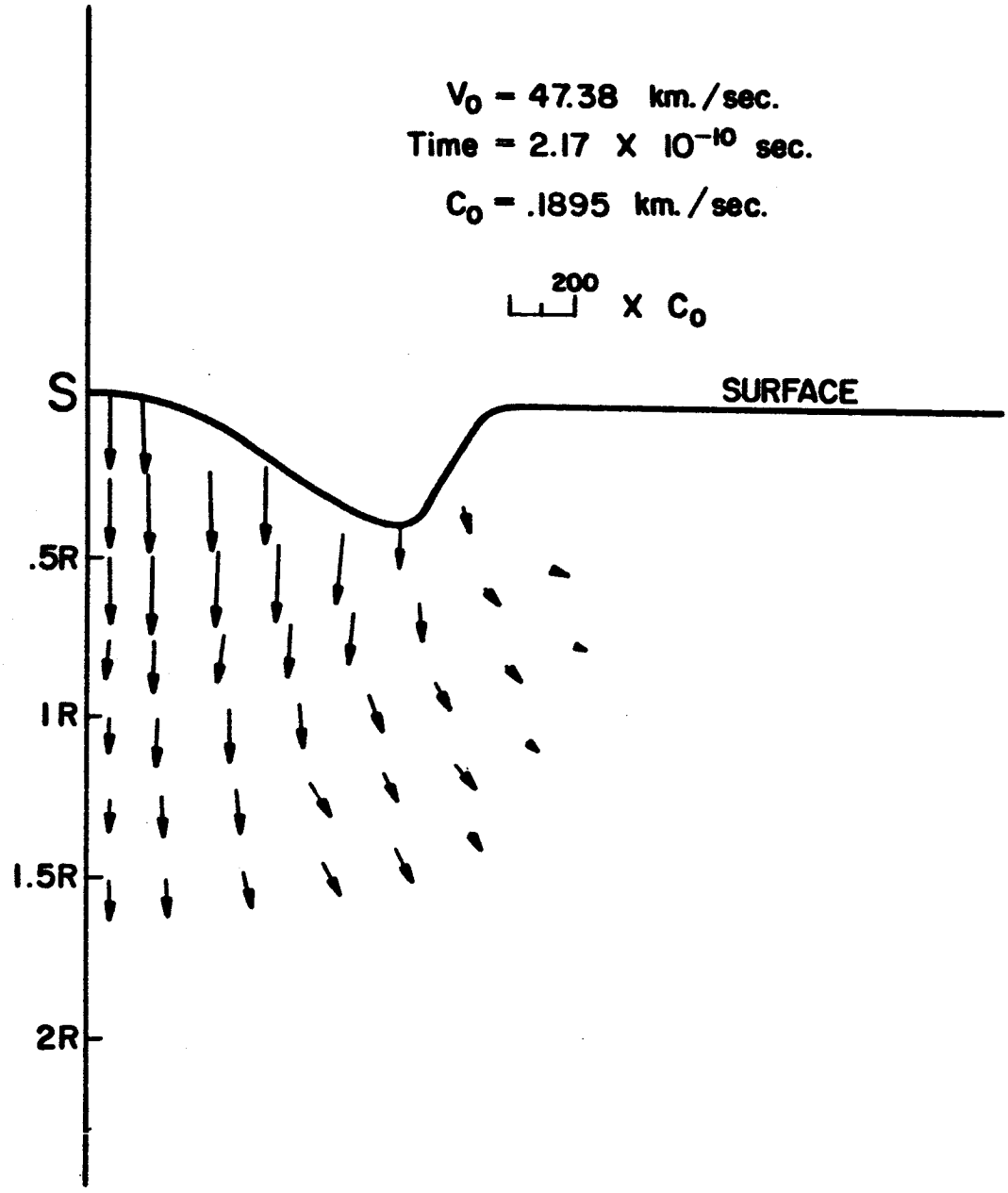

Figure 31. Velocity Distribution, Case V (Time = 2.17×10^{-10} seconds)

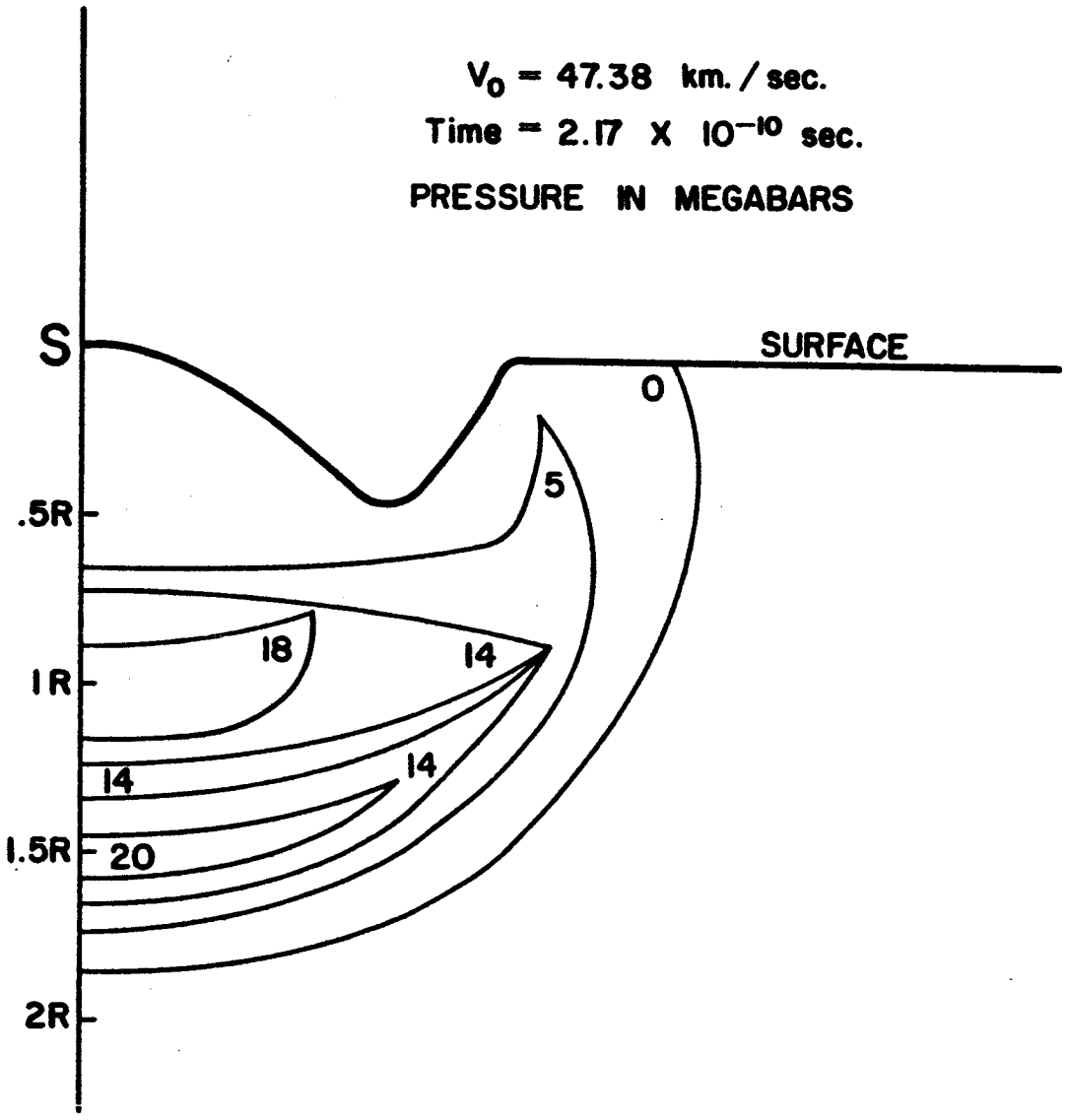

Figure 32. Pressure Contours, Case V (Time = 2.17×10^{-10} seconds)

integrity as it penetrates the target. A change in radial scale has occurred at this time; that is, a machine condensation of the finite difference mesh has taken place. The pressure distribution, in Figure 32, does not make such a clear distinction between affected and unaffected material. The peak pressure has begun to decay. It is interesting to note that the linit of this pressure distribution, the zero line determining the progress of the primary shock wave, is an approximately circular arc centered at the point of impact, S.

After reflection of the secondary shock wave has occurred along all of the free surface of the micrometeoroid, the velocity distribution is changed near the free surface. All material of the original projectile has been subject to shock compression. This material now starts to expand and an expansion or rarefaction wave proceeds from the vacuum boundary. The largest velocities sustained by aluminum are about forty percent of V_o. Upward motion of the surface near the edge of the expanding cavity can also be seen in Figure 33. The corresponding pressure disturbution is shown in Figure 34. Evidence of the shape of the micrometeoroid influencing the time of release waves can be inferred from the spacing between the material surface, which is at zero pressure and the four megabar line.

The velocity distribution, in Figure 35, depicts the motion of material ahead of the forming crater. Each vector shown is moving away from the expanding hole. The pressure

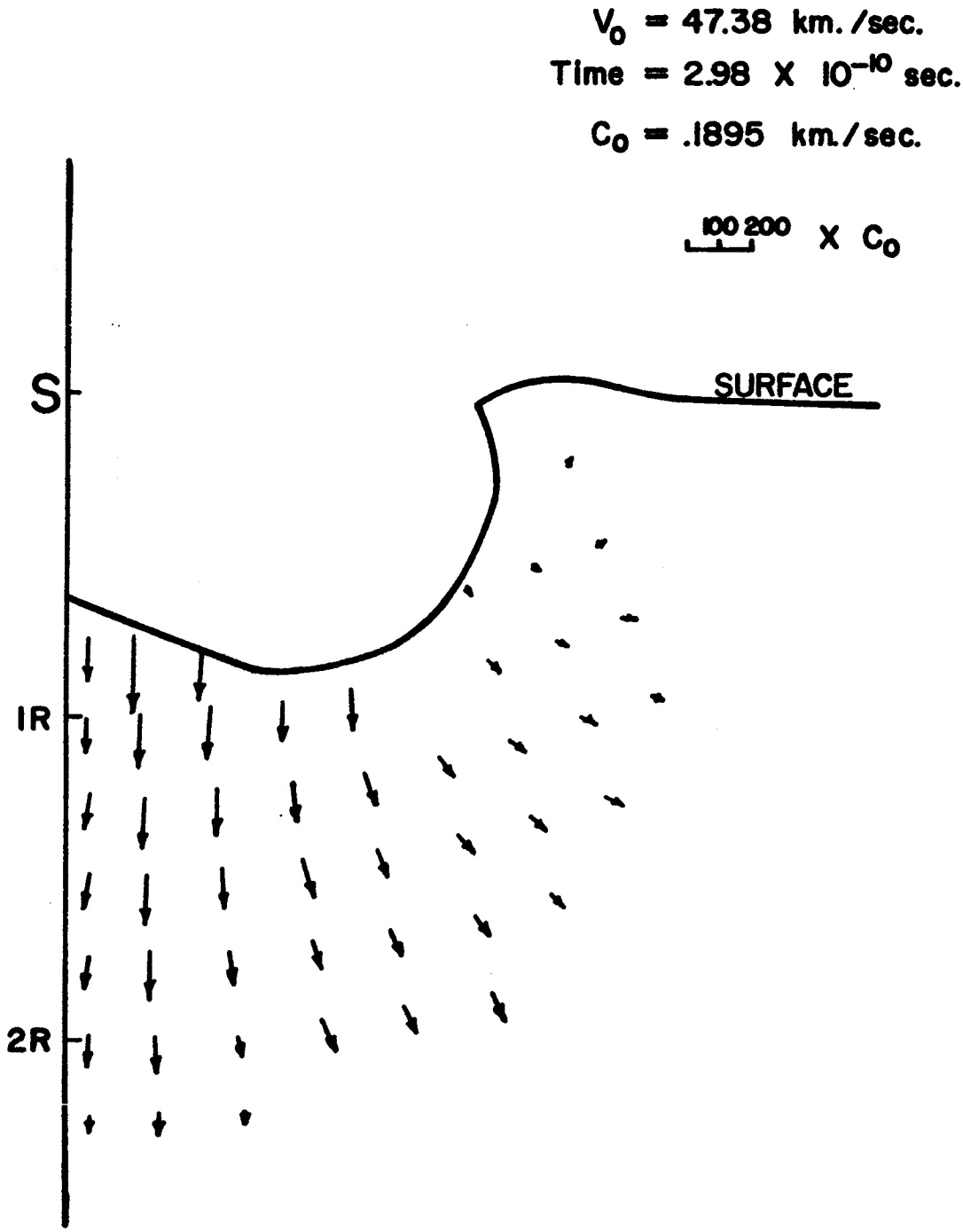

Figure 33. Velocity Distribution, Case V (Time = 2.98×10^{-10} seconds)

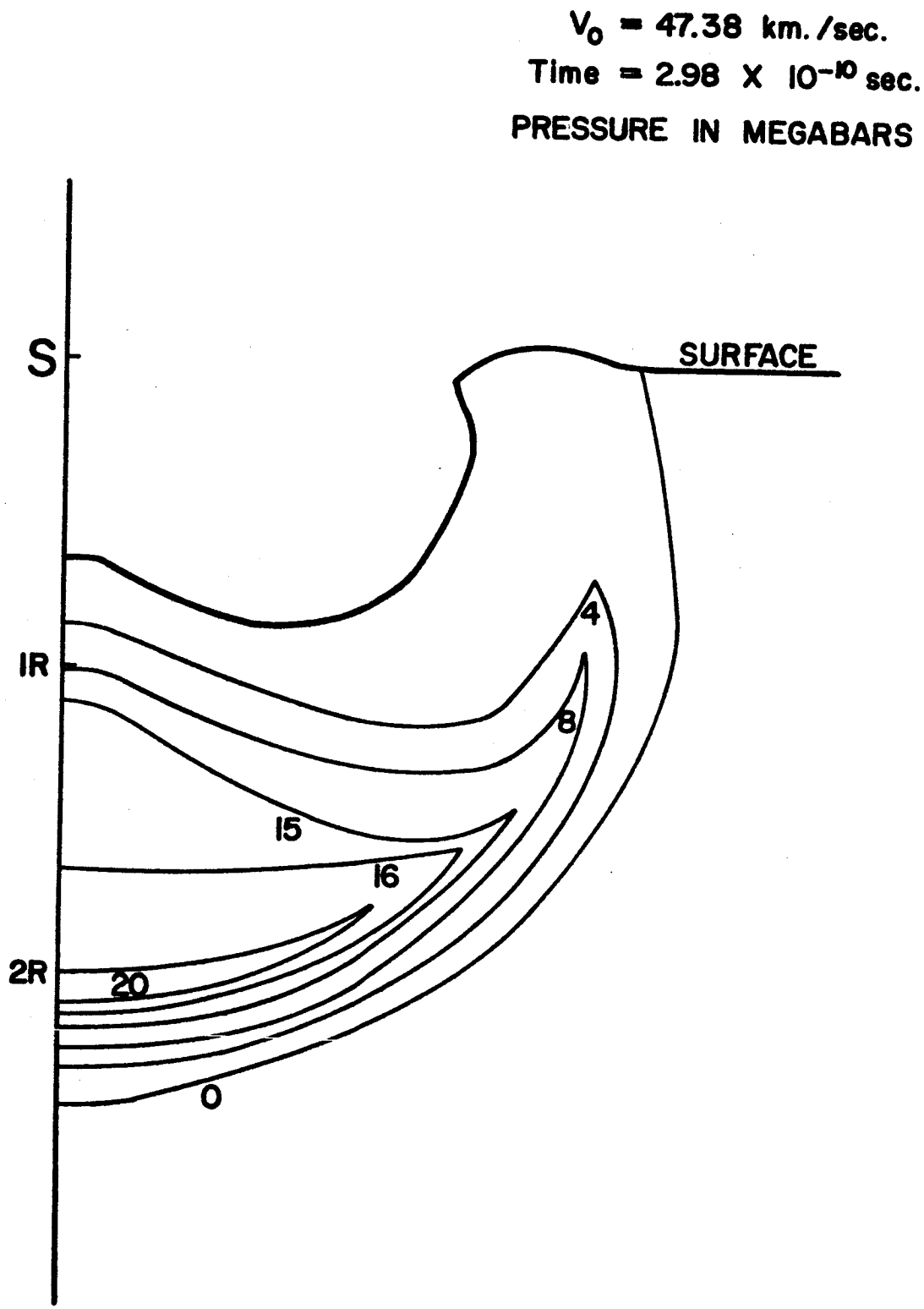

Figure 34. Pressure Contours, Case V (Time = 2.98×10^{-10} seconds)

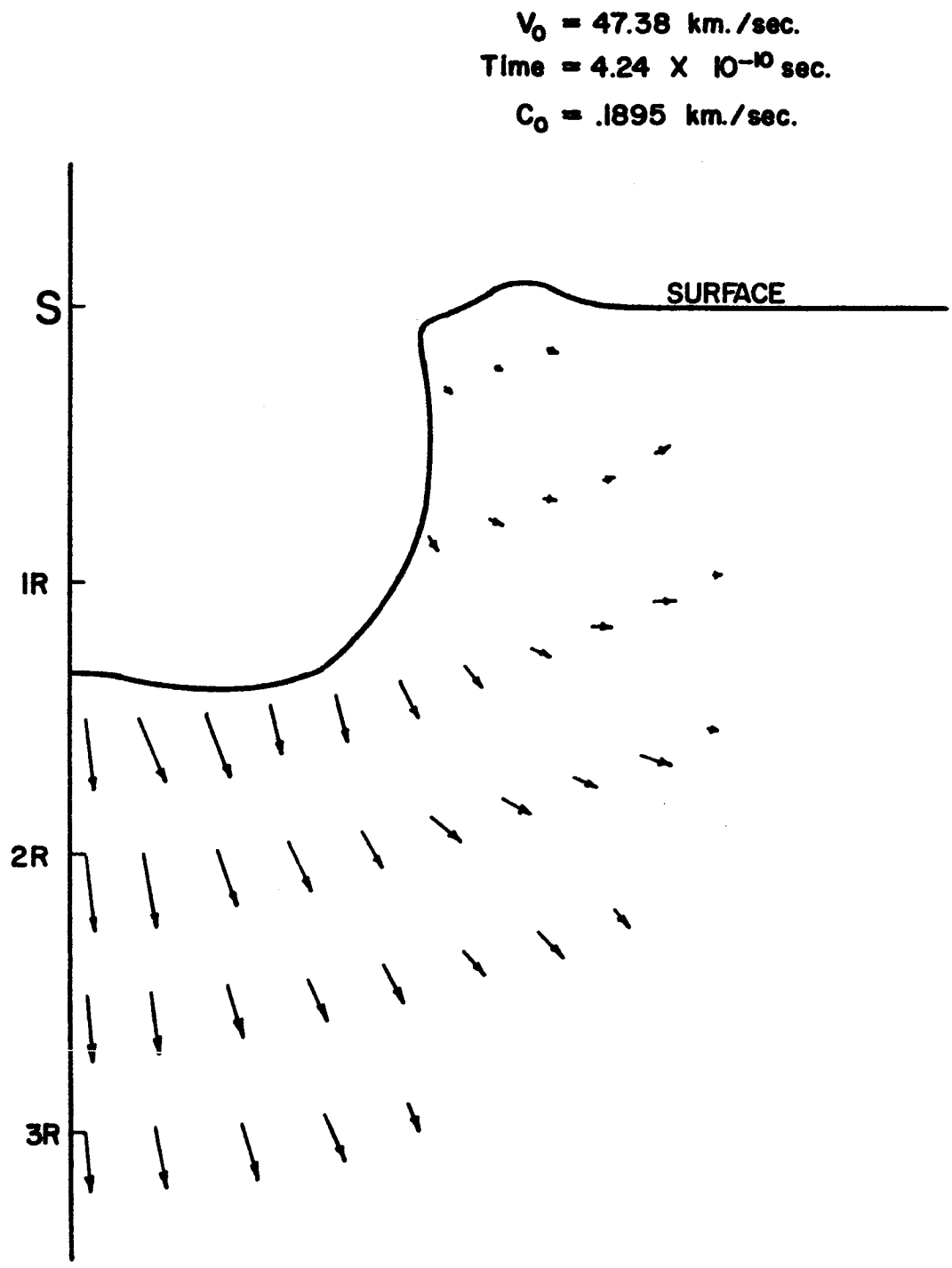

Figure 35. Velocity Distribution, Case V (Time = 4.24×10^{-10} seconds)

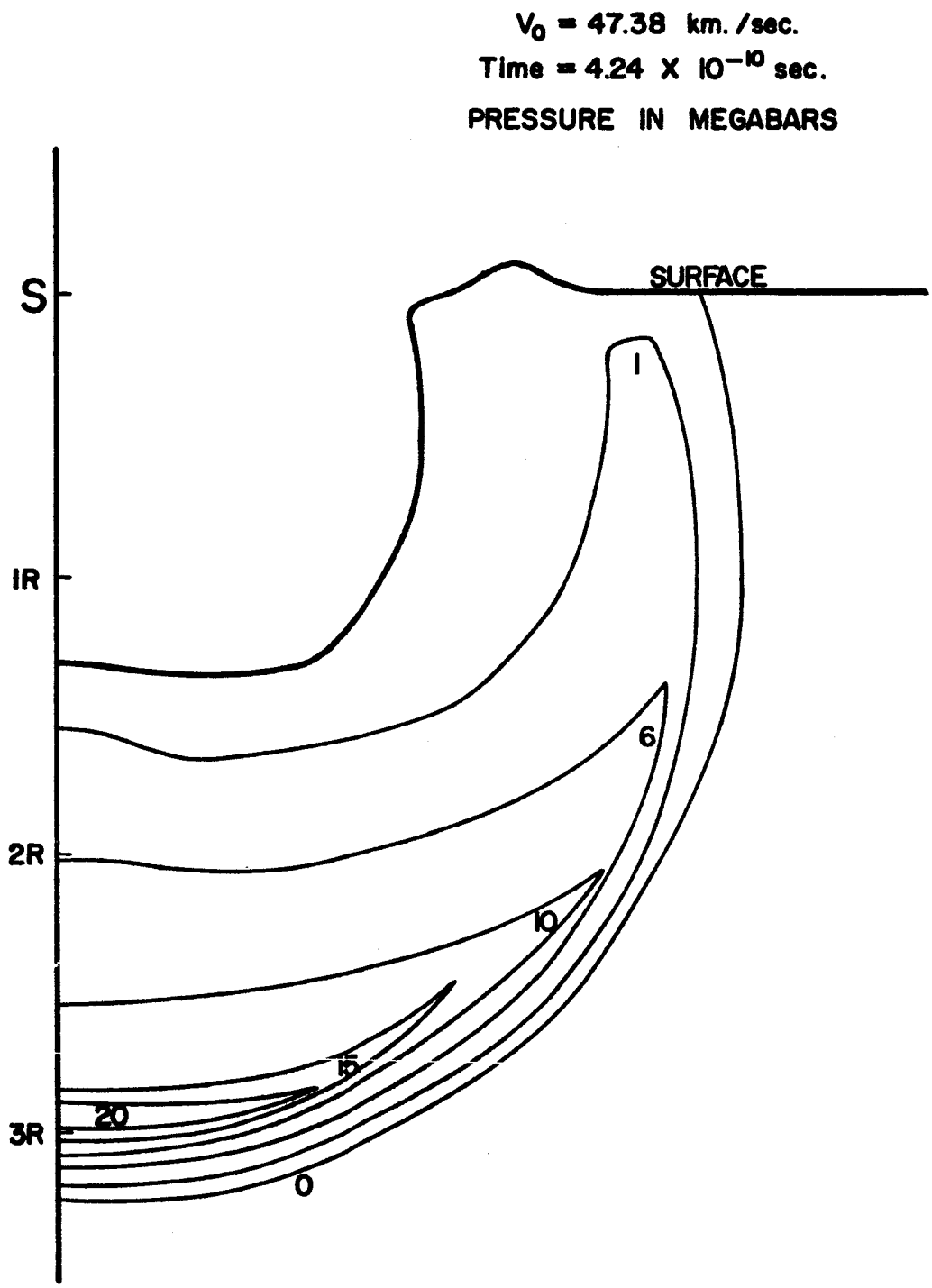

Figure 36. Pressure Contours, Case V (Time = 4.24×10^{-10} seconds)

at this time, Figure 36, exhibits one shock wave traveling in the target. Again, some movement of material above the original target surface line is indicated. This is correlated with the experimentally observed spray ejected by hypervelocity impact processes.

As the dimensions of the finite difference mesh are modified, the time increments used in the numerical calculation increase. One result of such computer directed condensations of the net is that the decay of the primary shock wave becomes more evident. This can be seen in both Figures 37 and 38. As the distance scale increases, the shock parameters decrease. The isobars in Figure 38 display somewhat less of a radial quality about the point of impact. Part of this proceeds from the retardation of the disturbance moving along the free surface of the target. This slow down results from the ejection of material from the target and from the failure of the aluminum equation of state to adequately describe the material. This latter point will be discussed in a later section.

The flow progresses at later times in the calculations as shown in Figures 39 and 40. The irregularity of the surface shape changes with time. The peak values of the shock wave have decayed even more at this time. The peak pressure in Figure 40, is down to 4 megabars. Illustrations of this type are quite representative of shock waves traveling in an inviscid fluid.

Further cell changes have been made in the time for

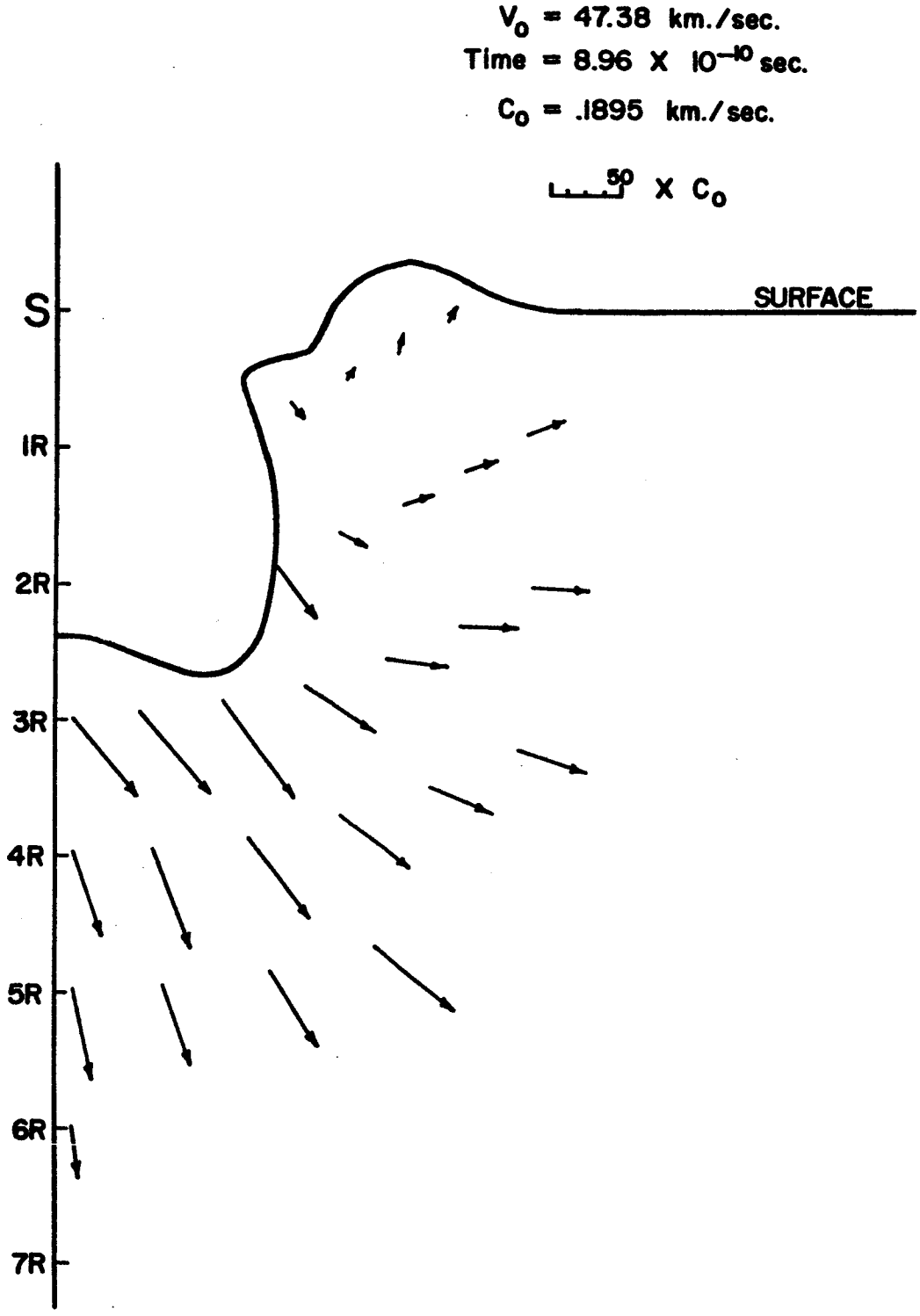

Figure 37. Velocity Distribution, Case V (Time = 8.96×10^{-10} seconds)

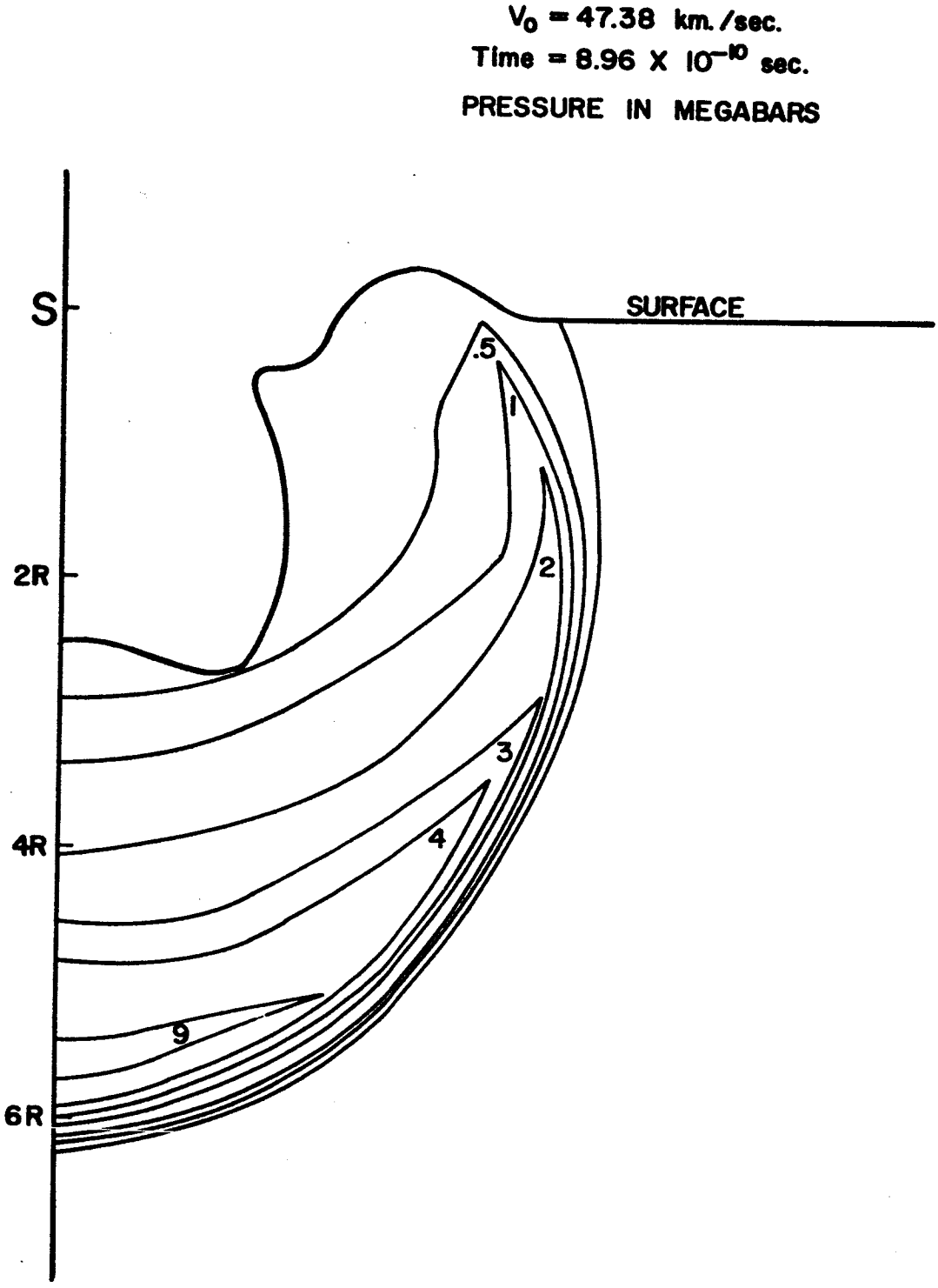

Figure 38. Pressure Contours, Case V (Time = 8.96×10^{-10} seconds)

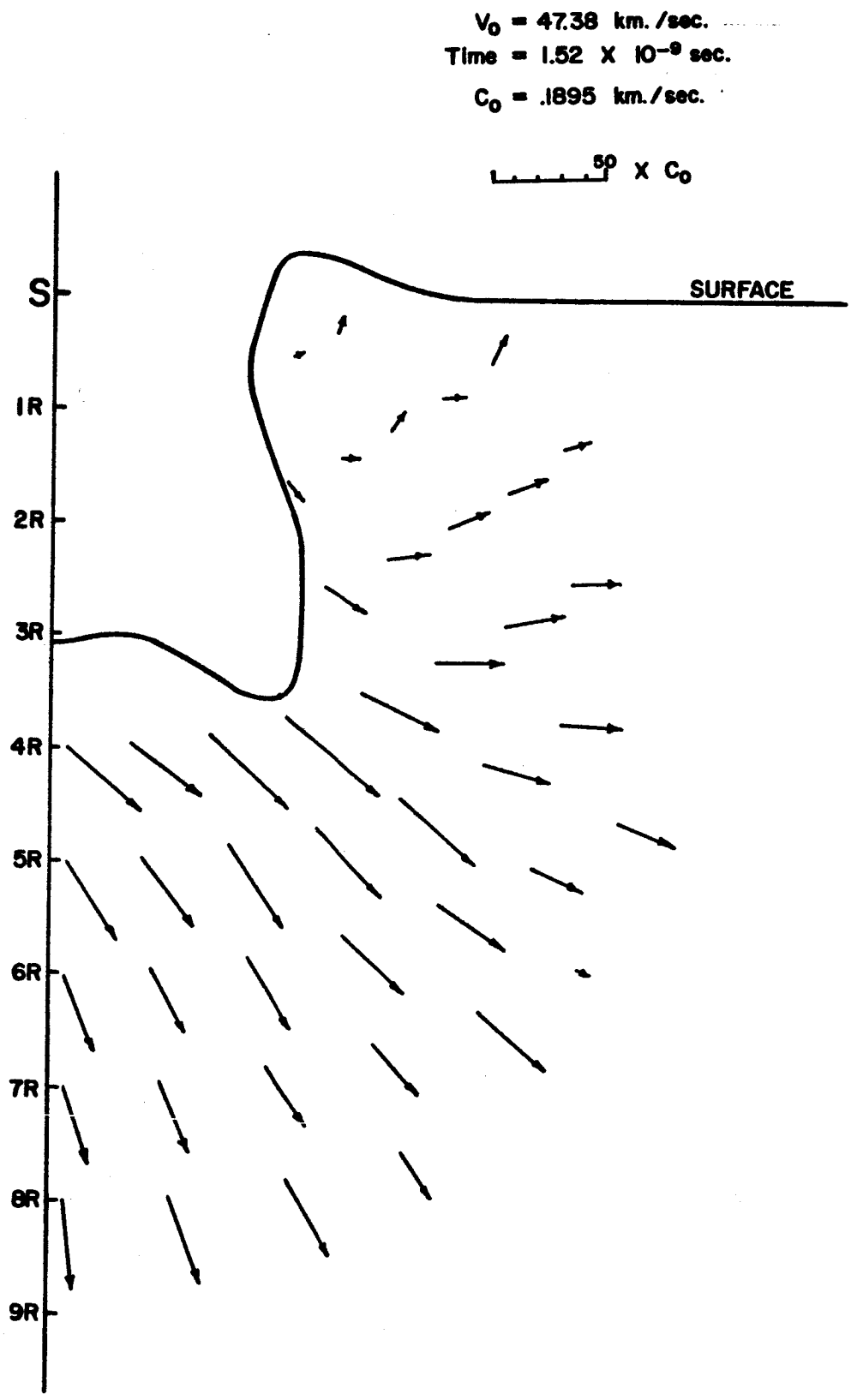

Figure 39. Velocity Distribution, Case V
(Time = 1.52 x 10^{-9} seconds)

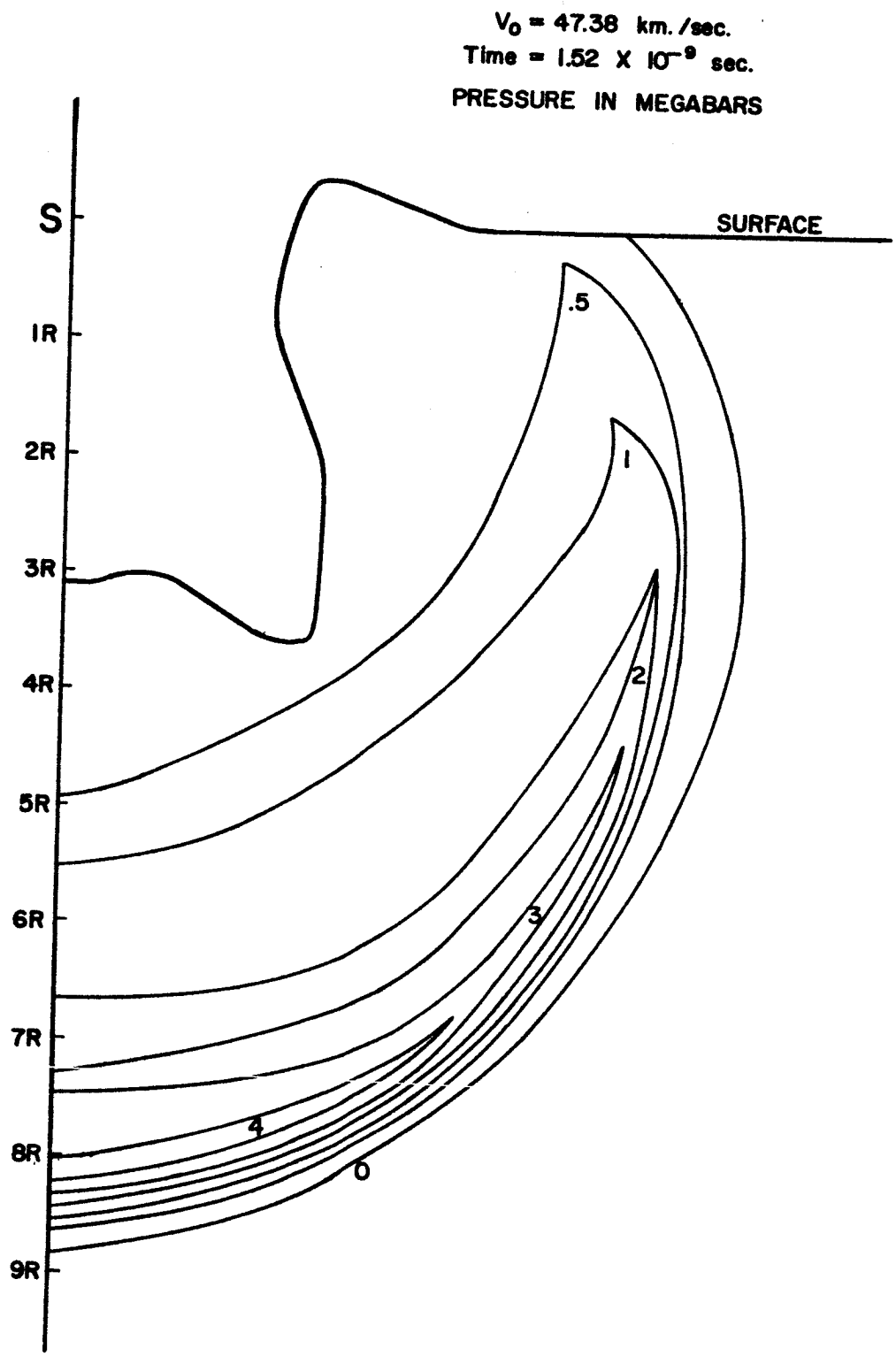

Figure 40. Pressure Contours, Case V (Time = 1.52×10^{-9} seconds)

distributions shown in Figure 41 and 42. The velocity vectors now indicate some small scale irregularities near the free surface and the leading edge of the fluid disturbance. The pressure distribution, in Figure 42, shows fairly smooth curves characteristic of the primary shock wave structure.

The last results obtained in the computer program for Case V are presented in Figures 43 and 44. The two distributions are terminal only in an arbitrary sense. They do not and cannot, represent the final stages of crater formation. The deepest part of the cavity is centered about the impact point. The large amount of material shown above the original surface is believed incorrect. The exact cause and correction of this difficulty will be discussed later. The peak velocity shown in Figure 43 is less than ten per cent of the initial impact velocity, V_o . Further calculations beyond this time would not provide useful results. A large part of the affected region is quite turbulent. The peak pressure occuring in Figure 44 is less than five per cent of that found in the initial stages of the basic assumptions of this work.

Cavity Formation

The purpose of the study of hypervelocity impact studies is to enable prediction of micrometeoroid damage to space vehicles. The assessment of such impacts is quite often done in terms of penetration or crater size related to initial impact velocity values. The numerical solution

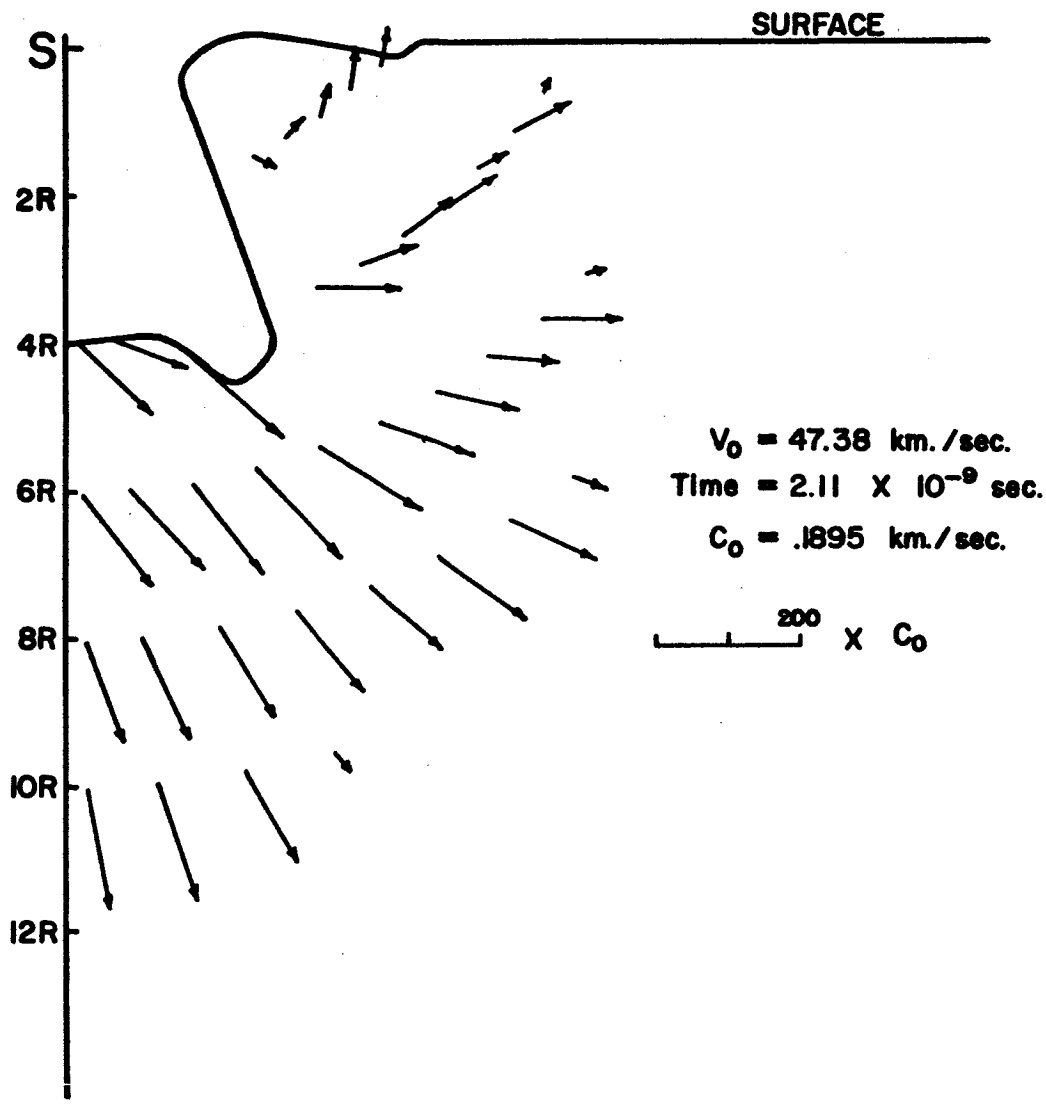

Figure 41. Velocity Distribution, Case V (Time = 2.11×10^{-9} seconds)

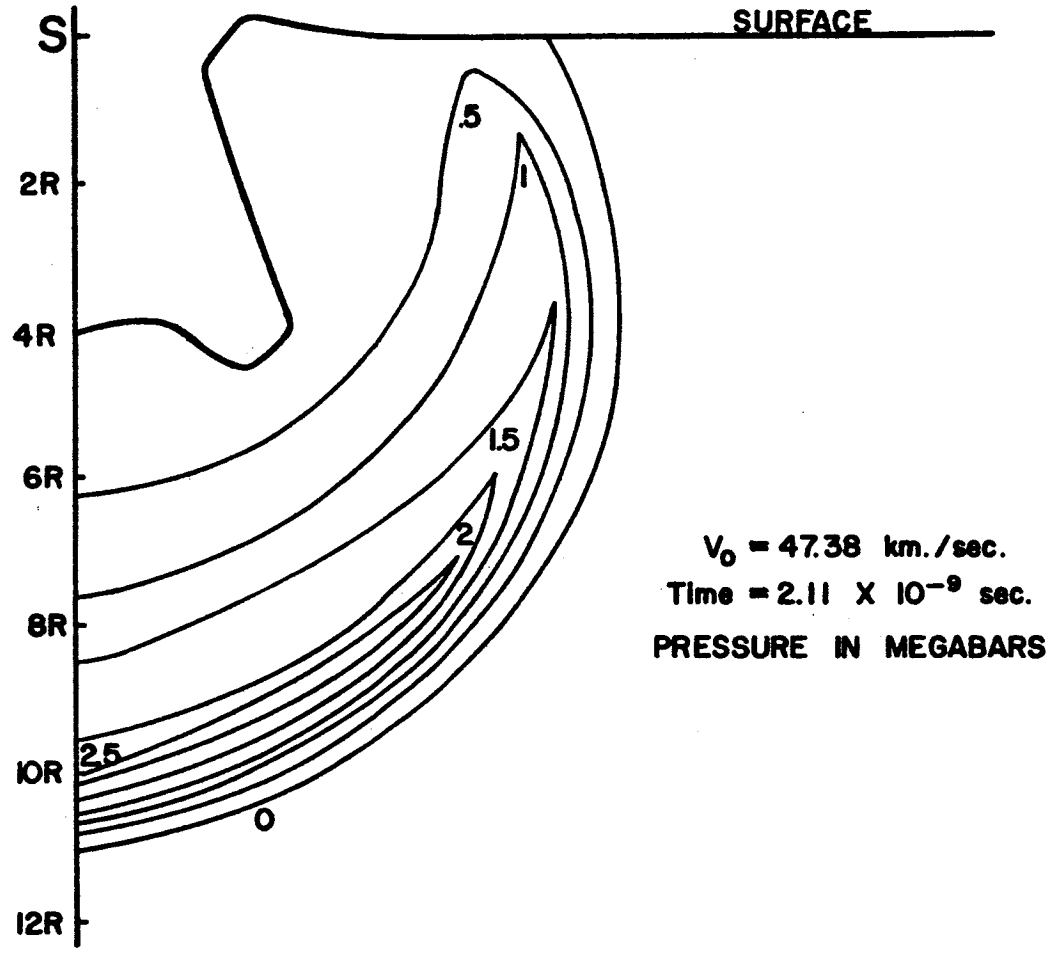

Figure 42. Pressure Contours, Case V (Time = 2.11×10^{-9} seconds)

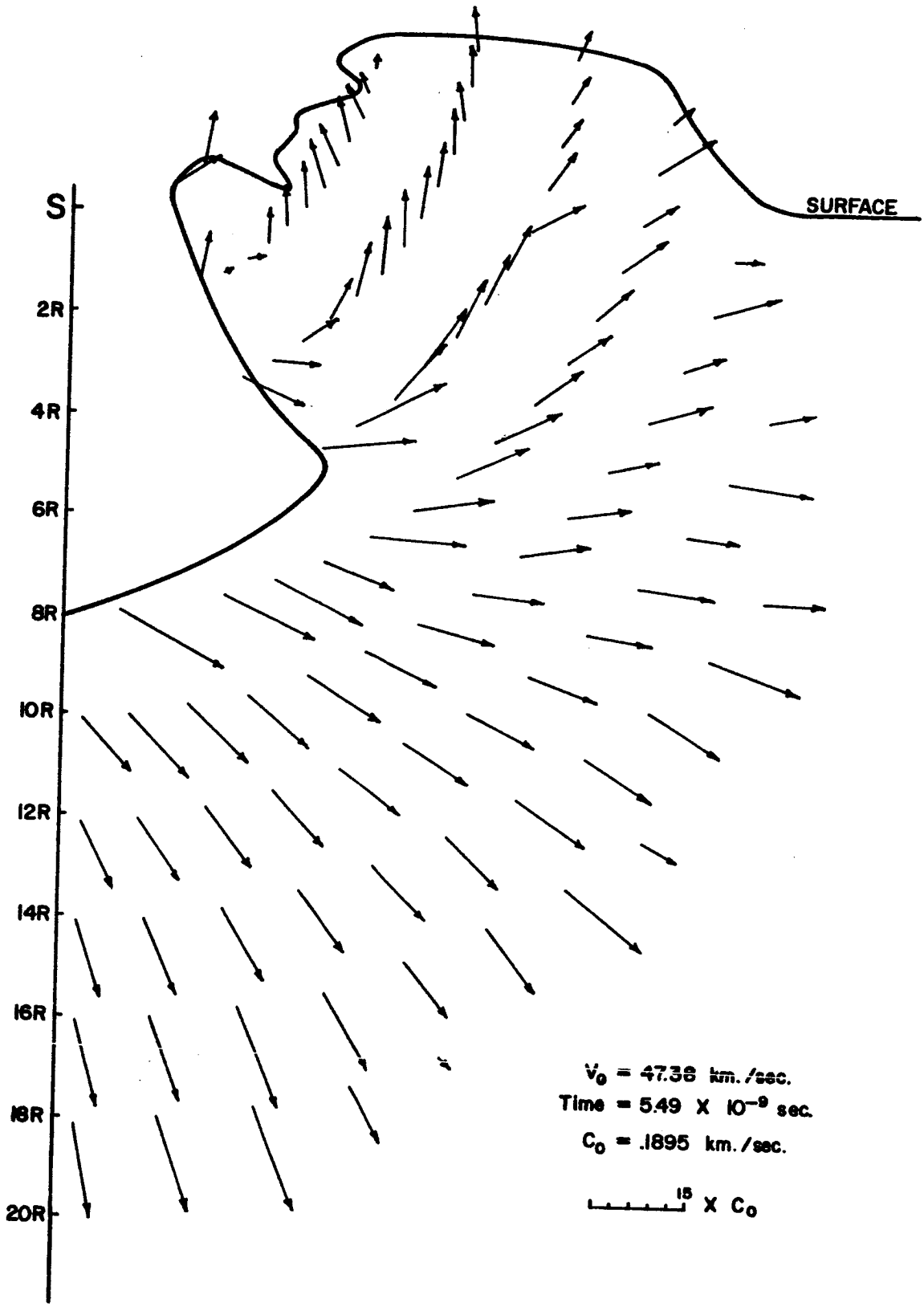

Figure 43. Velocity Distribution, Case V (Time = 5.49×10^{-9} seconds)

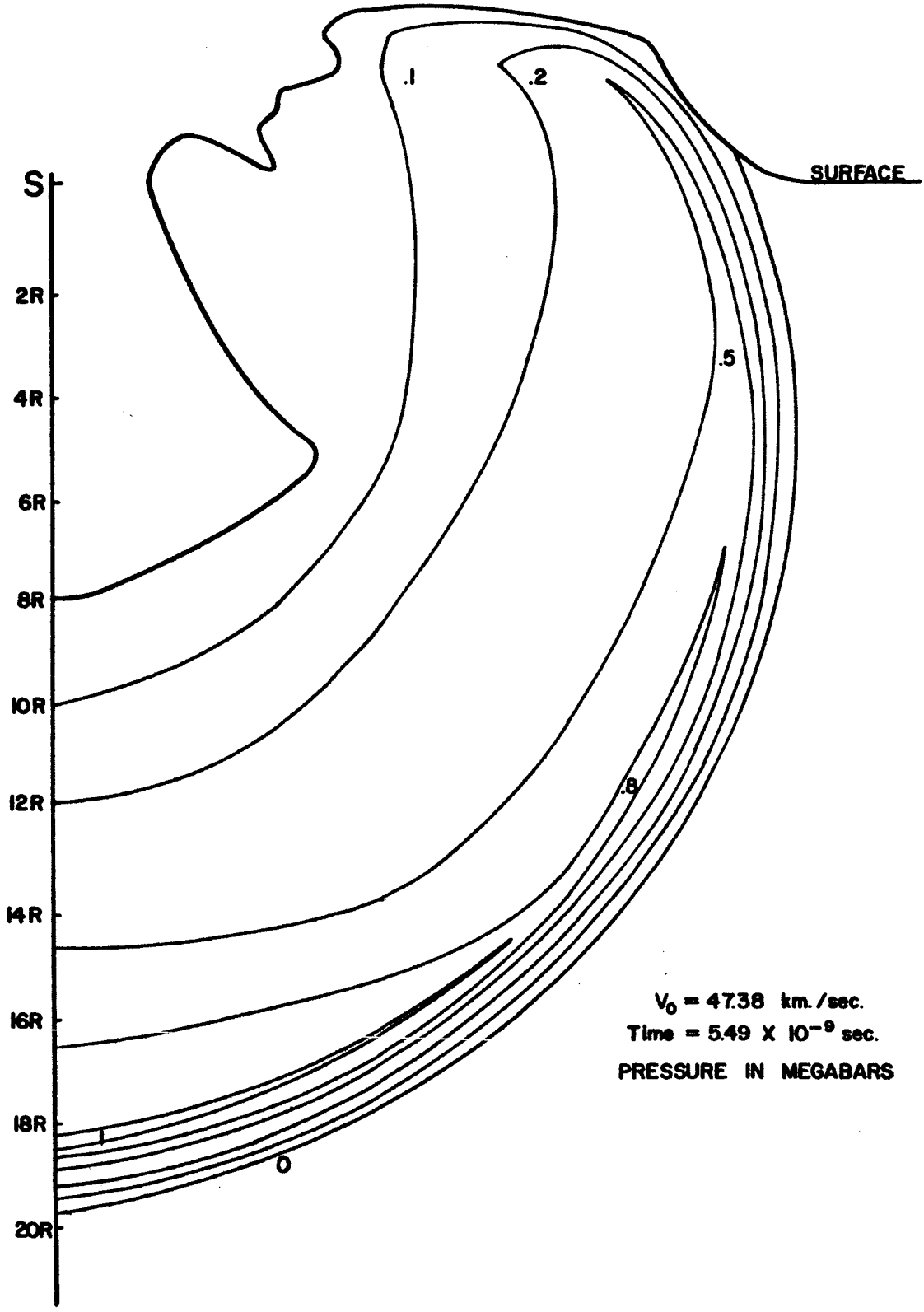

Figure 44. Pressure Contours, Case V (Time = 5.49×10^{-9} seconds)

presented for the hydrodynamic model shows the initial and middle stages of cavity development. The resolution afforded by the numerical calculations is indicated in Figure 45. Cells are shown sketched in near the aluminum-vacuum boundary approximately to the same scale as used by the computer program. Interface cells, those cells which are partially empty, are indicated by shading. More information than shown is provided by the computer print outs. The fraction of each cell which is filled with is given for each mixed cell. This helps in placing the boundary at any one time step. There is some latitude in positioning this line, but possible errors are less than one-half a cell dimension.

In order to observe the formation of the depression, a series of penetration versus time curves are shown in Figures 46 through 54 for four of the six cases solved. Such illustrations also give an overall view of the nature of the soluion obtained.

The mean velocity of free space micrometeoroids in the vicinity of the earth is about 36 km/sec. (2). Case IV was solved for an impact of this velocity. This case provided more data than any other. Positions of the material surface are shown for various times in Figure 46 through 48. The time for each curve is given in each Figure.

The progress of the solution describes the "swallowing" of the incident particle. The momentum and energy transferred from the micrometeoroid to the target compress the aluminum and cause the material to move into the target

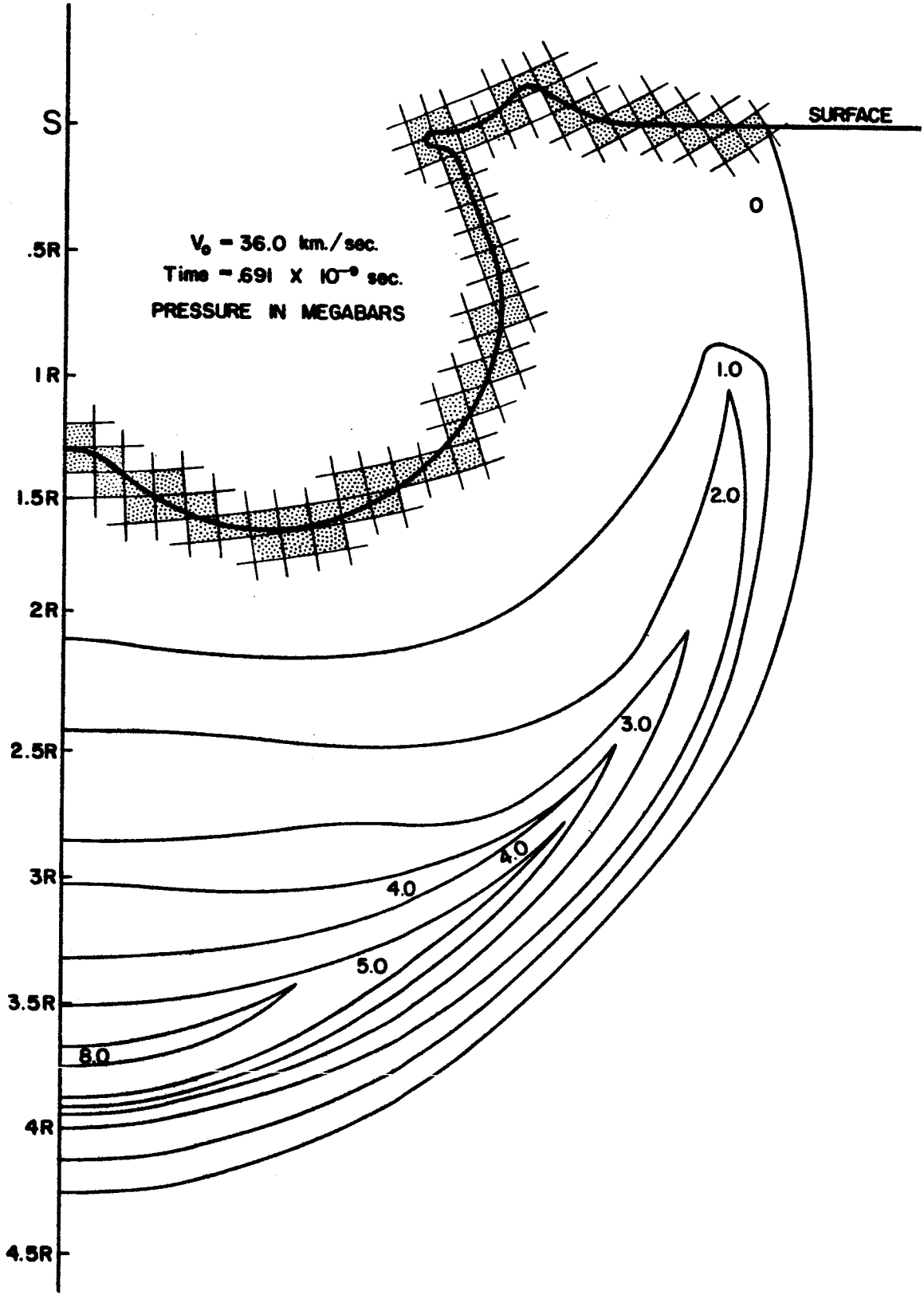

Figure 45. Pressure Contours, Case IV (Time = $.691 \times 10^{-9}$ seconds)

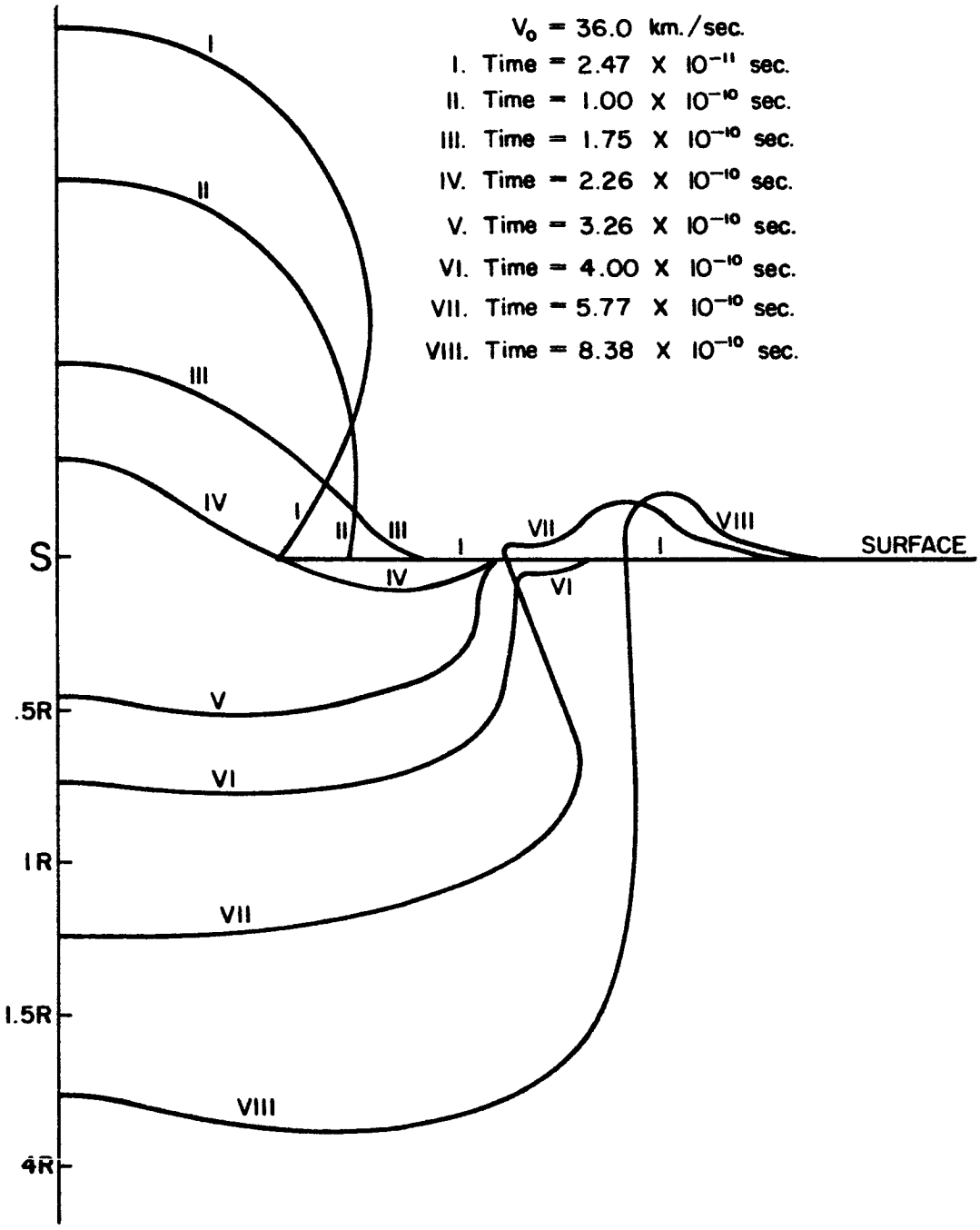

Figure 46. Position of Surface at Various Times, Case IV

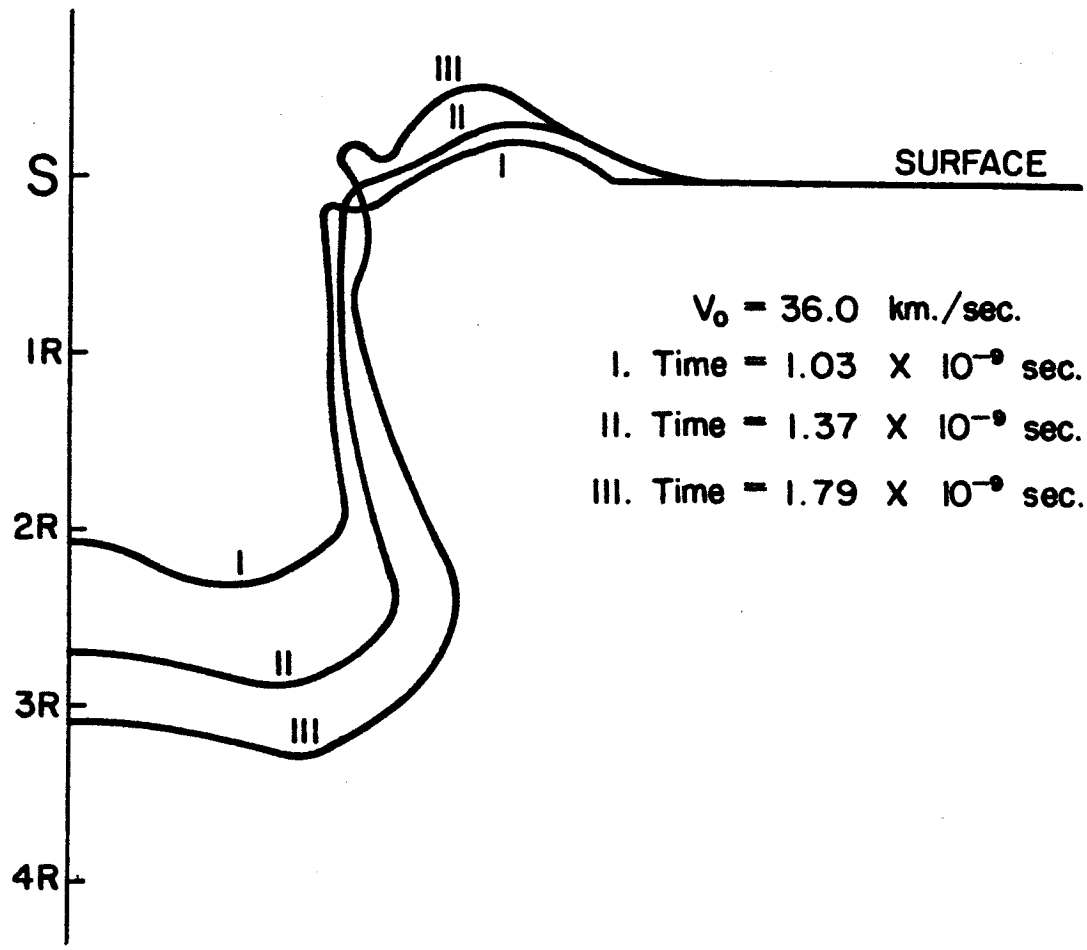

Figure 47. Position of Surface at Various Times, Case IV

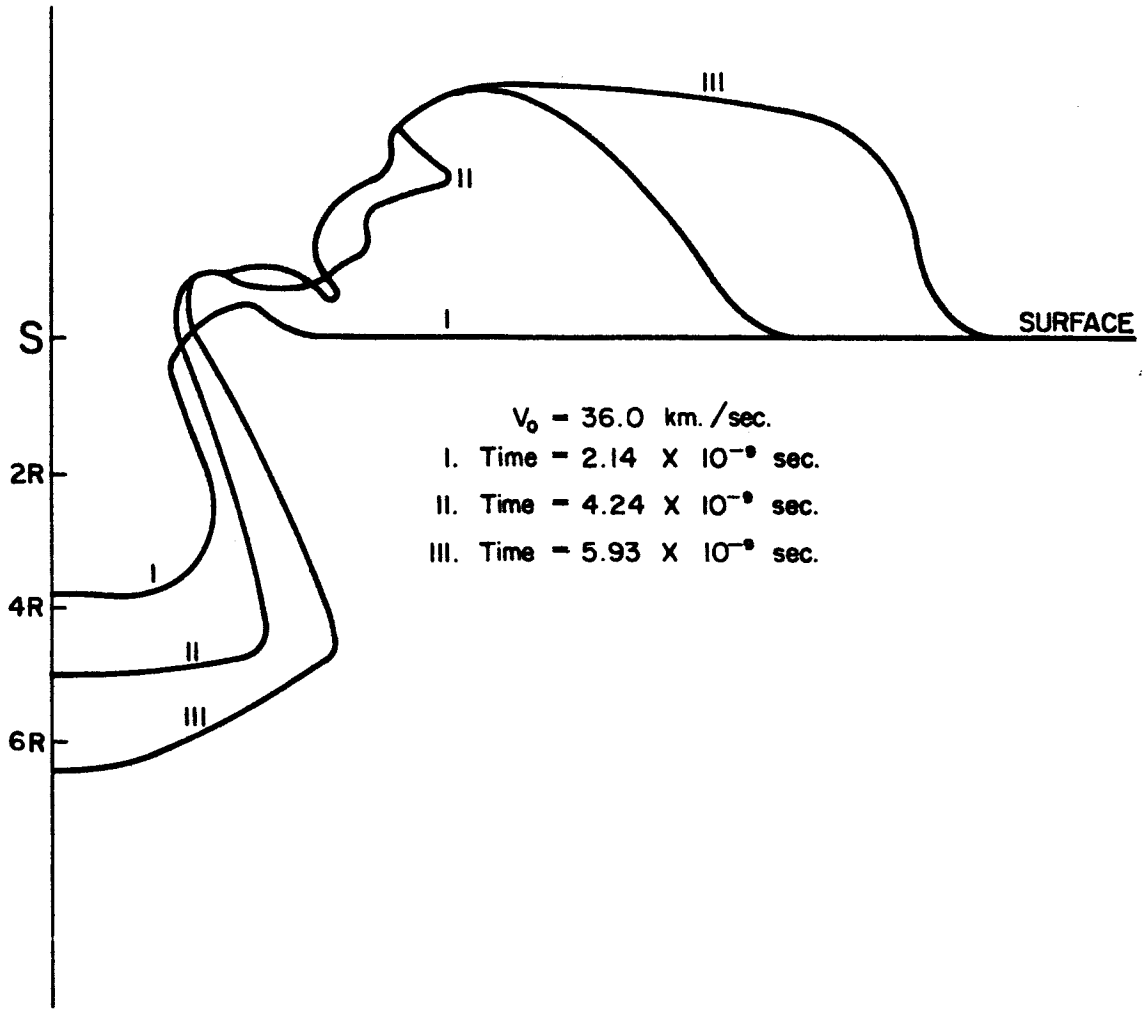

Figure 48. Position of Surface at Various Times, Case IV

forming a depression.

The initial motions of target and micrometeoroid are followed in Figure 46. At the latest times shown, material from the target is squeezed out by the disturbance of the micrometeoroids entrance. The cavity formation and ejection of material proceed in Figure 47.

The shape of the cavity assumes a more conical shape rather than the first noted radial symmetry about the point of contact. The curves shown in Figure 48 bear out this statement, although the deepest portions of the cavity are on a radial arc about S. The amount of material shown above the target surface is now very large. This difficulty arises in the following way. The finite difference mesh is not able to follow the motion very precisely at large distances behind S. The largest single cause of this accumulation of matter is the failure of the aluminum equation of state to describe states of tension. As seen from the numerical solution there is a strong tendency, evident in the graphs, for some target material to flow away from the entrance path of the micrometeoroid. This activity corresponds to the spray observed in hypervelocity cratering experiments. It is probable that the material expands to such states in which the density is less than that of normal aluminum. The equation of state, however, only allows states of compression or, at least, zero pressure. The density is required to be equal to or greater than normal density. This provision leads to an impasse near the distorted

portion of the surface where it is probable that densities less than normal would be seen. The shock wave moving in the lateral direction cannot propagate as freely as the pressure front penetrating along the normal axis. At the latest times, such as positions shown in Curves II and III of Figure 48, this fault leads to production of excess mass and energy in the fluid field.

Experimental data pertinent to high tension states of aluminum is not immediately available. It is hoped that future work will provide a more realistic equation of state. The present expression used is built up of curve fitting approximations valid only in specific regions. Substitutions of densities less than normal lead to results which are not physically acceptable or consistent.

The results for velocities of impact velocities greater than 36 km/sec. are quite similar to those just presented. Calculations for Case V, $V_o = 47.38$ km/sec. are shown in Figure 49. Calculations for Case VI, $V_o = 60.64$ km/sec. are given in Figures 50 through 53. Again, the accretion of material above the target surface prevents some of the freedom of motion expected. Also, if the mass were less, the velocity of ejection would be higher than shown in the present calculations.

Similar time traces for the lowest velocity considered, Case I in which $V_o = 5.68$ km/sec., are available and are different from the high velocity cases. Such curves, together with corresponding pressure distributions,

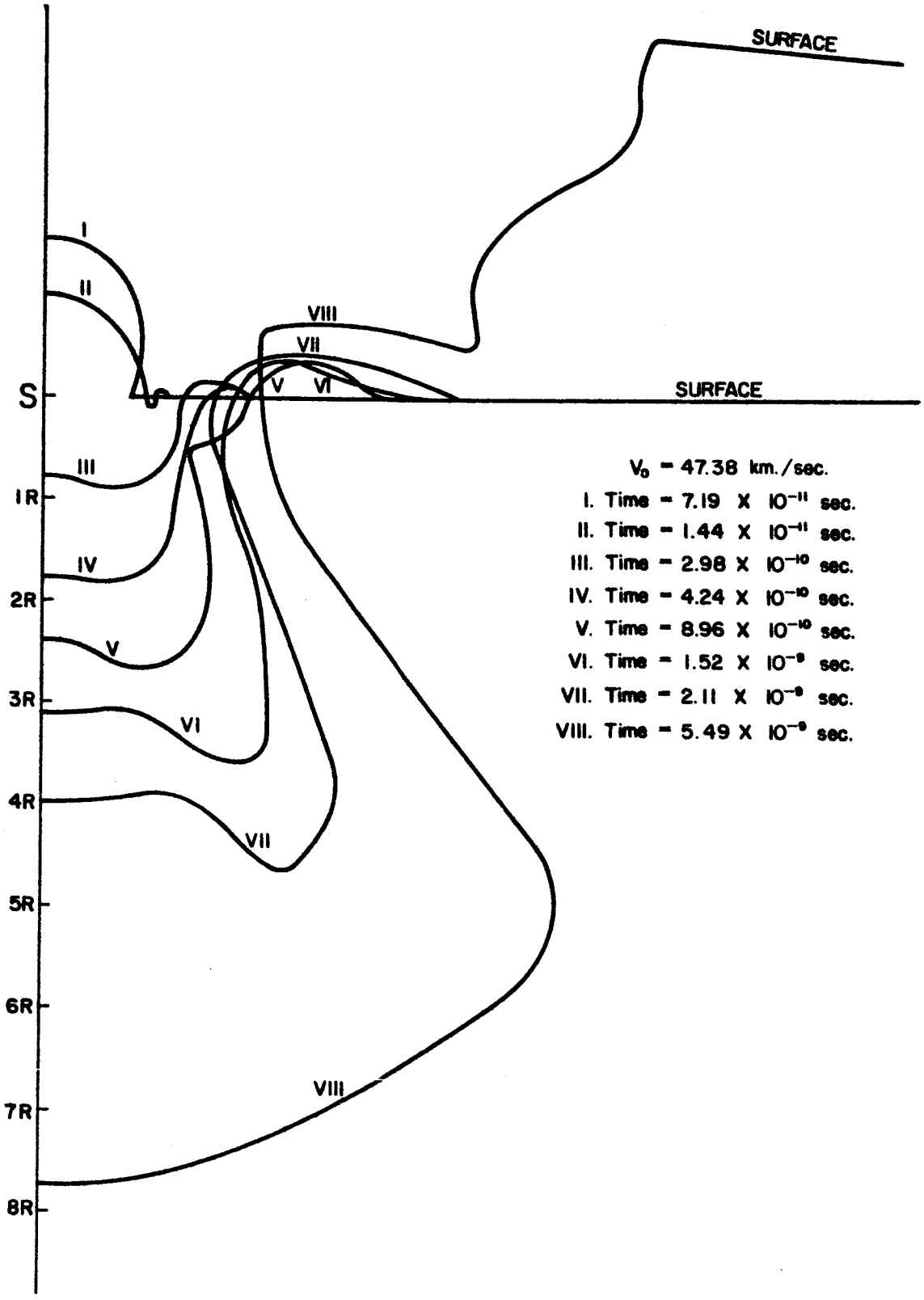

Figure 49. Position of Surface at Various Times, Case V

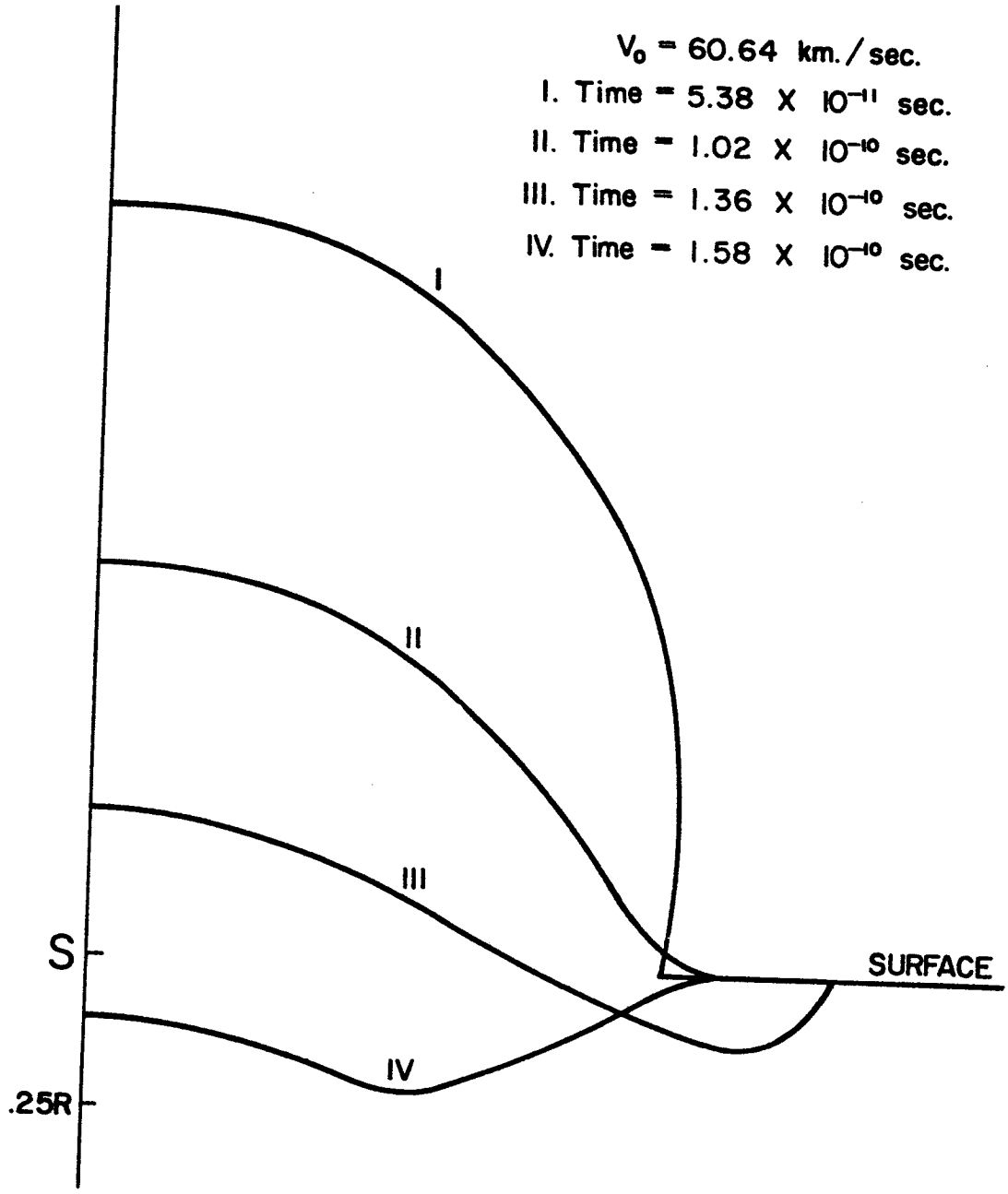

Figure 50. Position of Surface at Various Times, Case VI

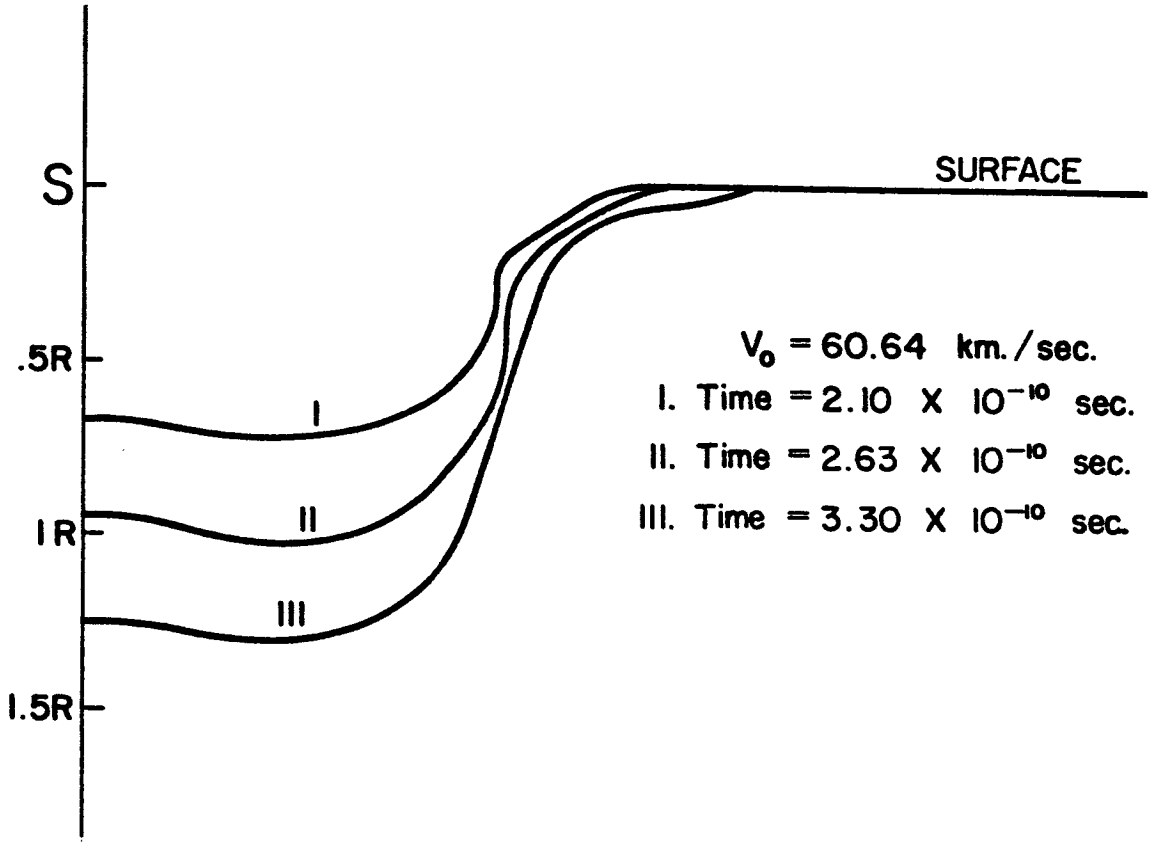

Figure 51. Position of Surface at Various Times, Case VI

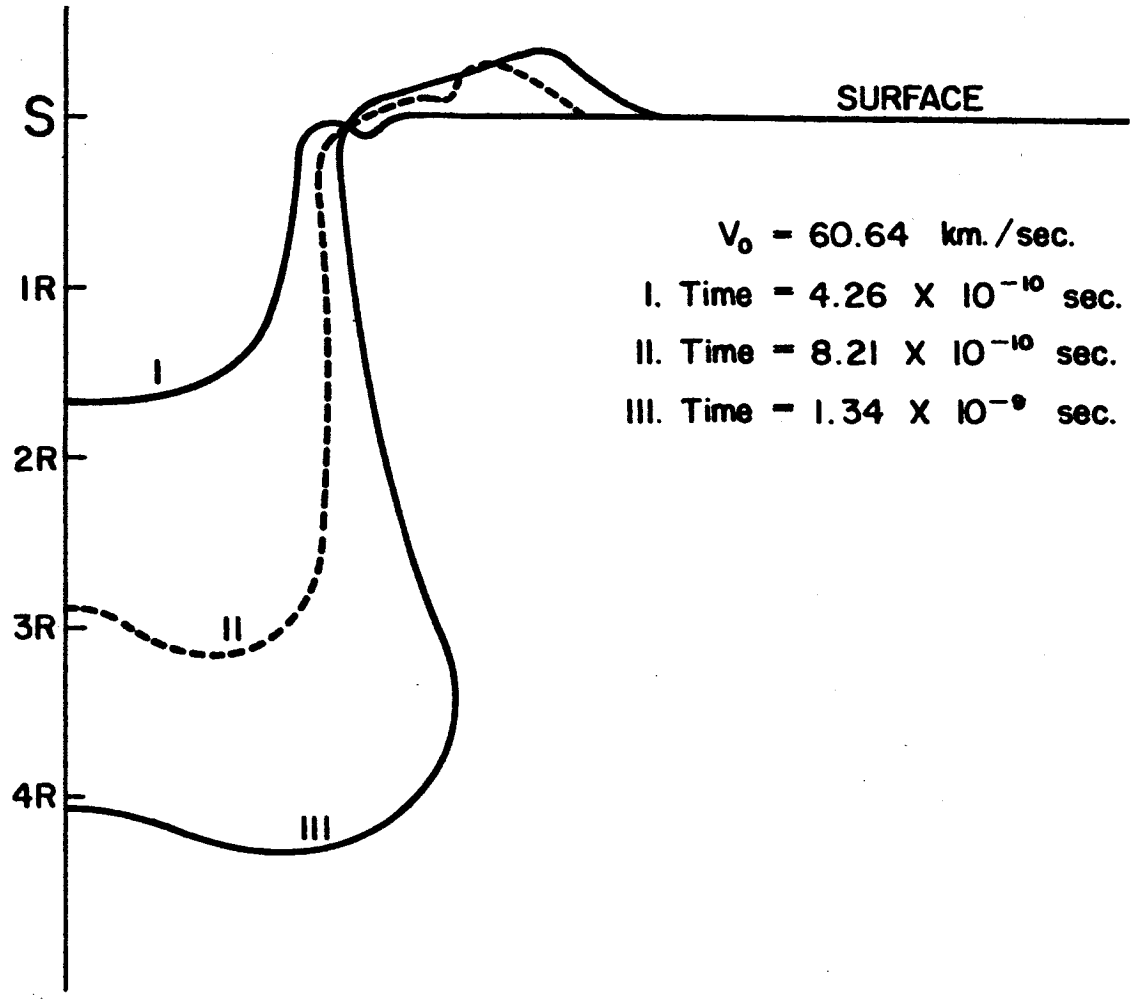

Figure 52. Position of Surface at Various Times, Case VI

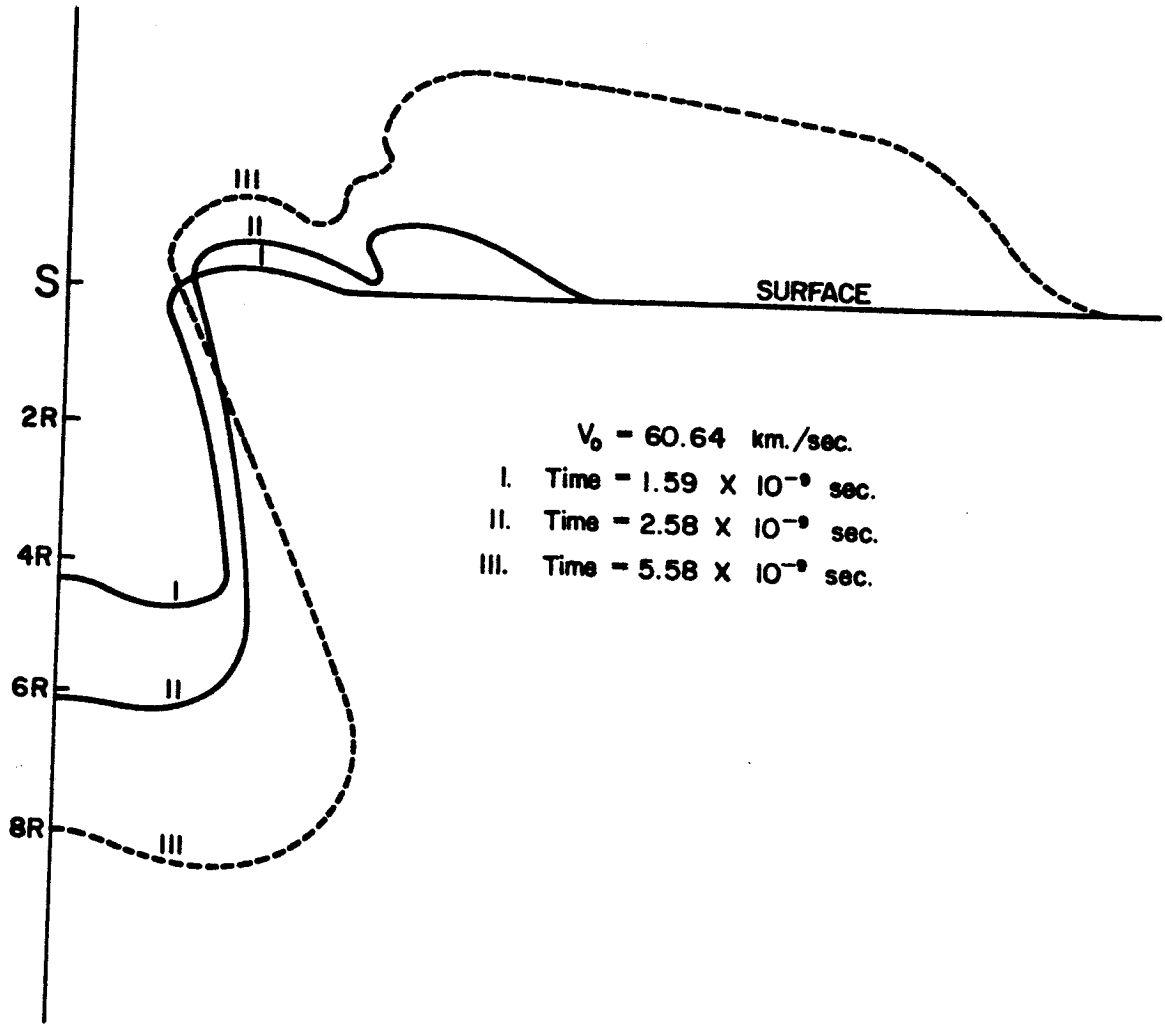

Figure 53. Position of Surface at Various Times, Case VI

are interpreted to indicate a shallower depression. The irregularity of the surface positon curves is quite noticeable. The last curve shown, however, in Figure 54, is completely radial from the point S to the original target surface line

Density Distributions

A slightly different view of the impact and a further study of the effects of the equation of state are given by a series of graphs of constant density contours. These illustrations were drawn in the same manner as the pressure distribution. Results for density distributions for Case V, $V_o = 47.38$ km/sec, are shown in Figures 55 through 59.

Density values result from solutions of the continuity of mass equation. Such values together with the internal energy determine the pressure in the hydrodynamic model. At peak pressure and peak density points, however, a shock process is occuring and the equation of state applicable is the Hugoniot curve. Such a relation is apparent at early times in the numerical solution where all disturbances are essentially by shock compression.

In the first stages of micrometeoroid penetration, the density behaves much like the pressure. A peak is formed slightly below the original point of contact. This peak is then broadened into two approximately equal shock waves. The propagation and reflection of these two fronts proceeds as discussed previously. Illustrations of the density

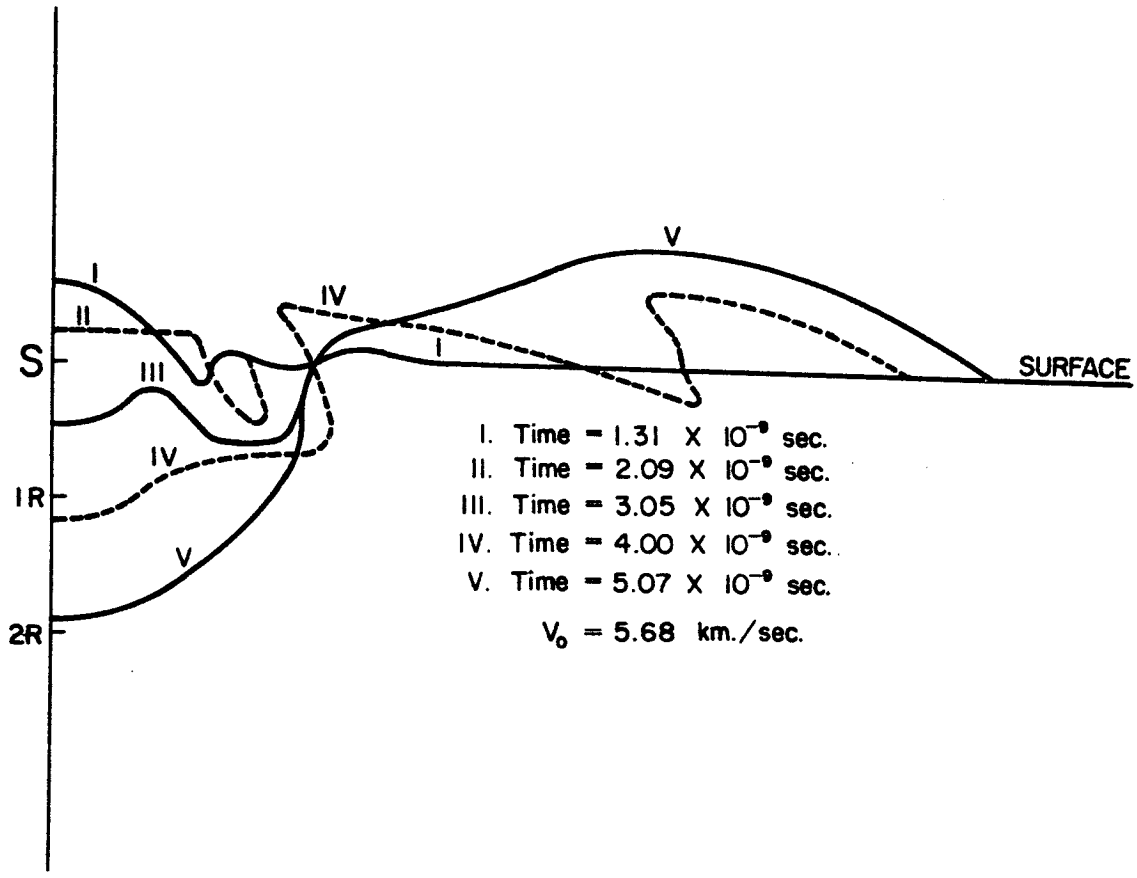

Figure 54. Position of Surface at Various Times, Case I

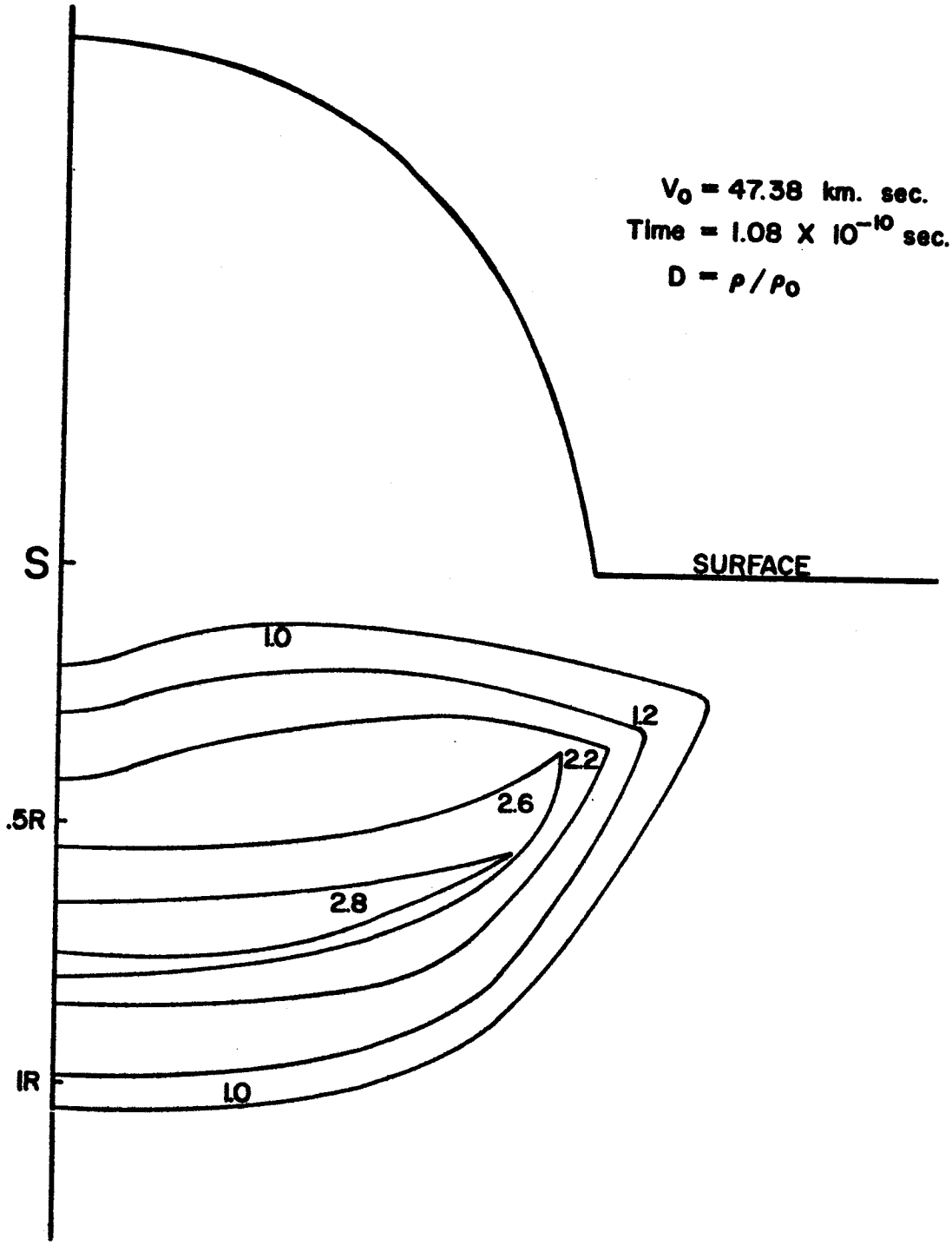

Figure 55. Constant Density Contours, Case V (Time = 1.08×10^{-10} seconds)

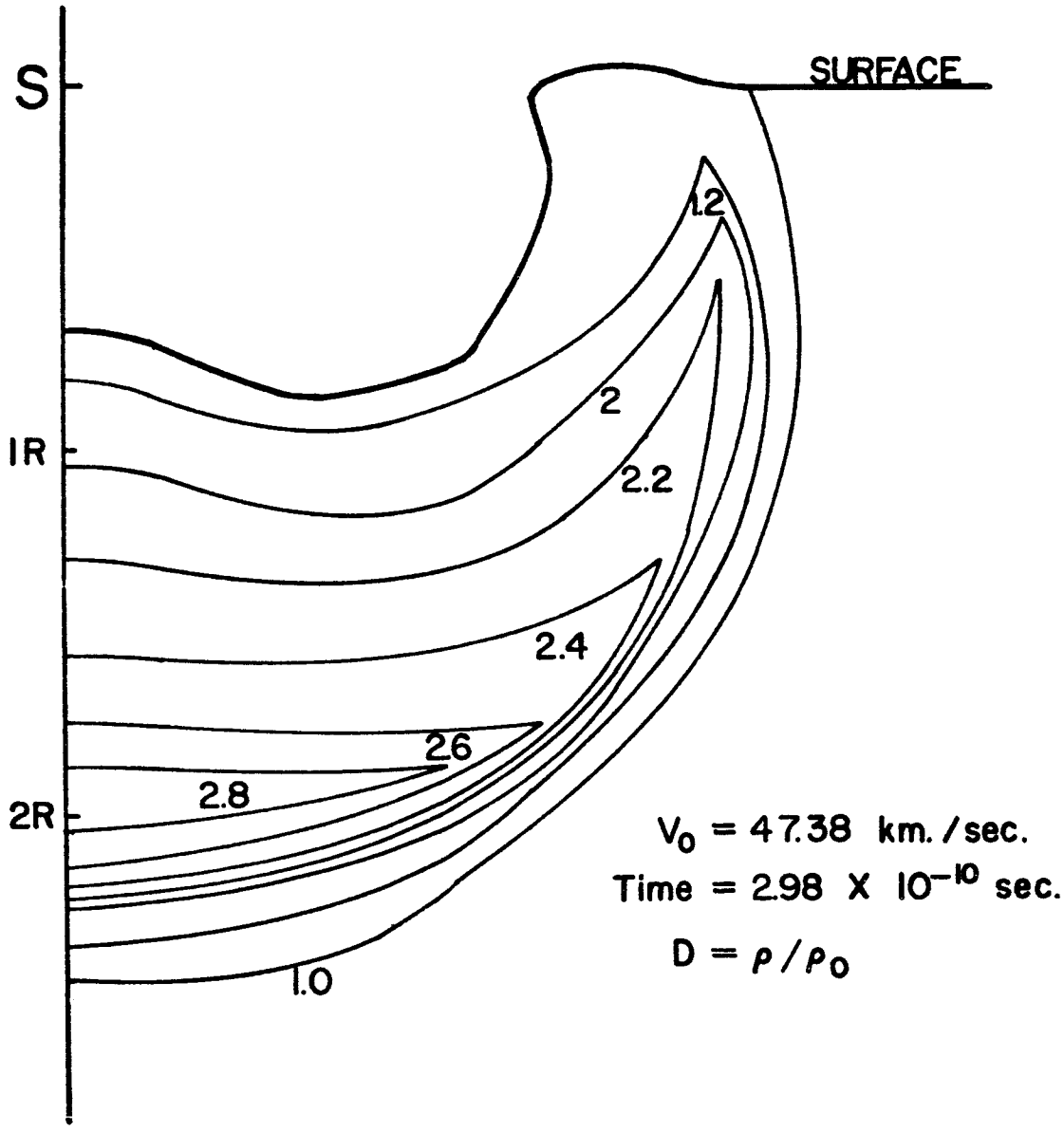

Figure 56. Constant Density Contours, Case V (Time = 2.98×10^{-10} seconds)

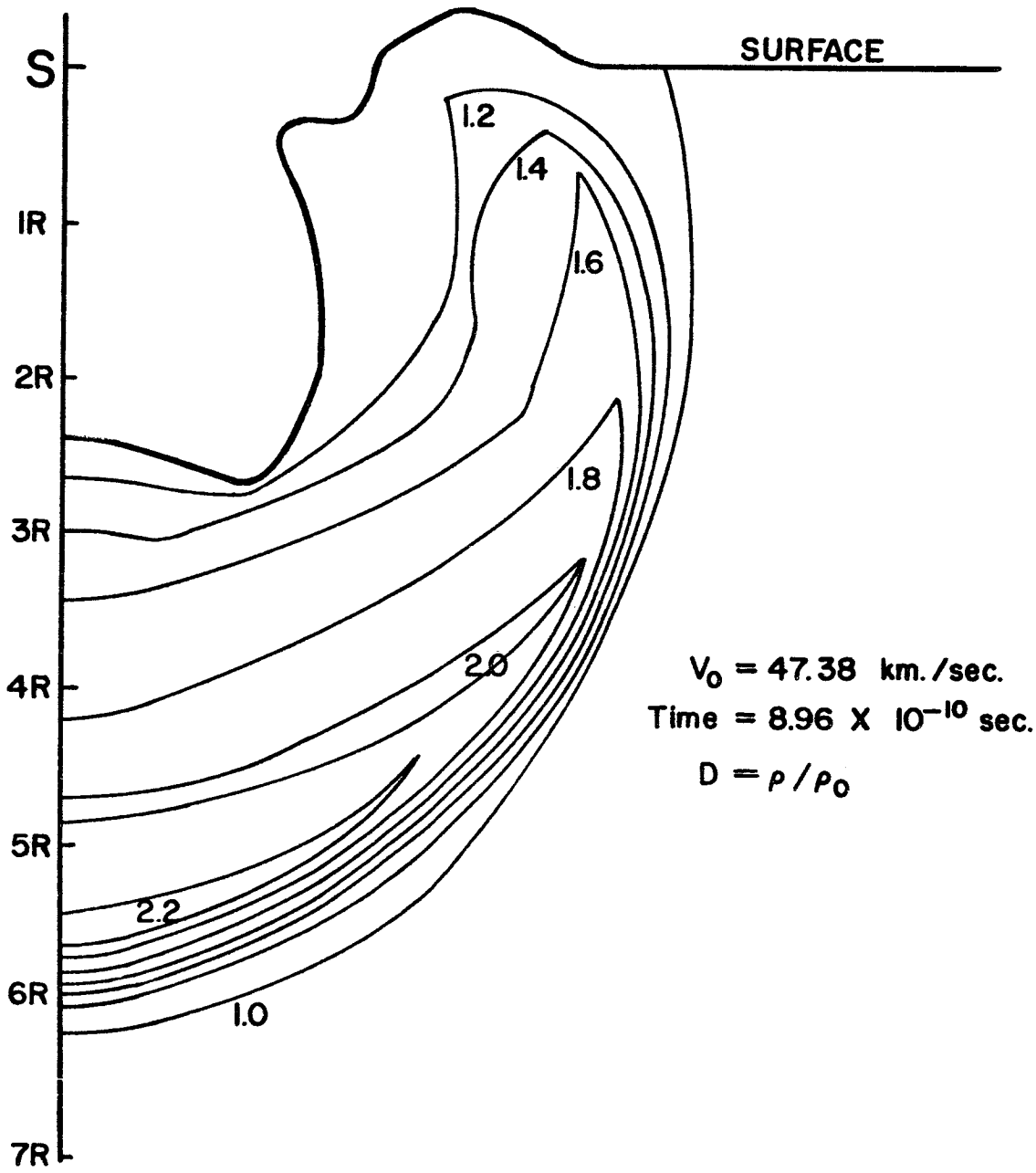

Figure 57. Constant Density Contours, Case V (Time = 8.96×10^{-10} seconds)

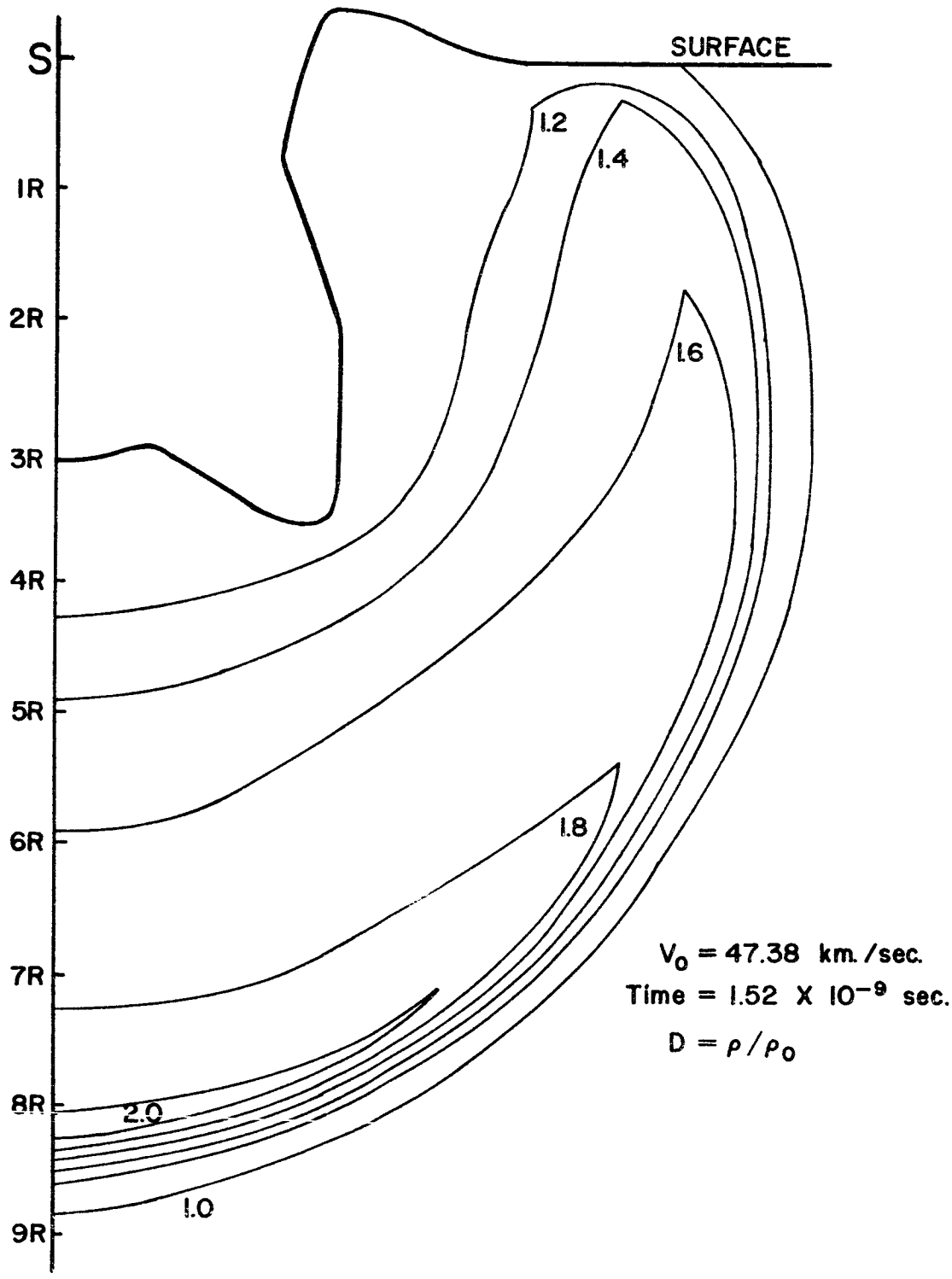

Figure 58. Constant Density Contours, Case V (Time = 1.52 x 10^{-9} seconds)

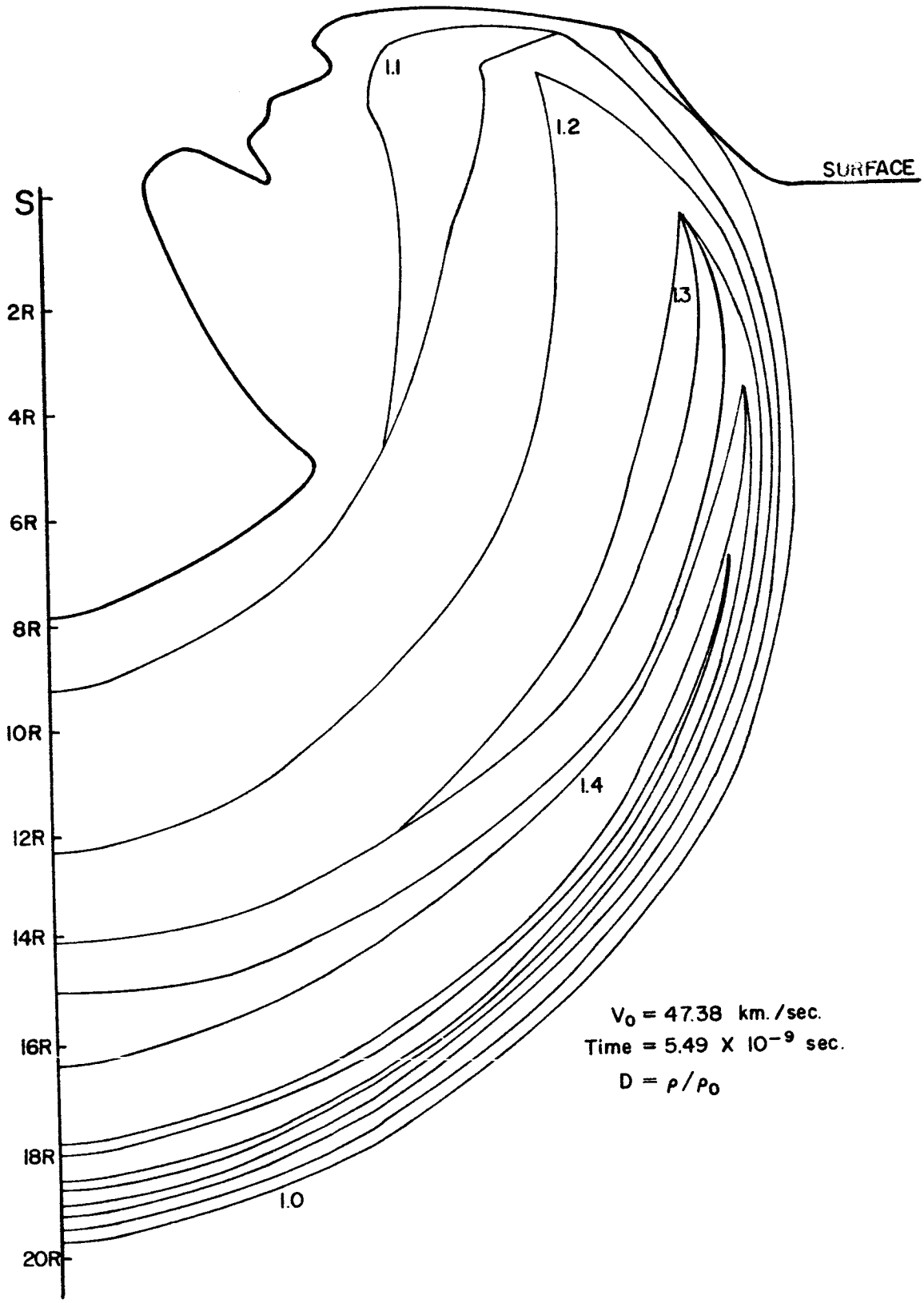

Figure 59. Constant Density Contours, Case V (Time = 5.49×10^{-9} seconds)

variation are found in Figures 55 and 56.

Material is first seen above the target sruface in Figure 57. It is at this time that the condition requiring the density ratio to be equal to or greater than one is first invoked. Material which leaves the target is probably in the form of a fine spray. The average density of this spray, composed of some material clusters and some vacuum between, is undoubtedly less than that of normal aluminum. In failing to adequately describe such states, which would have a negative pressure, the equation of state blocks the motion of the shock wave in the direction prependicular to the axis of impact.

The penetration process continues as the peak density decays. Further results of the numerical solutions are given in Figures 58 and 59. The disturbance, in Figure 59, has advanced along the target surface to a point seventy-five per cent of its penetration along the normal axis. While some of this reduction in lateral expansion follows from the finite size and shape of the individual micrometeoroid, that is, because of its explosive entrance into the target; the expected flow patterns are not fully developed. A retarding mass has appeared in the solution where material composed of aluminum which should have been ejected with a high velocity and low density is found.

Dissipation of the Peak Pressure

A further set of curves emphasing pressure decay have been prepared for six cases. These are presented in Figures 60 through 65. This group is shown in order to illustrate the rapid decay of the peak pressure. These peak value dissipation traces also permit correlation with experimental data and other theoretical calculations.

The curves are drawn using the approximate peak pressure along the normal axis versus the position of this function on the normal axis. There is some uncertainty concerning the exact point to point comparison, but the average curves yield a satisfactory indication of the decay rate. Distance along the axis is measured in units of the micrometeoroid radius, R, from the point of impact, S. As R increases, there is some uncertainty in interpreting the peak pressure and the large scale of the drawings seems to indicate a decay to a constant state. This is not observed in the results as can be verified by reference to full pressure distributions.

For the case of an impact velocity of 36 km/sec., sufficient information was obtained from the numerical solution to indicate the growth to a peak pressure of 12 megabars and the subsequent decay. This value is found in other shock propagation calculations (4, 14). The decay curve for Case IV, V_o = 36 km/sec. is shown in Figure 60.

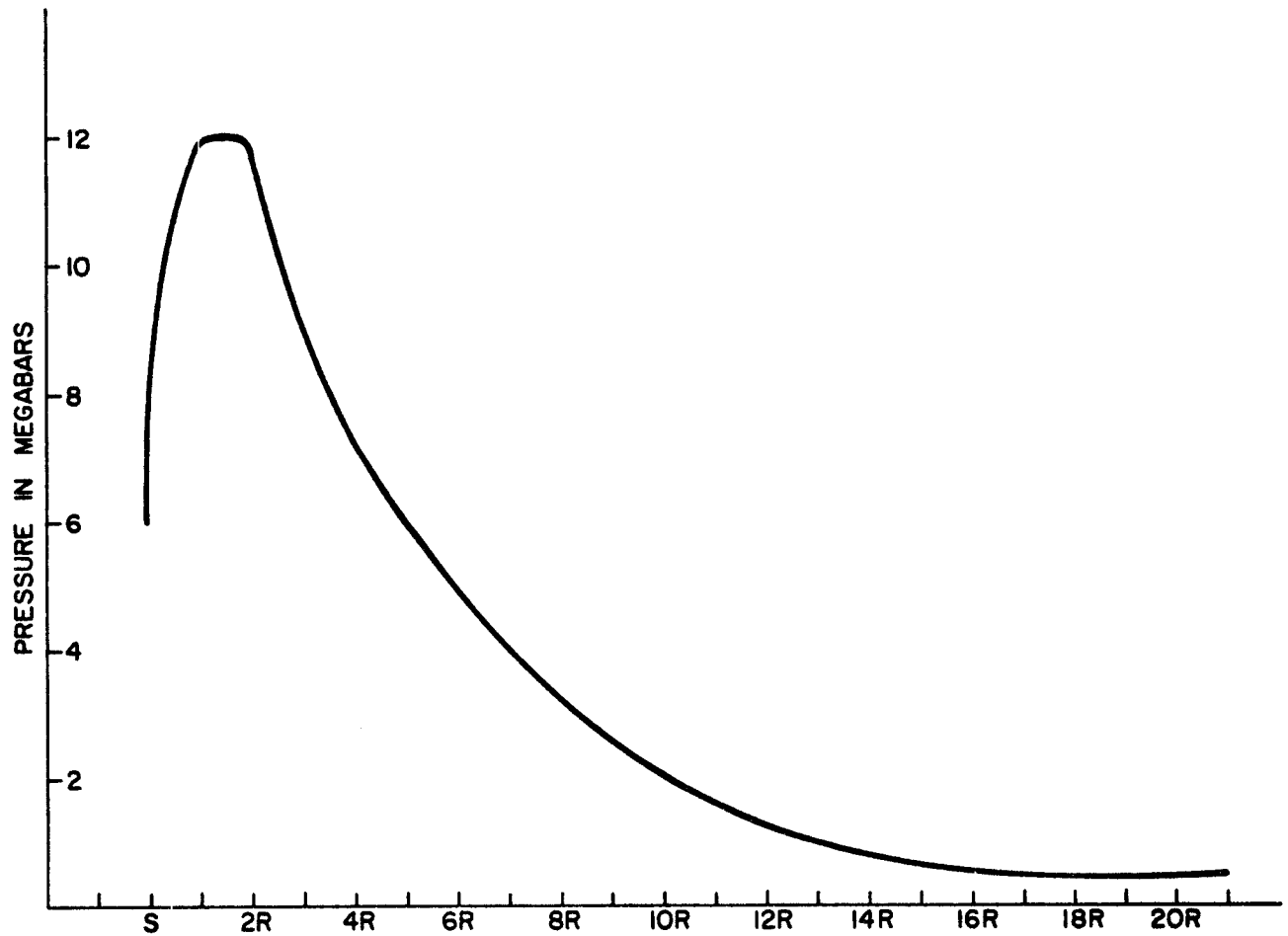

Figure 60. Approximate Peak Pressure vs. Maximum Penetration, Case IV

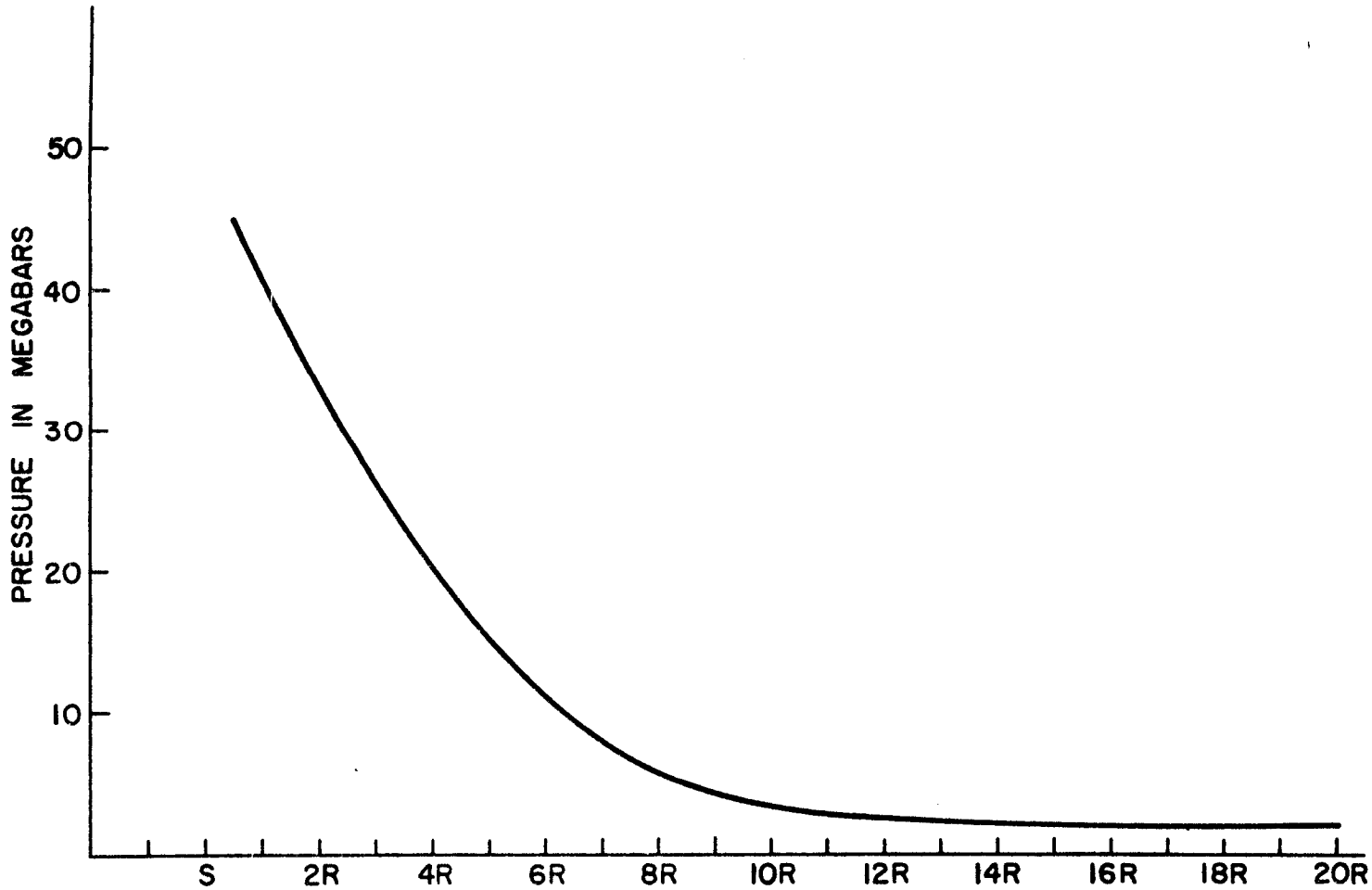

Figure 61. Approximate Peak Pressure vs. Maximum Penetration, Case VI

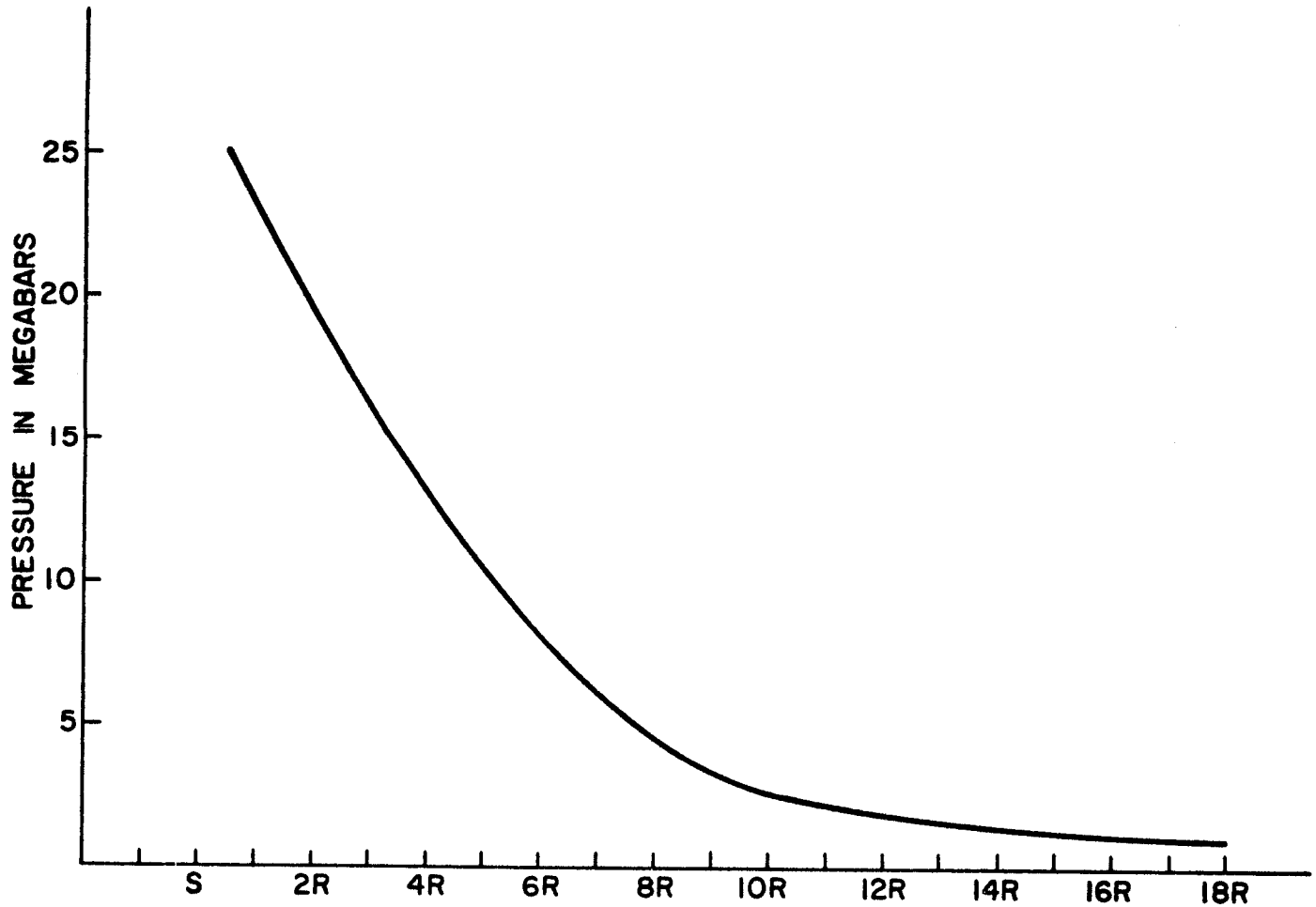

Figure 62. Approximate Peak Pressure vs. Maximum Penetration, Case V

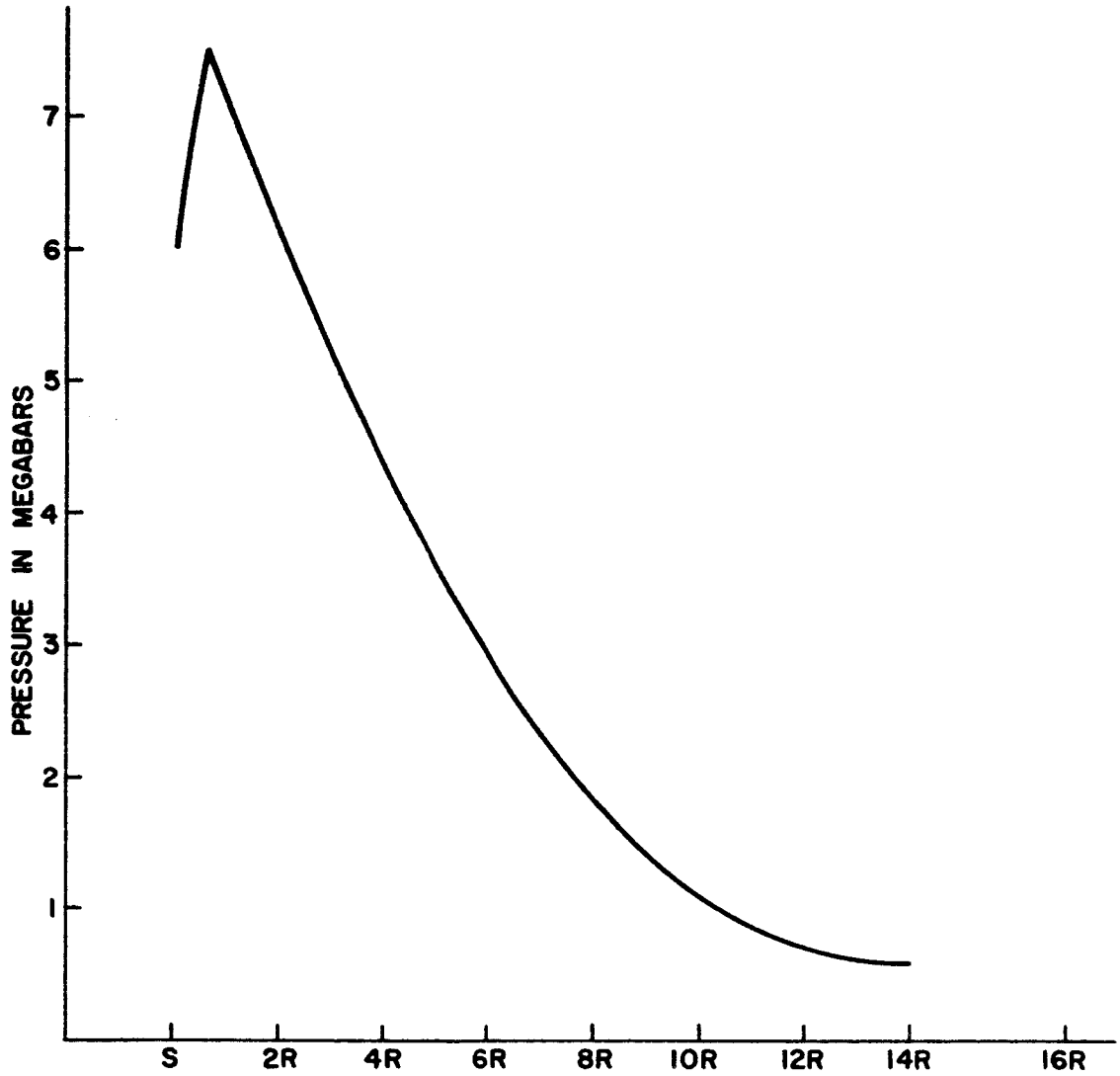

Figure 63. Approximate Peak Pressure vs. Maximum Penetration, Case III

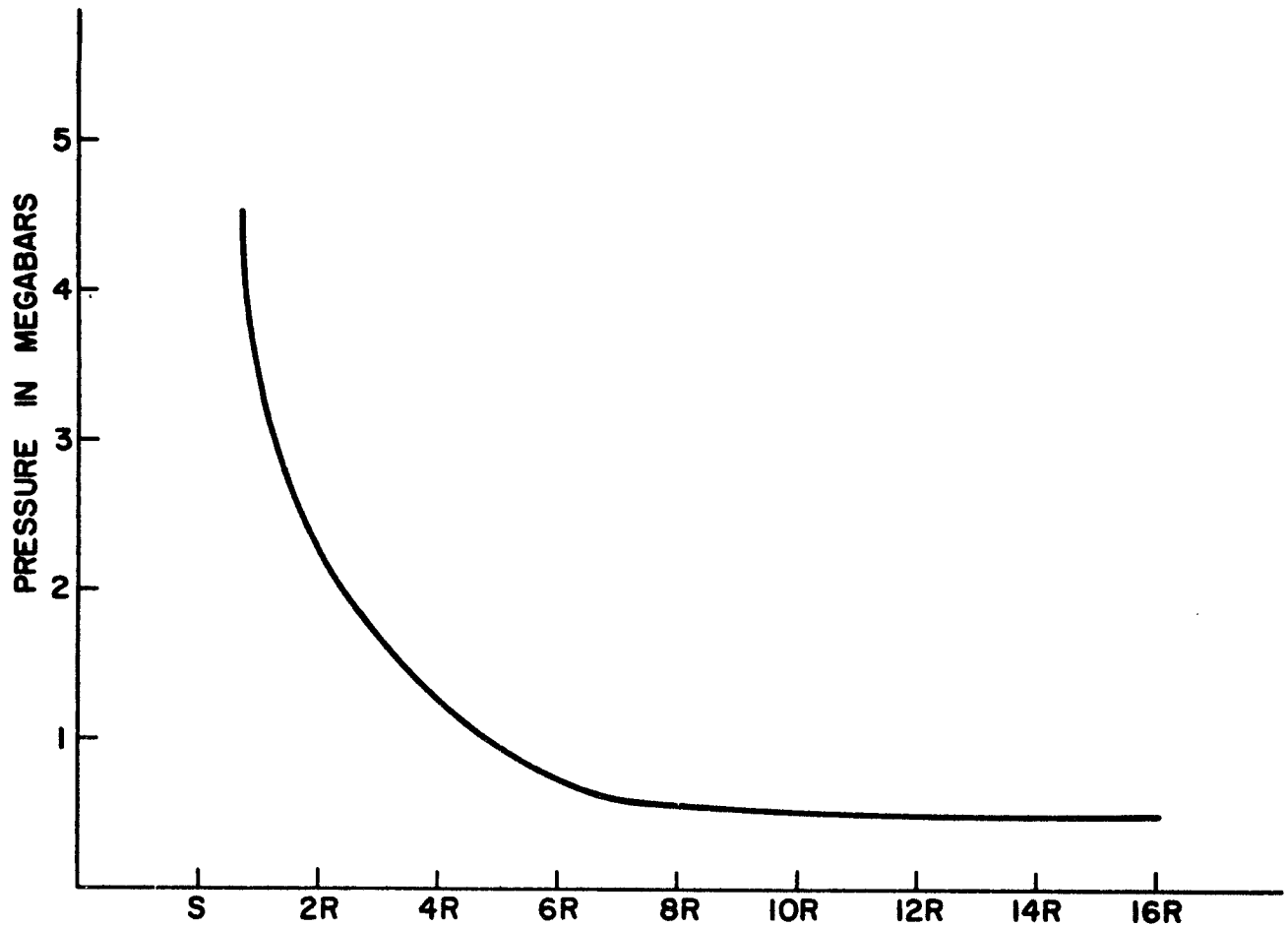

Figure 64. Approximate Peak Pressure vs. Maximum Penetration, Case II

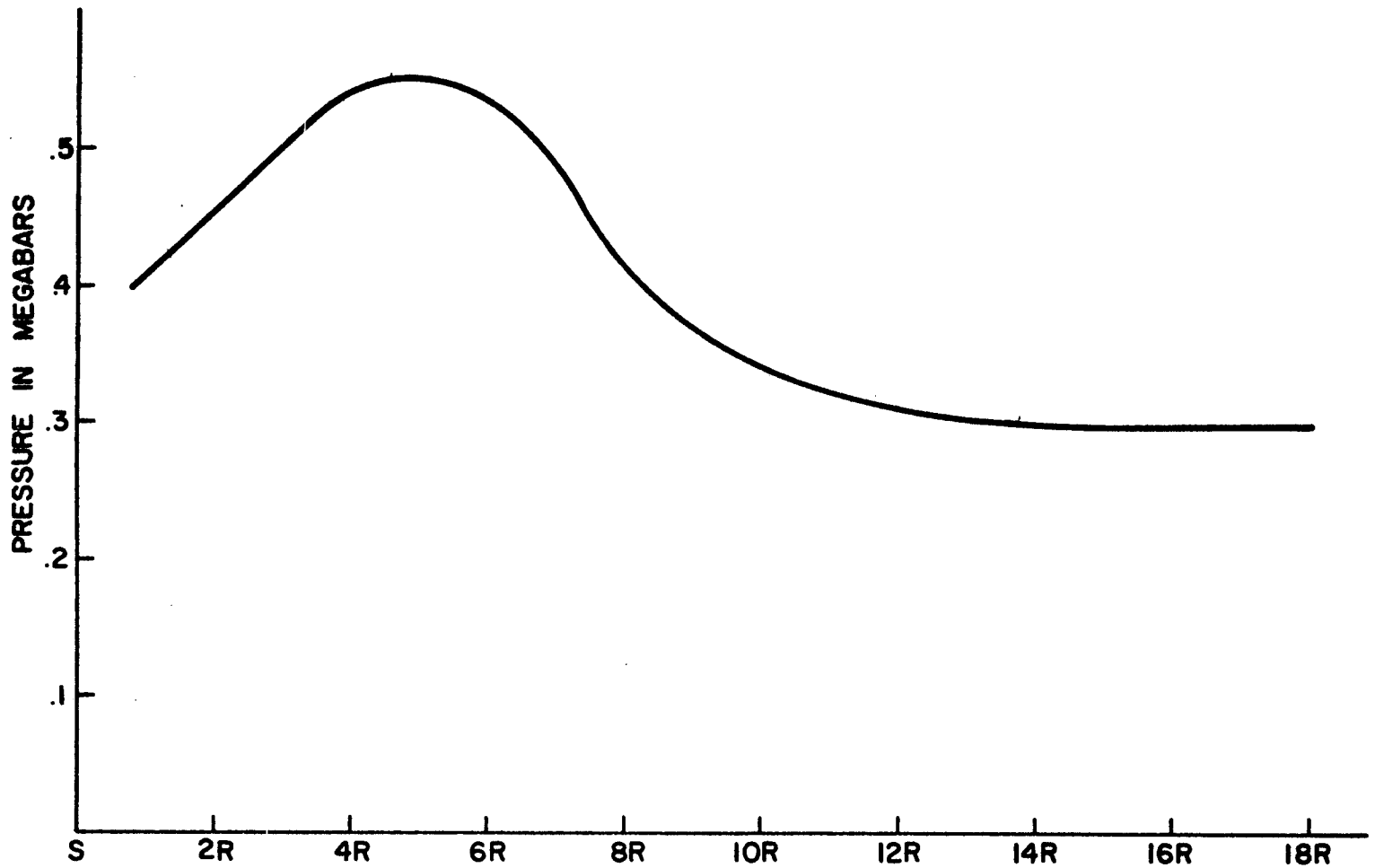

Figure 65. Approximate Peak Pressure vs. Maximum Penetration, Case I

Results for other cases are the same type. Dissipation of peak pressure for Case VI, $V_o = 60.64$ km/sec. is shown in Figure 61. Such curves give an indication of the transient nature of the peak pressures which occur in the impact process. These peak pressures, however, determine the subsequent states of the affected target material and ultimately the crater size and terminal mechanisms. Each decay curve is uniquely determined by the particular impact velocity.

Results are continued in Figures 63 and 64 for two more impact velocity case. Case I, in which $V_o = 5.68$ km/sec. is somewhat different from the other cases. There is a much more gradual rise and fall in the decay curve. The value predicted is about equal to a plate on an aluminum target. (23). The long persistance time of the peak pressure would explain why experiments have been so exact on reporting impact velocity versus peak pressure. Since the time changes with the size of the projectile, laboratory sample dimensions would make the peak pressure more susceptible to a constant value peak pressure measurement.

The correlation of peak pressure with other impact properties implies a relatively separate, initial shock. The characteristic variation of this quantity with impact velocity and an explanation for high and low velocity pressure dissipation curves are illustrated in Figure 66. This plot essentially relates the amount of energy transferred from microparticle to target when the particle is half

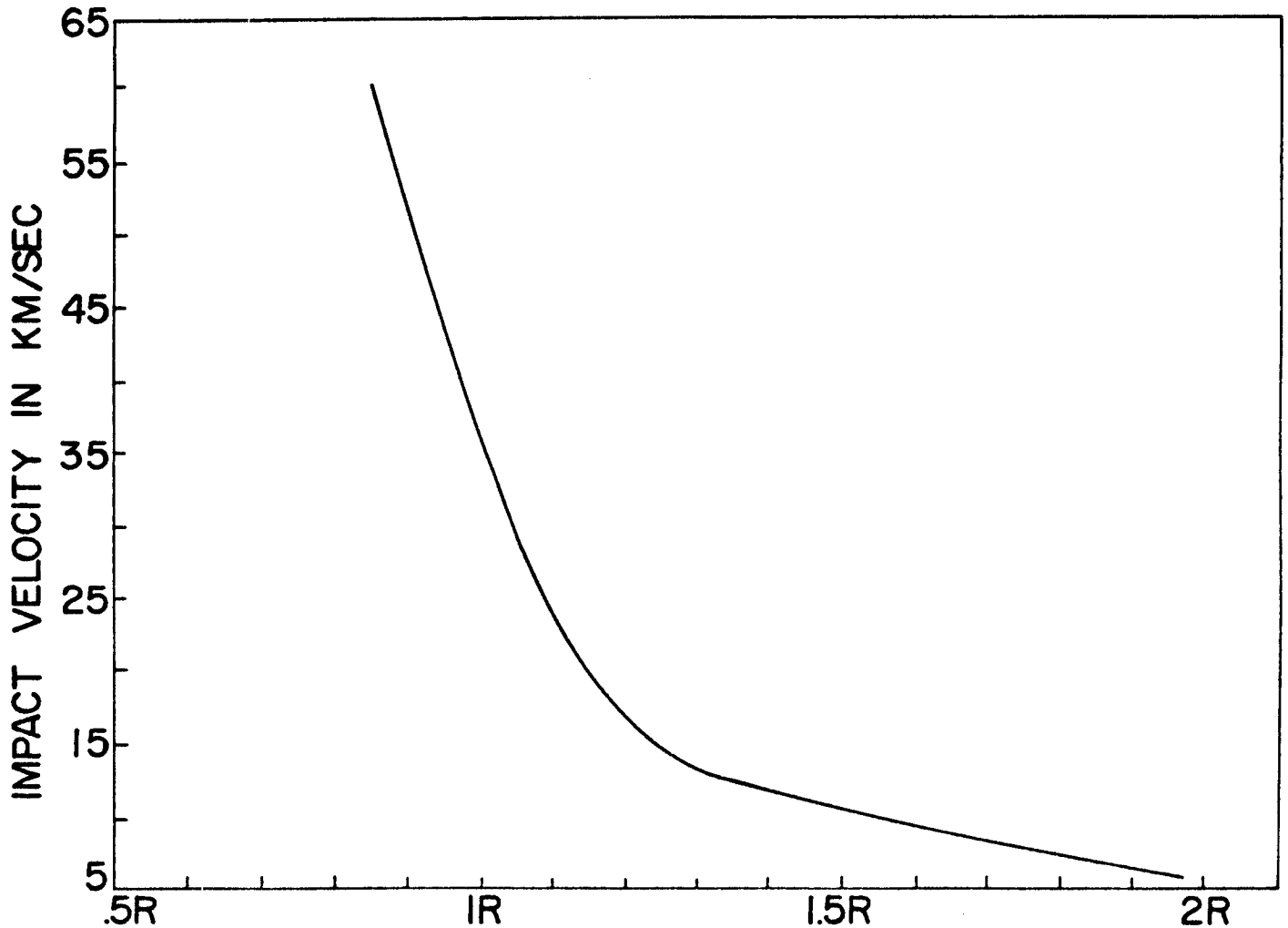

Figure 66. Position of Primary Shock Front on Normal Axis at a Time when the Micrometeoroid is One-Half Embedded in the Target as a Function of Initial Impact Velocity.

embedded in the target. The general trend agrees with results obtained from previous treatment which considered an impact by an incompressible micrometeoroid which penetrates only half-way into the target (4).

Discussion of Results

Six different cases were solved with an IBM 7094 computer. Each case involved a different impact velocity. This is necessary since the principles of similitude are not applicable. A number of features are common to the solutions. Difference have been found between high and low impact velocities.

The most interesting feature of this project is the production of two distinct shock waves at the point of initial contact. Both shock waves are of approximately equal strength traveling in opposite directions. There is some asymmetry in the forward direction, however; the primary shock front is somewhat stronger since it moves into undisturbed material. The progress of such waves is followed for all cases until free boundary reflection of one wave and considerable decay of the primary shock front modify the flow patterns. The start and growth of the cratering process have been fully depicted. A complete description must be found in other material regimes, such as the plastic and elastic.

Defects in the aluminum equation of state used have been pointed out in several places in this work. Originally,

the equation of state was developed in order to extend experimental data to ultra high pressure regions. Consideration of very low pressure and tension states need not be considered until later stages of the numerical calculations. The errors proceeding from this fault are localized near the target surface and probably do not invalidate the results obtained near the normal axis. Such results indicate the formation of a depression approximately circular with respect to the point of first contact.

CHAPTER V

SUMMARY AND SUGGESTIONS FOR FUTURE WORK

Calculations for the impact of a spherical aluminum microparticle on a semi-infinite aluminum target at six different velocities have been presented. A numerical method was developed and tested for the solution of a set of Eulerian, dimensionless, equations which were modified to describe large-scale fluid distortions. These distortions include shock wave propagation and target motion. A FORTRAN computer program has been used to obtain solutions for all cases up to a time when the decay of the primary shock front is significant and the resulting crater is well formed.

A basic feature of these solutions is the formation of two shock waves at the position of initial contact of microparticle and target. One shock front, the primary shock wave, travels into the target compressing material of the target. The other, moving into the projectile, is reflected at the material-vacuum boundary. The resulting rarefaction wave eventually overtakes the primary wave and weakens it. Another feature noted in all curves depicts the formation of a crater and the ejection of material above the original target surface. The impacting microparticle appears to compress the target material ahead of and surrounding itself. This results in

the flow of the target material up, around the entering particle and out of the target.

As the disturbance engulfs more target material, the hydrodynamic pressures become comparable to yield stresses. It is then inappropriate to neglect material strength and the hydrodynamic model becomes inapplicable. This same difficulty occurs earlier near the free surfaces involved in the problem. Consideration of necessary descriptive equations of the plastic and elastic states in addition to the hydrodynamic state will give a more complete description of micrometeoroid impact.

It is believed that inclusion of plasma properties in the equation of state, and addition of plasma conservation equations to the modified Eulerian set, would explain the radiation observed in the impact process.

These extensions, the refinement of the hydrodynamic model to include plasma, plastic, and elastic material should lead to a better understanding of the hypervelocity impact problem.

SELECTED BIBLIOGRAPHY

1. Collins, R. D., Jr., and W. Kinard. NASA TN D-230 (May, 1960).

2. Alexander, W. M., O. E. Berg, and M. Dubin. Direct Measurements of Cosmic Dust Showers. NASA TN D-1544 (January, 1963).

3. Cook, M. A. "Mechanism of Cratering in Ultra-High Velocity Impact," J. Appl. Phys. 30 (1959) 725-735.

4. Lake, H. R. "Digital Computer Solution for Propagation of a Spherical Shock Wave in Aluminum," Master's Thesis, Oklahoma State University (1962).

5. Bjork, R. L. "Effects of a Meteoroid Impact on Steel and Aluminum in Space." Engineering Division, RAND Corporation, P-1662 (1958).

6. Todd, F. C. and H. R. Lake. "Analytical and Limited Experimental Study of the Mechanisms of Impact, Penetration and Light Emission for Micrometeorites on an Aluminum-Coated Photomultiplier." Quarterly Progress Report, No. 1. NASr-7, Research Foundation, Oklahoma State University, December 31, 1960.

7. Hamann, S. D. Physico-Chemical Effects of Pressure. New York: Academic Press (1957), 57-60.

8. Charters, A. C. "High Velocity Impact," Scientific American 203 (October, 1960), 128-140.

9. Richtmyer, R. D. Difference Methods of Initial-Value Problems. New York: Interscience Publishers (1957), 207.

10. Von Neumann, J. and R. D. Richtmyer. "A Method for the Numerical Calculations of Hydrodynamic Shocks," J. Appl. Phys. 21 (1950), 232-237.

11. Landshoff, R. A Numerical Method for Treating Fluid Flow in the Presence of Shocks. Los Alamos Report LAMS-2379 (April, 1959).

12. Walsh, J. M., N. H. Rice and R. G. McQueen. "Compression of Solids by Strong Shock Waves," in Solid State Physics, 6, 1-63. New York: Academic Press (1958).

13. March, N. H. "The Thomas-Fermi Approximation in Quantum Mechanics," Adv. in Phys. 6 (1957), 1-101.

14. Sodek, B. A., Jr. "The Penetration of an Aluminum-Glass Interface by an Originally Radial Shock Wave," Master's Thesis, Oklahoma State University (1965).

15. l. c. 9, p. 199.

16. Longley, H. J. Methods of Differencing in Eulerian Hydrodynamics. Los Alamos Report LAMS-2379 (April, 1959).

17. Ables, J. G. Private Communication.

18. l. c. 9, p. 38.

19. l. c. 9, p. 40.

20. l. c. 9, p. 77.

21. l. c. 9, p. 169.

22. l. c. 9, p. 197.

23. Sodek, B. A. and F. C. Todd. "Penetration of an Initially Radial Shock Wave Through an Aluminum-Glass Interface," Proc. Okla. Acad. Sci. 43 (1963) 173-182.